DUCTILE FRACTURE BY VOID NUCLEATION, GROWTH AND COALESCENCE

by

Ronald D Thomson,

James Watt Engineering Laboratories,

Department of Mechanical Engineering,

University of Glasgow,

Scotland.

Submitted to

The University of Glasgow

for the degree of

Doctor of Philosophy

April 1985.

ABSTRACT

Plastic deformation in ductile metals is limited by a mechanism in which voids, nucleated at second phase particles, grow and coalesce to form a crack. The results of a finite element solution for spherical elastic inclusions in a plastically deforming matrix are discussed. These results have been used in conjunction with experimental work using notched tensile specimens to generate multiaxial states of stress from which the local conditions leading to decohesion of the inclusion/matrix interface were determined. An important feature of these results is the statistical distribution of the interfacial strength. This distribution is bimodal, showing the presence of both weakly and strongly bonded particles. The latter have a modal strength of about 7 times the initial yield stress and the weakly bonded particles are assumed to be pre-existent. Experiments in plane and axisymmetric states of strain indicate that while the stress state is of relevance, the remote strain state is not. The absence of a macroscopic strain state effect is explained in terms of the statistical distribution of the voids nucleated from the population of randomly distributed inclusions. The stress and strain concentrations possible in local patches of high porosity have been investigated by a finite element approach based on the mechanics of a dilating continuum to determine void growth in the porous aggregate and the local conditions at failure. This investigation recognises the importance of the local hardening rate of the aggregate material and leads naturally to the idea of a size scale for failure, in the light of which the concept of a crack-like defect is re-examined.

PREFACE

The work described in the following thesis was performed at the University of Glasgow over the period from October 1979 to April 1984. This work divides naturally into five major sections. Part 1 contains an introduction, provides a background to the work and gives reference to the existing literature. Successive parts deal with different aspects of the overall problem. An attempt was made to keep the size of the thesis to a minimum. In this spirit, while the numerical analysis performed was considerable, only outlines of the procedures are given in the appendices and results are presented as far as possible in graphical form. Further information on the coding and results can be obtained from the author.

ACKNOWLEDGEMENTS

My greatest debt is to Dr J W Hancock, who suffered this fool gladly, showing patience and understanding over and above the call of duty. Acknowledgement is also due to Dr D K Brown and Dr M J Cowling of the Department of Mechanical Engineering at Glasgow for their technical advice and moral encouragement during the project.

Appreciation is expressed to Prof R M McMeeking of the University of Illinois and Prof D M Parks of the Massachusetts Institute of Technology for much helpful discussion and for kind permission to use their finite element procedures.

The work was partially funded by the SERC Marine Technology Programme at the Glasgow University Centre. Thanks are due to the Programme Coordinator, Dr M J Cowling, and to Prof B F Scott, James Watt Professor of Mechanical Engineering at Glasgow, for the facilities provided.

Thanks are also due to Mr A Torry who assisted with the experiments, to Ms A MacKinnon for her assistance on the SERC computing network and to Mr D Fildes of Glasgow University Computing Service who met, without complaint, my frequent demands for additional and more sophisticated facilities on the University mainframe.

Finally, I owe a debt of gratitude to my wife Morag, who has tolerated over a number of years my antic disposition and a work schedule which would give adequate grounds for divorce.

PART 3: VOID NUCLEATION IN DUCTILE MATERIALS.

PART 4: THE INITIATION OF FAILURE.

PART 5: THE STRESS AND STRAIN FIELDS NEAR CONTAINED INHOMOGENEITIES IN A DEFORMING MATRIX.

APPENDICES.

SYMBOLS

For symbols with multiple meanings, the actual meaning will be clear from the context. Basic symbols may be modified by the addition of subscripts and superscripts.

BASIC SYMBOLS

A	Goodier constant
a	semi-major axis of elliptical void, lattice parameter, crack half-length
B	Goodier constant
b	semi-minor axis of elliptical void, Burger's vector
C	constitutive tensor, Goodier constant, interfacial radial stress concentration factor, strain state function, constant
D	rate of deformation, void volume parameter
d	mean dislocation spacing, diameter of tensile specimen
E	strain of aggregate material, void shape parameter
e	strain of matrix material
f	porosity (void volume fraction) of porous material
G	shear modulus
g	pressure dependent yield term
J	Jacobian of deformation
K	bulk modulus, stiffness matrix, stress intensity factor
k	yield stress in shear
M	eccentricity of elliptical void
n	power hardening index, unit normal
P	probability

q	Tvergaard constant
R	average radius of elliptical void
S	closure of deforming body, aggregate deviatoric stress
s	matrix deviatoric stress
T	surface traction
t	time
u	displacement
V	aggregate volume
v	strain state parameter, matrix volume, velocity
W	power dissipation in aggregate material
w	power dissipation in matrix
y	uniaxial loading axis
Z	Cauchy stress in aggregate material
α	direction of maximum shear, forest hardening factor
β	second shear direction
γ	free surface energy
δ	Kronecker delta, first variation, small distance
ϵ	matrix deviatoric strain
$\emptyset$	yield function, volumetric degree of freedom
Λ	Lagrange multiplier in aggregate flow rule
λ	Lagrange multiplier in non-porous or matrix flow rule
μ	Poisson's ratio, viscosity
ρ	dislocation density
σ	Cauchy stress in matrix material
τ	shear stress, Kirchhoff stress
Ω	angular displacement from loading direction

SUBSCRIPTS

0	initial value, initial yield value
∞	remote value
C	critical value
c	critical value
ij	general tensor component
m	mean
max	maximum value
r	radial component
rr	radial component
y	current yield value
yy	component in uniaxial loading direction
α	maximum shear component
β	second shear component

SUPERSCRIPTS

-(overbar)	effective, equivalent or representative value
'	modified value (defined locally in text)
.	time rate
^{0}	Jaumann rate
el	elastic component
p	plastic component

The summation convention is used throughout unless otherwise stated, but is restricted to the Roman letters i - n inclusive (these are the FORTRAN implicit integers). This allows normal engineering notation in an x,y,z coordinate system to be used where appropriate.

FOOTNOTES.

Page 3.4 The elastic constitutive equation:

$$\sigma_{ij} = C_{ijkl} e^{el}_{kl}$$

must be regarded here as empirical, since it is not derived from a potential function. The material is then hypoelastic.

Page 3.12. In the relation:

$$Z_m/\bar{Z} = \sigma_m/\bar{\sigma}$$

the quotient $\sigma_m/\bar{\sigma}$ is not the triaxiality at a point in the matrix of a dilating material, but is rather the initial triaxiality for a material in which f_0 is small. This result implies that the triaxiality of a dilating porous aggregate may be determined on the basis of an incompressible solution.

Page 5.19 Although nucleation is based here on an interfacial strength criterion, the contribution of the effective stress to the radial stress is fundamentally a strain-driven parameter.

Page 13.1 The void volume fractions at failure are calculated from the void growth equations and the known inclusion content of the material. Such values could then be verified experimentally, although this was not the case for the specimens noted here.

Page 17.5 It is not clear whether the 'instability' encountered with hydrostatic loading is a numerical problem or a feature of the real material. The latter seems unlikely.

PART 1: INTRODUCTION.

1. FAILURE IN METALLIC MATERIALS.

1.1. FRACTURE MECHANISMS.

Traditionally the demands of mechanical engineers have been for materials of increasing tensile strength and while the strength of pure metals is usually inadequate for engineering purposes, this can be improved by altering the microstructure through heat treatment, plastic working or by the addition of alloying elements which promote the formation of second phase particles. However, materials can fail at surprisingly low loads and an understanding of the mechanisms responsible for such failures is essential. In the wide class of failures known as fracture, cracks are propagated within the material, a process which requires an energy input. This energy requirement provides a basis for the classification of fracture.

Brittle fracture is characterised by small amounts of plastic deformation ahead of the crack tip and crack advance thus consumes very little energy in the form of plastic work and may proceed under the driving action of the strain energy released from elastic material which relaxes during crack extension. Such a situation can lead to unstable crack growth and result in catastrophic failure of the material. In the extreme case of cleavage fracture, with virtually no plastic deformation ahead of the crack tip, the crack advances along crystallographic planes or grain boundaries, giving a faceted topography to the fracture surface which thus has a characteristic shiny appearance.

In contrast to brittle modes, ductile failure is characterised by large amounts of plastic deformation ahead of the crack tip. The stretching of the intervoid ligaments in the material produces a dull fracture surface with a fibrous appearance which gives rise to the term 'fibrous rupture'. The large amount of plastic work required to advance cracks in ductile materials implies that they are generally tougher than brittle materials and better able to tolerate the small defects which inevitably exist within a material. However the failure mode of a material depends not only on the microstructure but on environmental factors including the local stress and strain fields. The design of improved structural alloys thus requires an understanding of the mechanics of both brittle and ductile fracture in a variety of environmental conditions.

1.2. BRITTLE FRACTURE.

Theories of brittle failure, largely based on the energy approach pioneered by Griffiths (1921), have been notably successful and the mechanics of brittle failure are now well understood. In many practical situations such mechanics may be described by the terms of linear elastic fracture mechanics (LEFM). In LEFM, the stress field around the crack is characterised, not by the stress at the crack tip, which will be infinite for an infinitely sharp crack irrespective of the local environment, but by the stress intensity factor K, given by:

$$K = f(G)\ \sigma_\infty \sqrt{\pi a}$$

in which f(G) is a geometry parameter, σ_∞ is the remote stress and a is the crack half-length. Essentially, K describes the rate at

which the stress approaches infinity towards the crack tip and thus characterises the order of the crack tip stress singularity, providing a means of comparing the crack tip stress fields in materials under different loading conditions. In particular, LEFM allows the determination of the fracture toughness K_c, a material parameter defined as the critical value of K necessary to advance a crack.

1.3. DUCTILE FRACTURE.

In real materials, the formation of a stress singularity is pre-empted by the occurrence of local yielding but provided the plastic zone ahead of the crack tip is small, the local stress field will be dominated by elastic terms. For such 'small scale yielding' the stress field may still be adequately characterised by K. If the plastic zone is larger, nonlinear plastic work terms become significant and LEFM must give way to elastic/plastic fracture mechanics (EPFM). In EPFM, the plastic work terms are included in a macroscopic approach to the energetics of crack advance and appear in energy integrals such as Rice's (1968) J-integral, although this is rigorously applicable only to non-linear elastic fields, or indirectly in parameters such as the crack opening displacement (COD). As the size of the plastic zone increases, the mechanism of fracture tends towards ductile tearing, the subject of the current work, for which an adequate theory does not yet exist.

1.4. DUCTILE FAILURE BY VOID COALESCENCE.

The extent of plastic deformation in ductile materials is often limited by a mechanism first identified by Tipper (1949), in which voids nucleated at hard particles in the metal matrix (fig.1.1) grow with increasing plastic strain until widespread coalescence occurs soon after plastic flow becomes concentrated close to the final fracture surface (fig.1.2).

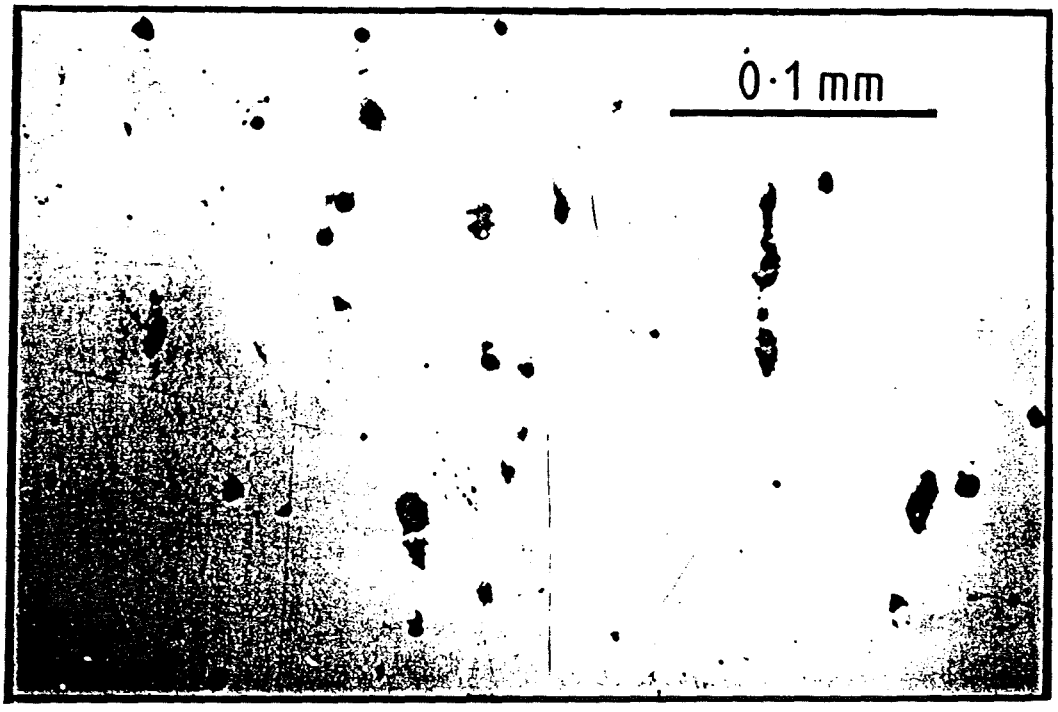

Fig.1.1. The nucleation of voids from hard particles in a metal matrix. Note the voids due to cracked particles and decohesion of the interface, and the random distribution of inclusions.

Such a mechanism is of relevance in many engineering contexts: in the triaxial stress field which exists ahead of a blunting crack, during the service loading of engineering components in which plastic flow

fields may occur in the vicinity of complex geometries and during the large deformations typical of metal forming operations. In general, such failures occur in regions which involve multiaxial stress and strain gradients and the problem cannot be adequately described in purely macroscopic terms but requires an understanding of the micro-mechanics of failure. Furthermore, the intractability of the general problem requires the development of such an understanding in simpler situations where the local conditions of stress and strain may be obtained by analytic or numerical methods.

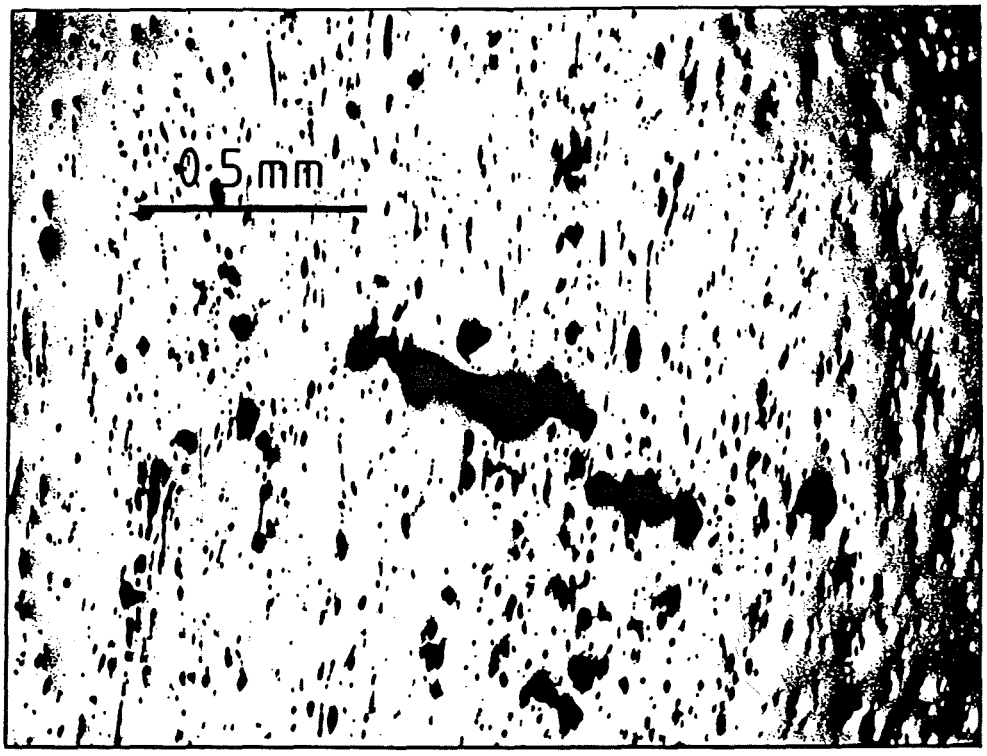

Fig.1.2. The concentration of deformation close to the final fracture surface. The final fracture surface is produced by the propagation of the obvious internal crack.

1.5. THE MECHANICS OF DEFORMATION.

The mechanics of deformation in the vicinity of second phase particles is intimately related to the size of the particles themselves. For particles whose size is comparable with the dislocation or slip-band spacing, the local conditions are most appropriately described in terms of dislocation mechanics, which considers plastic deformation to be driven by a shear stress τ given approximately by:

$$\tau = Gb\sqrt{\rho} \qquad \text{(equ.1.1)}$$

where G is the shear modulus, b is the Burger's vector and ρ is the dislocation density, defined as the total length of dislocation per unit volume of material or equivalently as the number of dislocations intersecting a cross-section of unit area. The average dislocation spacing d is then:

$$d = 1/\sqrt{\rho}$$

and substituting for ρ from equ.1.1 gives:

$$d = Gb/\tau$$

Replacing the shear stress τ by the effective stress $\bar{\sigma}$, defined in section 3.1, through the relation:

$$\bar{\sigma} = \tau\sqrt{3}$$

then:

$$d = Gb\sqrt{3}/\bar{\sigma} \qquad \text{(equ.1.2).}$$

For iron, b is of the order of 3×10^{-10} m while G = 80 GPa. Hence for stresses of the order of an initial yield stress of, say 0.2 GPa, dislocation mechanics is most appropriate over distances of the order of 0.2 μm.

On a larger scale dislocation mechanics becomes less suitable and McClintock (1968) has suggested that the stresses and strains near inclusions large enough to be seen with an optical microscope are adequately described within the framework of continuum mechanics. This qualitative criterion may be quantified if it is assumed that parameters retained in a continuum approach, such as the size and spacing of inclusions, are much greater than the mean dislocation spacing. Thus continuum mechanics may be taken to apply over distances very much greater than d in equ.1.2. To put such a size scale into the context of the microstructure of a real material, it is appropriate to compare it with the parameters of Swedish Iron, which features in much of the later experimental work. For this material, the inclusions have diameters of the order of 5 μm and a spacing of 20 μm (fig.1.3). The grain size is of the order of 500 μm. Equation 1.2 then implies that it is appropriate to describe the deformation near such inclusions in continuum terms.

Of course, this calculation is performed on the basis of the average material while in the vicinity of an inclusion it is necessary to consider distances smaller than the inclusion diameter itself. However in such regions the dislocation density is much greater than in the remote field and the scale of the applicability of continuum mechanics is likely to be reduced correspondingly. Nevertheless, even

within a framework of continuum mechanics, it must be recognised that events such as nucleation and failure initiation will be strongly dependent on the local microstructure.

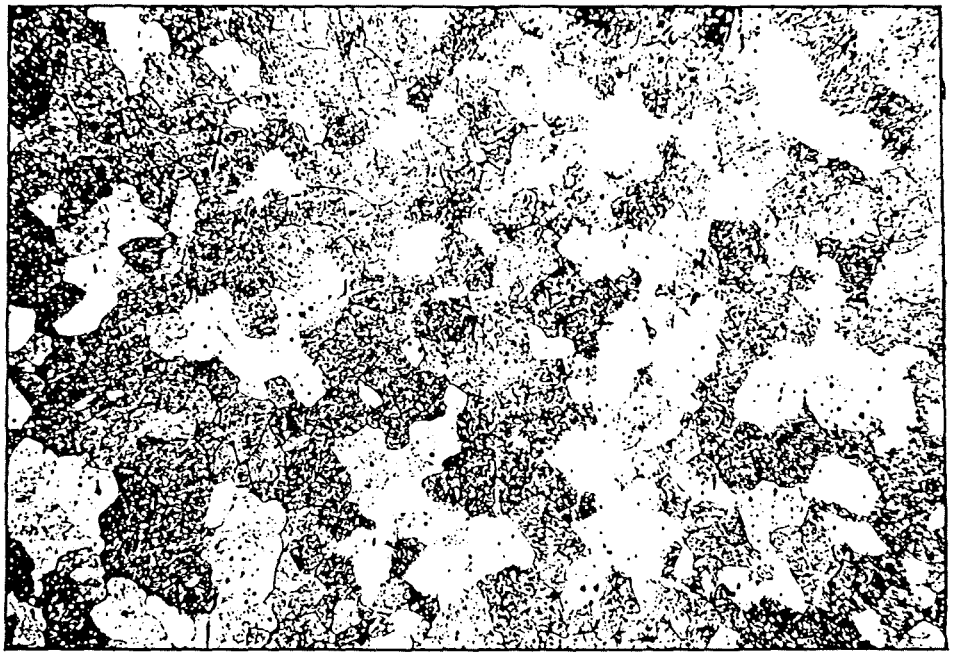

Fig.1.3. A metallographic section of Swedish Iron, etched with 5% Nital.

2. CURRENT APPROACHES TO DUCTILE FAILURE.

2.1. INCLUSIONS IN A DEFORMING MATRIX.

At a micro-scale, fracture often starts in the vicinity of inclusions in a deforming matrix where the local stress and strain conditions may lead to decohesion of the inclusion/matrix interface or failure of the particle itself. While the physical mechanisms of failure have been qualitatively described by Tipper (1949) and Puttick (1959) in terms of the nucleation and growth of the resulting voids, the quantitative description of these processes has awaited the development of the appropriate mechanics. In general, the nucleation and growth of the voids will depend on the local stresses and strains near the inclusions but since loads are in practice applied remote from the voids then such local conditions must be expressed in terms of force and displacement boundary conditions. The resulting description will depend on the way in which the material response is idealised in order to allow constitutive equations to be formulated and on the chosen mathematical techniques. Analytic solutions are available for elastic inclusions in an elastically deforming matrix but for plastic deformation it is necessary to resort to numerical methods.

2.1.1. ELASTIC SOLUTIONS.

The general solution for the elastic stress and strain fields near ellipsoidal elastic inclusions has been given by Eshelby (1957) who found that the fields within the inclusion are homogeneous. Solutions for spherical and cylindrical solutions can be derived as special cases of Eshelby's (1957) analysis but here it is more convenient

to refer to earlier work by Goodier (1933). In this, the solution for uniaxial tension is expressed in terms of arbitrary constants which are adjusted such that the appropriate boundary conditions are met on a closed path identified with the inclusion interface. The general solution for the elastic stress and displacement fields is expressed in plane polar coordinates (fig.2.1) as:

$$\sigma_{rr} = 2G(-(A/r^2)+(3(B/r^4)-2(C/r^2))\cos 2\omega) \qquad \text{(equs.2.1)}$$

$$\sigma_{\omega\omega} = 2G((A/r^2)-3(B/r^4)\cos 2\omega)$$

$$\sigma_{r\omega} = 2G(3(B/r^4)-(C/r^2))\sin 2\omega$$

$$u_{rr} = (A/r)+(-(B/r^3)+2(C/r)(1-\mu))\cos 2\omega$$

$$u_{\omega\omega} = -((B/r^3)+(C/r)(1-2\mu))\sin 2\omega$$

where A, B and C are arbitrary constants and μ is Poisson's ratio.

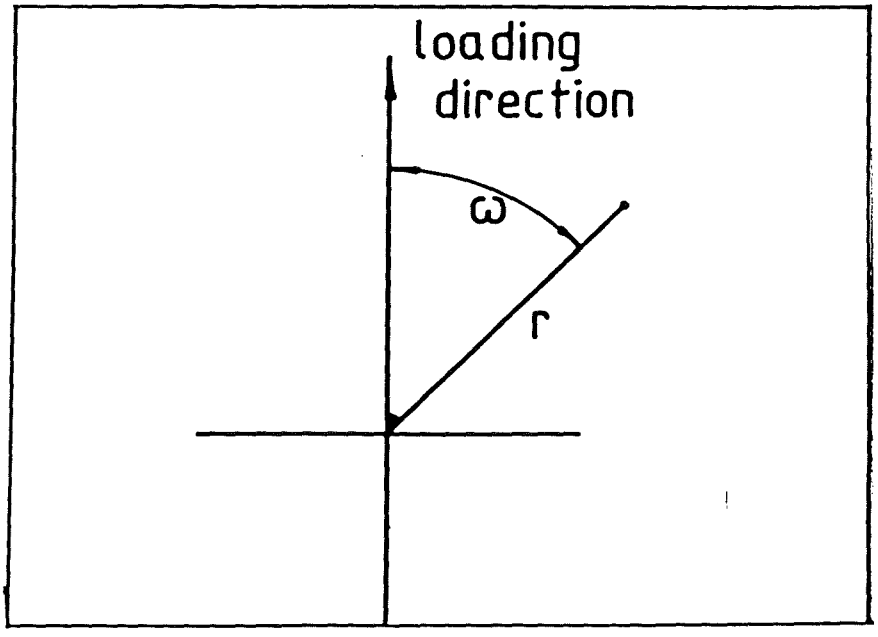

Fig.2.1. The polar coordinate system.

The homogeneous elastic stress and displacement components in a region subject to remote uniaxial tension σ_∞ in plane strain are given in polar coordinates as:

$$\sigma_{rr} = (\sigma_\infty/2)(1+\cos 2\omega) \qquad \text{(equs.2.2)}$$

$$\sigma_{\omega\omega} = (\sigma_\infty/2)(1-\cos 2\omega)$$

$$\sigma_{r\omega} = -(\sigma_\infty/2)\sin 2\omega$$

$$u_{rr} = ((\sigma_\infty a)/(4G))(1-2\mu+\cos 2\omega)$$

$$u_{\omega\omega} = -((\sigma_\infty a)/(4G))\sin 2\omega.$$

If the constants A, B and C are adjusted such that the stress fields in equs.2.1 and equs.2.2 are equal and opposite on the path along the interface between the matrix and a circular inclusion, the resultant stress field is zero on the interface. The 'inclusion' then acts as a free void and the sum of the two corresponding displacement fields gives the displacement field around a cylindrical void subject to uniaxial tension in plane strain. Similarly if A, B and C are adjusted such that the displacement fields in equs.2.1 and equs.2.2 are equal and opposite on the path bounding a circular inclusion, the resultant displacement field is zero on the inclusion-matrix interface. This is the boundary condition appropriate to a rigid inclusion and the sum of the two corresponding stress fields gives the stress field around a rigid cylindrical inclusion subject to uniaxial tension in plane strain. For incompressible deformation, Poisson's ratio μ is 0.5 and Goodier calculates the constants A, B and C for the case of the

rigid inclusion to be:

$$A = -((\sigma_\infty a^2)/(4G))(1-2\mu) = 0$$

$$B = -((\sigma_\infty a^4)/(4G))/(3-4\mu) = -((\sigma_\infty a^4)/(4G))$$

$$C = -((\sigma_\infty a^2)/(2G))(3-4\mu) = -((\sigma_\infty a^2)/(2G)).$$

Inserting these values into equs.2.1, the resultant elastic stress field for uniaxial tension is:

$$\sigma_{rr} = \sigma_\infty(-(3/2)(a/r)^4+2(a/r)^2+(1/2))\cos 2\omega+(\sigma/2)$$

$$\sigma_{\omega\omega} = \sigma_\infty((3/2)(a/r)^4-(1/2))\cos 2\omega+(\sigma/2)$$

$$\sigma_{r\omega} = \sigma_\infty(-(3/2)(a/r)^4+(a/r)^2-(1/2))\sin 2\omega.$$

The maximum values of the elastic stress components occur at r = a on the interface and the maximum normal interfacial stresses at $\omega = 0$ in the direction of the maximum remote principal stress, where the shear stress is zero. In this case the maximum radial stress on the interface of a rigid cylindrical inclusion under a remote uniaxial tensile stress σ_∞ is:

$$\sigma_{rrmax} = 1.5\ \sigma_\infty.$$

The solution for multiaxial loading can be found from the uniaxial solution by superposition and in particular, the elastic stress field for remote pure shear τ_∞ is found by adding the stress field for a uniaxial tension of magnitude $+\tau_\infty$ to that for a uniaxial tension of magnitude $-\tau_\infty$ rotated through an angle of $\pi/2$ to the

loading direction (fig.2.2), to give:

$$\sigma_{rr} = \tau_\infty(-(3/2)(a/r)^4+2(a/r)^2+(1/2))\cos 2\omega+(\tau_\infty/2)-$$
$$\tau_\infty(-(3/2)(a/r)^4+2(a/r)^2+(1/2))\cos 2(\omega+\pi/2)-(\tau_\infty/2)$$

$$\sigma_{\omega\omega} = \tau_\infty((3/2)(a/r)^4-(1/2))\cos 2\omega+(\tau_\infty/2)-$$
$$\tau_\infty((3/2)(a/r)^4-(1/2))\cos 2(\omega+\pi/2)-\tau_\infty/2)$$

$$\sigma_{r\omega} = \tau_\infty(-(3/2)(a/r)^4+(a/r)^2-(1/2))\sin 2\omega-$$
$$\tau_\infty(-(3/2)(a/r)^4+(a/r)^2-(1/2))\sin 2(\omega+\pi/2).$$

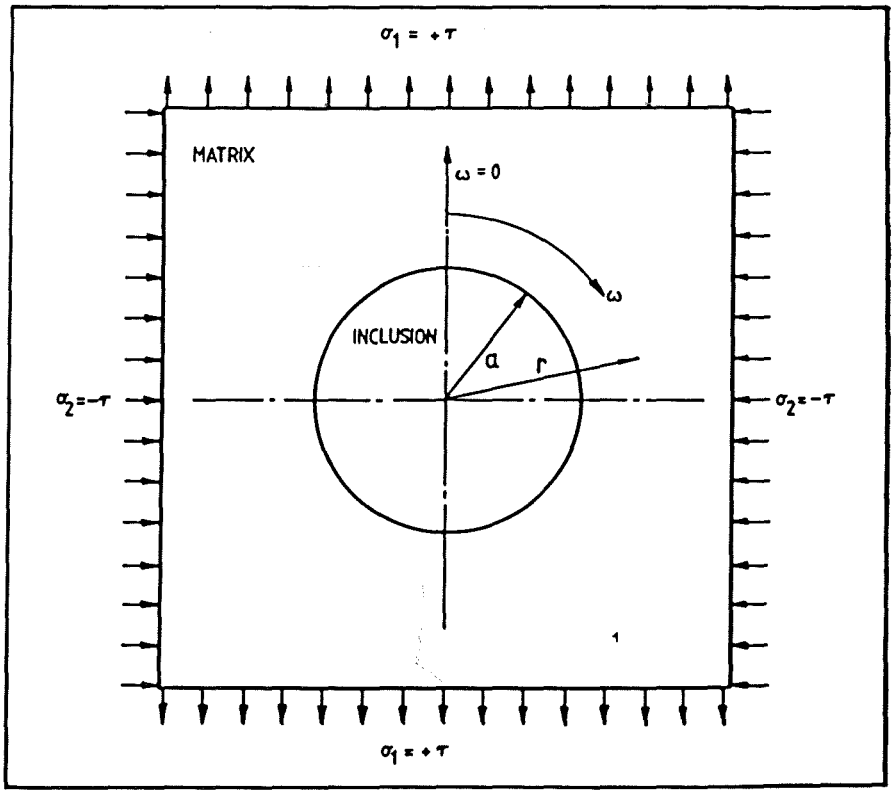

Fig.2.2. A cylindrical inclusion subject to pure shear loading.

With the identity:

$$\cos 2(\omega+\pi/2) = \cos(2\omega+\pi) = -\cos 2\omega$$

and:

$$\sin 2(\omega+\pi/2) = \sin(2\omega+\pi) = -\sin 2\omega$$

these become:

$$\sigma_{rr} = \tau_{\infty}(-3(a/r)^4+4(a/r)^2+1)\cos 2\omega$$

$$\sigma_{\omega\omega} = \tau_{\infty}(3(a/r)^4-1)\cos 2\omega$$

$$\sigma_{r\omega} = \tau_{\infty}(-3(a/r)^4+2(a/r)^2-1)\sin 2\omega.$$

The remaining stress component σ_{zz} may be found from the plane strain condition $e_{zz} = 0$ which implies that:

$$\sigma_{zz} - \mu(\sigma_{rr} + \sigma_{\omega\omega}) = 0.$$

and with the incompressibility condition $\mu = 0.5$, then for plane strain under pure shear:

$$\sigma_{zz} = 2\tau_{\infty}(a/r)^2\cos 2\omega$$

Again the maximum values of the elastic stress components occur at r = a on the inclusion-matrix interface. In this case:

$$\sigma_{rr} = 2\tau_{\infty}\cos 2\omega$$

$$\sigma_{\omega\omega} = 2\tau_{\infty}\cos 2\omega$$

$$\sigma_{r\omega} = -2\tau_{\infty}\sin 2\omega$$

$$\sigma_{zz} = 2\tau_{\infty}\cos 2\omega$$

and the maximum values of the interfacial stresses occur at $\omega = 0$, where the shear stress is zero, giving:

$$\sigma_{rrmax} = 2\tau_{\infty} \qquad \text{(equ.2.3)}$$

$$\sigma_{\omega\omega max} = 2\tau_{\infty}.$$

σ_{rr} is then a principal stress. The maximum shear stress occurs at $\omega = \pi/4$ and has a magnitude of:

$$\sigma_{r\omega max} = -2\tau_{\infty}.$$

Hence the maximum radial stress on the interface is twice the applied shear stress and occurs in the direction of the greatest principal stress. The remote principal stresses for an incompressible material in plane strain and subject to pure shear are:

$$\sigma_1 = \tau_{\infty} \qquad \sigma_2 = -\tau_{\infty} \qquad \sigma_3 = 0$$

and with:

$$\bar{\sigma} = \sqrt{3}\tau,$$

the maximum interfacial radial stress (equ.2.3) may be written as:

$$\sigma_{rrmax} = (2/\sqrt{3})\bar{\sigma}_{\infty}.$$

Since the principle of superposition is valid for linear elastic materials, the stress field for any plane strain triaxial loading may be obtained by summing a remote pure shear field and the appropriate hydrostatic component $\sigma_{m\infty}$ to give:

$$\sigma_{rrmax} = 1.15\bar{\sigma}_{\infty} + \sigma_{m\infty}$$

For a rigid spherical inclusion in uniaxial tension, Goodier (1933) similarly finds that:

$$\sigma_{rrmax} = 2\sigma_{\infty}$$

due to a remote uniaxial stress σ_{∞}. This can also be generalised to axisymmetric loading by superimposing the appropriate hydrostatic stress to give:

$$\sigma_{rrmax} = 1.67\bar{\sigma}_{\infty} + \sigma_{m\infty}.$$

2.1.2. ELASTIC/PLASTIC SOLUTIONS.

The problem of a cylindrical elastic inclusion in an elastic/plastic matrix has been addressed by Orr and Brown (1974). Both non-hardening and linear-hardening matrices were considered, the latter having a stress-strain curve with a slope of E/40 in the plastic regime. Plane strain finite difference solutions for different biaxial loadings were found, the results indicating that the stress distribution around the interface for a triaxial loading is simply the sum of the stresses due to the pure shear component and the hydrostatic or mean component. While superposition may not rigorously be applied to elastic/plastic problems, this result is of considerable practical use. In all their solutions, Orr and Brown (1974) found little intensification of stress on the interface in the direction of the maximum principal stress but that a stress concentration exists elsewhere, the interfacial radial stress reaching a maximum at about $\pi/8$ from this direction. If the effective stress at first yield from a

uniaxial tensile test is σ_0, then for remote plastic strains of the order of 15 times the yield strain, the distribution of the radial stress around the inclusion takes the approximate form:

$$\sigma_{rr} = 1.75\sigma_0 \sin 4\omega + \sigma_{m\infty} \quad \pi/24 < \omega < 11\pi/24$$

in the non-hardening case, while for the hardening solution:

$$\sigma_{rr} = 2.10\sigma_0 \sin 4\omega + \sigma_{m\infty} \quad \pi/24 < \omega < 11\pi/24.$$

Interestingly, the solution of Orr and Brown (1974) did not reach a steady state even at such large plastic strains and these expressions are not applicable throughout the loading history. This was considered as reflecting the method of solution and in particular the starting conditions for the finite difference routines under which the inclusion and matrix were assumed to have identical elastic properties up to first yield. Beyond yield, the inclusion was held rigid since the elastic strains were believed to become less significant as plastic strain developed.

A useful feature of the Orr and Brown (1974) solution is their plot of the directions of maximum shear strain around the inclusion. This must be very similar to the corresponding plot for a rigid-perfectly plastic matrix containing a rigid inclusion and hence the form of a possible slip-line field may be inferred. Figure 2.3 gives the detail in a quarter of the field. For pure shear the slip-lines remote from the inclusion are at an angle of $\omega = \pi/4$ to the greatest principal stress ($\omega = 0$) and the symmetry of the problem

under reversed loading implies that the slip-lines meeting the inclusion at $\pi/4$ or a multiple of $\pi/4$ must remain straight until they meet the interface. Along any α or β slip-line:

$$\sigma_m + 2k_0 \xi = \text{constant}$$

where ξ is the rotation of the line from some datum and k_0 is the yield stress in pure shear. For a straight slip-line, $\xi = 0$ and hence along the length of the line:

$$\sigma_m = \text{constant}.$$

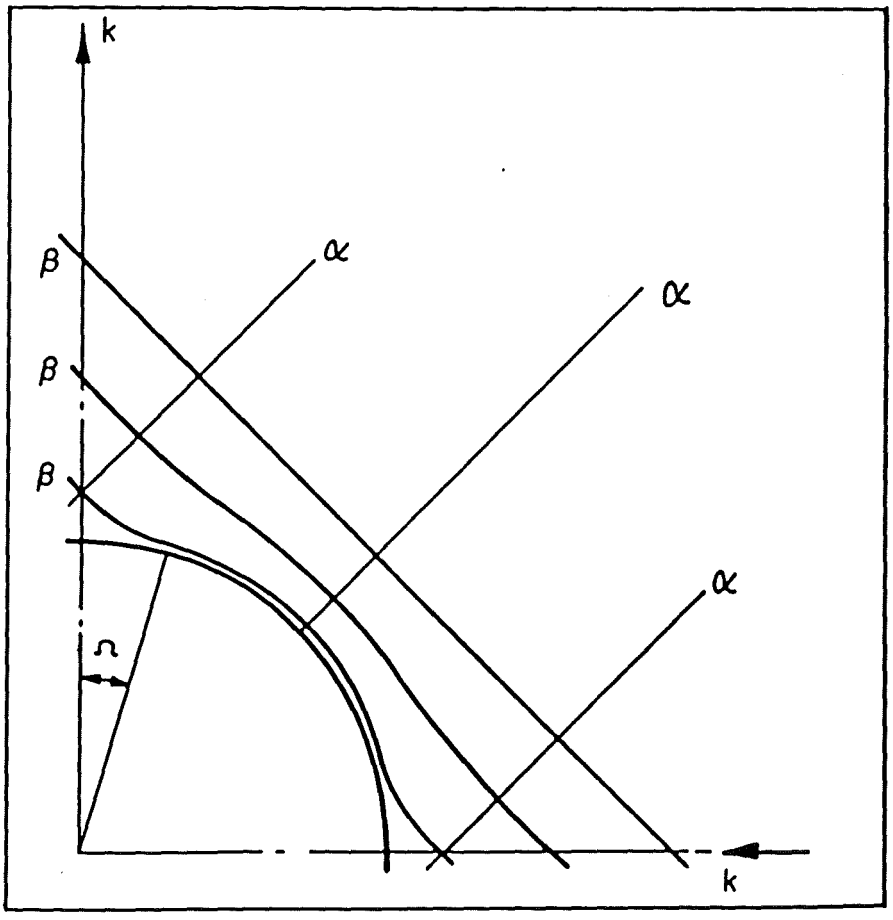

Fig.2.3. The proposed form for the slip-line field around a cylindrical inclusion.

The α-line which meets the inclusion at $\pi/4$ in fig.2.3 is straight and it follows that the mean stress on the interface is the same as that in the remote field. Since the remote mean stress is zero in pure shear then:

$$\sigma_m = 0 \text{ at } \omega = \pi/4 \qquad \text{(equ.2.4)}.$$

For a plastically deforming matrix adjacent to a rigid inclusion the α-slip-lines must meet the interface radially and the β-lines tangentially. The β-line tangential to the interface must cross the remote tensile axis at $\pi/4$ if it is to be orthogonal to the corresponding α-line on the other side of the axis. This β-line must therefore break away from the interface at some angle Ω (fig. 2.3) which is indeterminate at present but has limiting values of $\Omega = 0$ and $\Omega = \pi/4$. The Hencky equation for a β-line tangential to the inclusion gives:

$$\sigma_m + 2k_0\omega = \text{constant}$$

if the rotation is measured from the ω-axis. Inserting the condition in equ.2.4, then around the inclusion:

$$2k_0\pi/4 = \text{constant}$$

$$\Rightarrow \sigma_m = 2k_0(\pi/4 - \omega) \qquad \text{(equ.2.5)}.$$

For any slip-line:

$$\sigma_{\alpha\alpha} = \sigma_m$$

and since the α-lines are normal to the interface in this case:

$$\sigma_{\alpha\alpha} = \sigma_{rr}$$

which, with equ.2.5, leads to:

$$\sigma_{rr} = 2k_0(\pi/4 - \omega).$$

With:

$$\sqrt{3}k_0 = \sigma_0$$

then for a perfectly plastic matrix:

$$\sigma_{rr} = 1.15\sigma_0(\pi/4 - \omega)$$

For $\Omega = \pi/4$ all but the point on the interface at $\pi/4$ is rigid and the straight slip-lines form a square which circumscribes the inclusion. In the case when Ω approaches 0, the maximum possible interfacial radial stress approaches $0.5\pi k_0$ or alternatively:

$$\sigma_{rrmax} = 0.9\sigma_0$$

in the direction of the maximum principal stress ($\omega = 0$). This case of $\Omega = 0$ gives an upper limit to the interfacial stress concentration. Superposition of a hydrostatic stress does not change the nature of the slip-line field for an incompressible material and leads finally to an expression of the form:

$$\sigma_{rrmax} = 0.9\sigma_0 + \sigma_{m\infty}.$$

Argon, Im and Safoglu (1975) modelled an inclusion in plane strain as a rigid cylinder embedded in a finite element mesh of CST elements. The stress and strain fields in the deforming matrix were evaluated for an applied shear loading using the elastic-plastic finite element program of Marcal and King (1967) and the results showed that when full plasticity develops in a linear-elastic/perfectly-plastic matrix, the interfacial radial stress is given approximately by:

$$\sigma_{rr} = 1.5k_0\cos 2\omega$$

This implies a maximum value of σ_{rr} at $\omega = 0$ of:

$$\sigma_{rrmax} = 1.5k_0$$

in accord with $(\pi/2)k_0$ for the limiting value of the slip-line field solution. The final remote plastic strain reached in this analysis was only of the order of the yield strain but it was felt that while an analysis which continued well into the plastic regime of the stress -strain curve would give different results, the differences would not be significant enough to merit increased computing costs. This result was therefore interpreted as a steady state solution, in contrast with the work of Orr and Brown (1974). In terms of the effective stress, Argon, Im and Safoglu (1975) predicted a maximum value of σ_{rr} of:

$$\sigma_{rrmax} = 0.87\sigma_0 \qquad \text{(equ.2.6)}.$$

Following the results of McClintock and Rhee (1962) for strain fields, the stress behaviour of strain hardening materials was viewed as being intermediate between non-hardening and purely elastic materials. In-

terpolation between the stress concentration resulting from the finite element analysis of a non-hardening material (equ.2.6) and Goodier's (1933) analytic elastic solution (equ.2.3) gave:

$$\sigma_{rrmax} = \bar{\sigma}_{\infty}$$

which was taken to represent the approximate behaviour of strain hardening materials. For triaxial stress states the mean stress $\sigma_{m\infty}$ was added to give the simple result:

$$\sigma_{rrmax} = \bar{\sigma}_{\infty} + \sigma_{m\infty}.$$

Inclusion	Matrix	Source	σ_{rrmax}
Rigid cylinder	Elastic	Goodier (1933)	$1.15\bar{\sigma} + \sigma_{m\infty}$
Rigid sphere	Elastic	Goodier (1933)	$1.67\bar{\sigma} + \sigma_{m\infty}$
Elastic cylinder	Elastic/plastic non-hardening	Orr and Brown (1974)	$1.75\sigma_0 \sin 4\omega + \sigma_{m\infty}$ $\pi/24 < \omega < 11\pi/24$
Elastic cylinder	Elastic/plastic linear-hardening	Orr and Brown (1974)	$2.10\sigma_0 \sin 4\omega + \sigma_{m\infty}$ $\pi/24 < \omega < 11\pi/24$
Rigid cylinder	Rigid/plastic non-hardening	Slip-line field	$0.9\sigma_0 + \sigma_{m\infty}$
Rigid cylinder	Elastic/plastic hardening	Argon, Im and Safoglu (1975)	$\bar{\sigma}_{\infty} + \sigma_{m\infty}$

Fig.2.4. A summary of existing expressions for the maximum interfacial radial stress around an inclusion.

2.2. VOID NUCLEATION.

Microscopic voids can occur in materials for a variety of reasons and while the homogeneous nucleation of cavities is not uncommon, by vacancy condensation or diffusion for example, in most cases heterogeneous nucleation occurs at sites such as grain boundaries or hard particles. For the latter case, Puttick (1959) has noted that as deformation continues in a ductile material, the stress and strain fields near such particles increase until the inclusion cracks or debonds from the matrix around a greater or lesser part of the inclusion/matrix interface. Since the deformation at which this occurs may comprise a significant part of the ductility, the nucleation of voids at hard particles has received considerable attention and has been studied both in terms of dislocation/particle interaction (Goods and Brown (1979)) and in terms of continuum plasticity (Argon, Im and Safoglu (1975)). Various nucleation criteria have been proposed and while two-parameter criteria have been suggested (McClintock (1968)), most authors favour a single criterion for the onset of nucleation, based on an energy balance or the local attainment of the interfacial cohesive strength or a critical plastic strain.

On the basis of the strain energy released by interfacial separation to form new surfaces, Gurland and Plateau (1963) derived an energy condition for nucleation, while from a combined micromechanical and continuum approach to the energetics of nucleation, Brown and Stobbs (1976) found that, for particles around which secondary slip produces plastic relaxation, the onset of nucleation occurs at a remote strain given by:

$$e^{p}_{c\infty} = (3\gamma)/(Gb).$$

Here γ is the free surface energy and nucleation is independent of the particle size. This expression was found to give an overestimate of the nucleation strain but may be corrected by allowing for partial nucleation around part of the interface. Such an energy criterion is necessary but for nucleation to be guaranteed the interfacial cohesive strength must also be exceeded. For very small particles, the latter condition is satisfied first and nucleation occurs when the energetics are favourable. Conversely, for large particles, the energy criterion is satisfied almost upon yielding (Tanaka, Mori and Nakamura (1970)) and the strength of the interface provides a sufficient condition for nucleation. This introduces a scale effect in addition to any functional dependence of nucleation on the particle radius and is well supported by experiments (Goods and Brown (1979)).

Considering the local stress σ at an inclusion to be dominated by the dislocation density, Brown and Stobbs (1976) found that:

$$e^{p}_{c\infty} = (\sigma)^2/(G\alpha)^2(r/b).$$

in which the nucleation strain increases linearly with the particle size and is a function of the forest hardening factor α. Since dislocation density depends on deformation then $e^{p}_{c\infty}$, although expressed in terms of the interfacial stress, is fundamentally dependent on the remote strain. The experimental evidence for a minimum nucleation strain is however conflicting and while the work of Goods and Nix (1978) on a silver matrix with and without pre-existing voids implies such a minimum strain, Gurland (1972) failed to find any evidence in spheroidized steels.

In the spirit of Eshelby's (1957) method for ellipsoidal inclusions in a deforming matrix, Ashby (1966) devised a model in which the misfit between a deforming matrix and a rigid particle was accommodated by the punching of prismatic loops of dislocations. However, as the rate of dislocation storage increases, plastic deformation near a particle becomes more difficult and the local stress approaches the interfacial cohesive strength. Applying this argument to the analysis of small particles, Argon, Im and Safoglu (1973) proposed a nucleation criterion in terms of the maximum interfacial radial stress. While at the smaller size scale this may again be argued to be fundamentally strain dependent, near larger particles the dislocation structure is not the major influence on the local stress and a continuum approach may be taken to nucleation. Argon, Im and Safoglu (1973) then proposed an interfacial stress criterion, sufficient for such particles, which fundamentally involves the remote stress state as well as the deformation.

In the particular case of Swedish Iron, the inclusions have sizes of micron order and the local fields near the interface result largely from the remote deformation and stress state. On this basis it is argued here that the nucleation conditions in this material are derivable from a continuum approach.

2.3. VOIDS IN A HOMOGENEOUS DEFORMING MATRIX.

Stable void growth in a continuing deformation field accounts for much of the plastic strain between nucleation and the initiation of failure and is therefore an important aspect of the failure process. Again the local stress and strain fields produced by the remote loading will be perturbed in the presence of a void and these local fields will determine the mechanics of the growth of an isolated void up to coalescence.

Provided the eccentricity of the void is small, Goodier's (1933) analysis is applicable to a single void in an elastic matrix. Presented in section 2.1 for a rigid inclusion, the analysis may be applied to an 'inclusion' of zero stiffness, ie a void, by appropriate choice of the constants A, B and C in equs.2.1. These must now be chosen such that the resultant stress obtained by superposition of equs.2.1 and equs.2.2 is zero on either side of a closed path circumscribing the inclusion, which then acts as a free surface. In this case, Goodier (1933) gives:

$$A = (\sigma_\infty a^2)/(4G)$$

$$B = (\sigma_\infty a^4)/(4G)$$

$$C = (\sigma_\infty a^2)/(2G)$$

for a void under a remote uniaxial tensile stress σ_∞. Inserting these values into equs.2.1 for the stress components leads to:

$$\sigma_{rr} = \sigma_\infty(-(1/2)(a/r)^2+((3/2)(a/r)^4- 2(a/r)^2+(1/2))\cos 2\omega)+(\sigma_\infty/2)$$

$$\sigma_{\omega\omega} = \sigma_\infty((1/2)(a/r)^2-((3/2)(a/r)^4+(1/2))\cos 2\omega)+(\sigma_\infty/2)$$

$$\sigma_{r\omega} = \sigma_\infty((3/2)(a/r)^4-(a/r)^2-(1/2))\sin 2\omega$$

and again the result for pure shear τ_∞ is found by superposition of two perpendicular uniaxial loads to be:

$$\sigma_{rr} = \tau_\infty(3(a/r)^4-4(a/r)^2+1)\cos 2\omega$$

$$\sigma_{\omega\omega} = \tau_\infty(-3(a/r)^4-1)\cos 2\omega$$

$$\sigma_{r\omega} = \tau_\infty(3(a/r)^4-2(a/r)^2-1)\sin 2\omega.$$

At the interface r = a these reduce to the boundary conditions:

$$\sigma_{rr} = \sigma_{r\omega} = 0$$

The expansion of an ellipsoidal void in a general triaxial deformation field has not yet been fully described but both Rice and Tracey (1969) and McClintock (1968) give solutions for the special cases of spherical symmetry and generalised plane strain respectively. More recently the problem of the asymptotic shape assumed by an initially spherical void has been addressed by Budiansky, Hutchinson and Slutsky (1981).

Substituting the polar equilibrium and strain-displacement relations into the appropriate stress-strain law, McClintock (1968) gives:

$$d(\ln(R/R_0)) = \sqrt{3}de_{r\infty}\sinh(\sqrt{3}\sigma_{r\infty}/(\sigma_{r\infty} - \sigma_{z\infty})) + de_{r\infty} \quad \text{(equ.2.7)}$$

for a circular hole of radius R in a rigid, perfectly plastic medium and:

$$\ln(R/R_0) = 3e_{r\infty}\sigma_{r\infty}/(\sigma_{r\infty} - \sigma_{z\infty}) + e_{r\infty} \quad \text{(equ.2.8)}$$

for a hole in a linear viscous material. No solution for a non-circular hole in a plastic medium being available, McClintock (1968) considered the expressions derived by Berg (1962) for an elliptical hole in a linear viscous material:

$$\ln(R/R_0) = t/(4\mu)(\sigma_{a\infty} + \sigma_{b\infty}) \quad \text{(equs.2.9)}$$

$$M = (\sigma_{a\infty} - \sigma_{b\infty})/(\sigma_{a\infty} + \sigma_{b\infty}) + (M_0 - (\sigma_{a\infty} - \sigma_{b\infty})/(\sigma_{a\infty} + \sigma_{b\infty}))\exp(-t/(2\mu)(\sigma_{a\infty} + \sigma_{b\infty}))$$

where R is the average radius of the ellipse, defined in terms of the semi-major axis a and semi-minor axis b as:

$$R = (1/2)(a + b) \quad \text{(equ.2.10)}$$

and M is the eccentricity of the ellipse defined as:

$$M = (a - b)/(a + b) \quad \text{(equ.2.11).}$$

For comparison with plastic materials, McClintock (1968) replaced Berg's (1962) ratio of time t to viscosity μ by an expression in terms of the effective stress and effective plastic strain (defined in section 3.1):

$$t/\mu = 3\bar{e}^{p}_{\infty}/\bar{\sigma}_{\infty}$$

and, with this replacement, equs.2.9 lead, for an elliptical hole in a linear viscous material, to the expressions:

$$\ln(R/R_0) = (3/4)\bar{e}^{p}_{\infty}(\sigma_{a\infty}+\sigma_{b\infty})/\bar{\sigma}_{\infty} + (1/2)(e_{a\infty}+e_{b\infty})$$

$$M = (\sigma_{a\infty}-\sigma_{b\infty})/(\sigma_{a\infty}+\sigma_{b\infty}) + (M_0 - (\sigma_{a\infty}-\sigma_{b\infty})/(\sigma_{a\infty}+\sigma_{b\infty}))\exp(-(3/2)\bar{e}^{p}_{\infty}(\sigma_{a\infty}+\sigma_{b\infty})/\bar{\sigma}_{\infty})$$

(equs.2.12)

The strain term on the right hand side of the first of equs.2.12 was introduced to give solutions for generalised plane strain in which the strain normal to the ellipse is a constant but not necessarily zero. McClintock (1968) then looked at the differences between the rigid, perfectly plastic and the linear viscous expressions for a circular hole (equ.2.7 and equ.2.8) and proposed that similar differences exist between the corresponding expressions for an elliptical hole. With due regard for the occurrence of poles and zeros in the equations for limiting cases of applied loadings, the desired plastic expressions were derived by extension of equs.2.12 to give:

$$\ln(R/R_0) = (\sqrt{3}/2)(\bar{e}^p_\infty/(1-n))$$
$$\sinh((\sqrt{3}/2)(1-n)(\sigma_{a\infty}+\sigma_{b\infty})/\bar{\sigma}_\infty)+(1/2)(e_{a\infty}+e_{b\infty})$$

(equs.2.13)

$$M = (\sigma_{a\infty}-\sigma_{b\infty})/(\sigma_{a\infty}+\sigma_{b\infty}) +$$
$$(M_0 - (\sigma_{a\infty}-\sigma_{b\infty})/(\sigma_{a\infty}+\sigma_{b\infty}))$$
$$\exp(-\sqrt{3}(\bar{e}^p_\infty/(1-n))\sinh((\sqrt{3}/2)(1-n)(\sigma_{a\infty}+\sigma_{b\infty})/\bar{\sigma}_\infty))$$

in which the terms in n were introduced in accordance with McClintock and Rhee (1962) by interpolation between the rigid/perfectly-plastic expressions and the linear-viscous expressions, to account for strain hardening in a material with a power law constitutive equation of the form:

$$\bar{\sigma} = \sigma_0 \bar{e}^{p^n} \qquad \text{(equ.2.14).}$$

The growth of initially spherical voids in multiaxial deformation fields has been considered by Rice and Tracey (1969) who found that for rigid/perfectly-plastic materials, the velocity field v_i in a material subject to a remote strain rate $e_{ij\infty}$ is such as to minimise the functional:

$$Q(v) = \int (s_{ij}(v)-s_{ij\infty})e_{ij\infty}\, dV - \sigma_{ij\infty} \int n_i v_j dS$$

where n_i is the unit normal drawn into the matrix from the surface S_v of the void and V is the volume of material outside the void. For uniaxial remote deformation, the local strain rate field was assumed to have the form:

$$e_{ij} = e_{ij\infty} + De^{D}_{ij} + Ee^{E}_{ij}$$

in which e^{D}_{ij} is a spherically symmetric field producing changes in the volume of the void but not in its shape, e^{E}_{ij} is a volume-preserving shape-changing field, and the remaining term is the strain field to meet the remote boundary conditions. Using a Rayleigh-Ritz procedure to minimise their functional with respect to the constants D and E, Rice and Tracey (1969) found that the volume changing aspect of void growth, expressed through the parameter:

$$D = (1/R)(dR/d\bar{e}^{p}_{\infty})$$

overwhelmed the shape changing aspect and that void growth was not particularly sensitive to the shape changing parameter E. This result was assumed to hold under general multiaxial remote strain fields and considering only the volume changing aspects of the deformation, the functional to be minimised becomes:

$$\int (s_{ij}(D)-s_{ij\infty})e^{D}_{ij}dV - \sigma_{m\infty} \int n_i v^{D}_{i} dS.$$

D was then found to have the approximate form:

$$D = C(v)\exp(\sigma_{m\infty}/(2\sigma_0)) \qquad \text{(equ.2.15)}$$

where C(v) is a function of the strain state, expressed through the parameter v with a domain of -1, corresponding to remote uniaxial compression or biaxial tension, to +1 for remote uniaxial tension or biaxial compresssion. C(v) was found to be approximately:

$$C(v) = 0.279 + 0.004v$$

and is thus only weakly dependent on the remote strain state, which in practice influences the void growth rate only through the effective strain. The high triaxiality result was then assumed to adequately describe the growth rate even at low stress levels when the dilational growth does not dominate the shape changing growth. For uniaxial tension C(v) was obtained as 0.282. Replacing the exponential in equ.2.15 by a hyperbolic function such that:

$$D = 0.558 \sinh(\sigma_{m\infty}/(2\sigma_0)) + 0.008v\cosh(\sigma_{m\infty}/(2\sigma_0))$$

reproduces the exponential tail at both positive and negative triaxialities and allows the same expression to be used in both cases.

Budiansky, Hutchinson and Slutsky (1981) have also considered the deformation of an isolated axisymmetric void, in a stress state characterised by the ratio of the longitudinal stress to the transverse stress, σ_1/σ_2. By adjusting this ratio, the evolution of the voids in a range of stress states was studied and in particular the asymptotic shape assumed by the void as $\bar{e}^p_\infty$ tends to infinity. Starting with Eshelby's (1981) solution for an ellipsoidal void, numerical solutions were obtained for the void growth rate in a variety of material types and approximate analytic expressions given for such rates in stress states for which $\sigma_{m\infty}/\bar{\sigma}_\infty$ exceeds unity. For initially cylindrical voids in a rigid/perfectly-plastic materials Budiansky, Hutchinson and Slutsky (1981) found that:

$$(1/V)(dV/d\bar{e}^p_\infty) = \sqrt{3}\sinh(\sqrt{3}\sigma_2/(\sigma_1-\sigma_2))$$

which agrees with McClintock's (1968) formula. Further, by neglecting the shape-changing aspect of the deformation field of an initially shperical void, an approximate expression was derived which reduces in the limiting case of a rigid/perfectly-plastic material to:

$$(1/V)(dV/d\bar{e}^{p}_{\infty}) = 0.850 \exp((3/2)|\sigma_{m\infty}/\bar{\sigma}_{\infty}|)$$

in accord with the high triaxiality results of Rice and Tracey (1969).

A feature of the results of Budiansky, Hutchinson and Slutsky (1981) is the oblate asymptotic shape assumed by initially spherical voids in highly triaxial stress fields even when σ_1 is positive. This possibility was discounted by Rice and Tracey (1969) but is believed be the norm by Budiansky, Hutchinson and Slutsky (1981) for such loading. The relevance of oblate shapes to failure by void coalescence is noted, as is the strong influence of initial porosity on the growth rates of nonlinear materials, which argues against the indiscriminate extension of the isolated void in an infinite matrix to materials with finite porosity, and vice versa.

McClintock's (1968) solution is strictly only applicable to cylindrical voids in generalised plane strain but equs.2.13 give good agreement with experimental results and in particular with the observed shape change of highly eccentric voids. These equations were thus chosen as the basis for the numerical analysis of the voids in Swedish Iron which develop prolate shapes in the experimentally generated stress states.

2.4. FAILURE INITIATION.

Voids grown in isolation in a continuing deformation field eventually reach a size where local perturbations in the stress and strain fields interact to produce coalescence. This results in the formation of an internal crack, accompanied by a drop in the load-bearing capacity of the material, which has been identified by Hancock and Mackenzie (1976) as 'failure initiation'. The mechanism by which failure initiates is currently the most controversial area and it is not clear whether the crack results from true normal rupture or from zig-zag shear failures in the intervoid ligaments. In either case further deformation causes the crack to propagate through previously damaged material in a direction macroscopically normal to the maximum principal direction of a simple tension specimen, until the free surface is approached and strain concentrates on an inclined plane to produce the familiar cup-and-cone fracture.

Insight into the growth of a single void during plastic deformation has been provided by the work of McClintock (1968), Rice and Tracey (1969) and Budiansky, Hutchinson and Slutsky (1981) from which the size and shape of voids at failure can be estimated. A common feature of these solutions is the exponential amplification of the growth rate by the stress triaxiality $\sigma_{m\infty}/\bar{\sigma}_{\infty}$ in perfectly plastic materials and, since stable void growth accounts for much of the plastic strain before failure, the ductility of a material often depends strongly on triaxiality, as observed by Hancock and Mackenzie (1976). However predictions of ductility limited by the coalescence of voids have usually been based on the analysis of a periodic array of cells (Needleman (1972), each representative of the average mater-

ial, but McClintock (1968) and Hancock and Mackenzie(1976) have shown that in a homogeneous strain field there is insufficient growth to produce failure by coalescence between the voids in adjacent representative cells. There must therefore be a mechanism by which the locally high strain concentrations necessary for void coalescence may be produced within the bounds of the average aggregate material.

In an analysis of cylindrical voids in a regular 2-space array , Brown and Embury (1973) considered that coalescence would follow the shear bands admitted when the void length equals the spacing. Such a simple failure criterion is appealing but the kinematics of the flow field for the general 3-space case are not obvious. A 3-space failure model has been developed by Thomason (1984), who believes that coalescence must be analysed in terms of the mechanics of discrete voids, and obtained an upper-bound solution to the failure load from a flow field compatible with the deformation of a regular array of voids embedded within a non-hardening matrix. A localisation criterion was then proposed, based on the limit load in the intervoid ligament, which is reported to be in good agreement with experiments. Such a criterion takes account of the destabilising influence of void growth in a continuing deformation field but specimens which have been precompressed to lower the hardening rate of the matrix and suppress the growth of nucleated voids show, on subsequent deformation under positive mean stress, greatly reduced ductility resulting from enhanced void growth rates compared to non-predeformed specimens. This implies a crucial role for the stabilising influence of matrix strain hardening in inhibiting strain concentrations, in opposition to the effect of void growth. Thomason's (1984) analysis however, denies a major role for this parameter.

In contrast to the discrete void approach, the role of strain hardening is emphasised in the continuum approach of Rudnicki and Rice (1975). This approach is thus preferred in the current work. Rather than concentrate on the mechanism by which discrete voids grow and interact, Rudnicki and Rice (1975) took the view that ductility is limited by a change from a homogeneous flow field to a localised deformation mode which permits unbounded strains in a shear band. Localisation was analysed as a bifurcation in this flow field, given appropriate constitutive equations. The appropriate equations admit the possibility of plastic dilation and strain softening by void growth, as discussed by Berg (1970), Gurson (1977) and Tvergaard (1981), and must take account of other destabilising features such as yield vertices due to anisotropy and non-normality of plastic flow. Rice (1976) however has noted that with realistic average porosities the predicted bifurcation strain is still too high compared to measured values to be directly responsible for failure. This may be reconciled by noting that in real materials the random spatial distribution of particles from which voids initiate implies the existence of inhomogeneities in which the local concentration of voids is significantly greater than average. Since failure is likely to initiate in regions where the random distribution of inclusions leads to higher than average initial porosities (fig.2.5) then these statistical inhomogeneities must be modelled in continuum terms. Yamamoto (1978) idealised such regions within the material as unbounded planar bands of imperfection which allow homogeneous deformation fields to be established inside and outside the band while a finite strain discontinuity permits the deformation rate in the band to be very much greater than that in the remote field. As a consequence of the strain concentration, the local conditions for unbounded deformation, as de-

fined by Rudnicki and Rice (1975), can be met at realistic values of the remote strain.

The strain concentrations within inhomogeneities are largely determined by the relative hardening rates on either side of the interface, with less positive hardening rates in the inhomogeneity tending to favour higher strain concentrations. In the case of the unbounded planar shear band of Yamamoto (1978), very high strain concentrations become possible as the hardening rate approaches zero in the band at correspondingly high values of the remote deformation. The physical sense of this can be appreciated from an argument by Mudry (1982) who assumed that the strain within the highly porous imperfection is simply that necessary to maintain the local aggregate effective stress $\bar{\bar{Z}}$ at the same value as $\bar{\bar{Z}}_\infty$ in the less porous environment. The hardening rate within the imperfection will decrease faster than in the average material, producing large strain concentrations as the local hardening rate approaches zero. Assuming that Z_{kk} in the inhomogeneity is equal to that in the average material implies massive void growth rates and ultimate failure within the imperfection. This argument does not constitute a complete solution but illustrates how large strain concentrations may arise in an unbounded band of imperfection. In such a situation, the detailed mechanism of flow localisation and of void coalescence will have little bearing on the remote ductility, which is largely determined by the approach to zero of the local hardening rate in the imperfection.

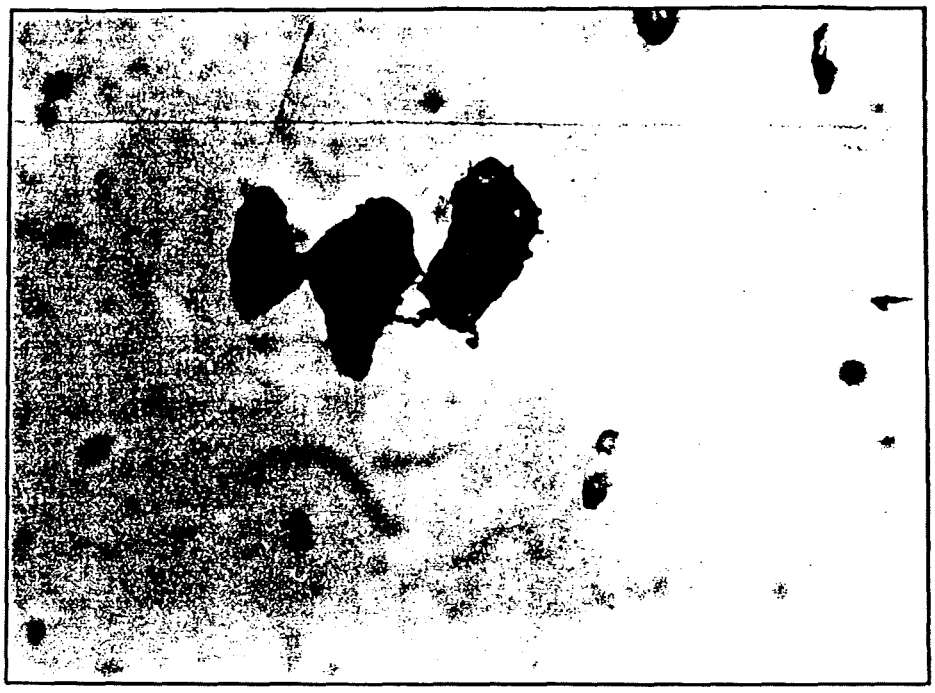

Fig.2.5. The rapid coalescence of voids nucleated from closely spaced inclusions.

Inhomogeneities in the form of parallel bands do exist in wrought steels and are a major cause of their anisotropy. However, while the unbounded planar inhomogeneities of Yamamoto (1978) can be given a direct physical significance in the biaxial loadings typical of sheet metal forming, they were not strictly intended to represent features of the metallurgical microstructure but were a formality by which inhomogeneities could be envisaged at all possible orientations, with localisation occurring at the most favourable angle. As such, the lack of constraint at the ends and their subsequent inability to predict the strain concentrations which promote the propagation of damage, limits their application in the triaxial stress fields typical of many engineering components. The inhomogeneities which exist in

the microstructure of real materials are generally better represented in the form of small volumes of highly porous material completely surrounded by material of average porosity. For such contained inhomogeneities, different behaviour might be expected.

A feature of the Rudnicki and Rice (1975) analysis is the prediction that localisation is favoured in plane strain and inhibited by axisymmetric strain states. Experiments by Hancock and Brown (1983) on structural steels show that for both axisymmetric and plane strain specimens, the ductility is independent of the strain state since the identity of the remote strain state is generally lost within the arbitrarily shaped inhomogeneities in which failure initiates. Furthermore, the microstructure of steels is such that two generations of particles may be identified. Failure can then be produced when the voids nucleated at microscopic carbides grow in the strain fields of voids which nucleate at larger non-metallic inclusions, as observed by Hancock and Mackenzie (1976) and discussed in detail by Tvergaard (1982), who concludes that such a mechanism will not show a strain state effect. The experimental evidence then also favours the view that failure initiates in regions of locally high porosity completely contained by the surrounding material.

An elegant approach to this problem has been made by Ohno and Hutchinson (1984) who considered the case of an axisymmetric band of finite thickness in which the volume fraction of voids was allowed to vary along the length of the band in such a way that the porosity reduced asymptotically to that of the surrounding material. In the limit this imperfection geometry allows contact to be made with Yamamoto's (1978) solution for an infinite band with a uniform distri-

bution of porosity. Rather than adopt a finite element approach, the deformation fields outside and inside the inhomogeneity were simplified to reduce the problem to an integral equation which was solved numerically. To model the effect of inhomogeneities in materials in which the inclusions are well dispersed and randomly distributed in 3-space, the present work adopts a finite element approach to the analysis of equiaxed inhomogeneities. These admit stress and strain gradients inside and outside the patch while the deformation within the patch is kinematically constrained by the surrounding material, which suggests that the size scale of the failure process is of crucial relevance to fracture. Despite such complexities, in many materials the dominant influence is that of void growth as observed by Edelson and Baldwin (1962), who have correlated the ductility with the volume fraction of inclusions.

As yet, the size scale associated with the failure initiation has not been identified and the current work recognises both the presence of discrete inclusions and voids within the bounds of an aggregate porous continuum. A metallurgically simple material has been studied in which the failure mechanism is dominated by voids formed from a single generation of second-phase particles. The work is motivated towards determining the local conditions at failure initiation.

3. THE MECHANICS OF DILATING MATERIALS.

3.1. CLASSICAL PLASTICITY.

3.1.1. THE VON MISES YIELD FUNCTION.

Other than in special circumstances, most structural metals undergo purely elastic deformation up to the yield point, at which plastic flow commences. In the simple case of uniaxial tension for which there is only one non-zero component of the principal stress tensor, say σ, yielding occurs when:

$$\sigma = \sigma_y$$

where σ_y is the current uniaxial yield stress. While σ_y remains at its initial value of σ_0 for non-hardening materials, in the general hardening case σ_y increases with deformation, as depicted in the familiar stress-strain curve of fig.3.1.

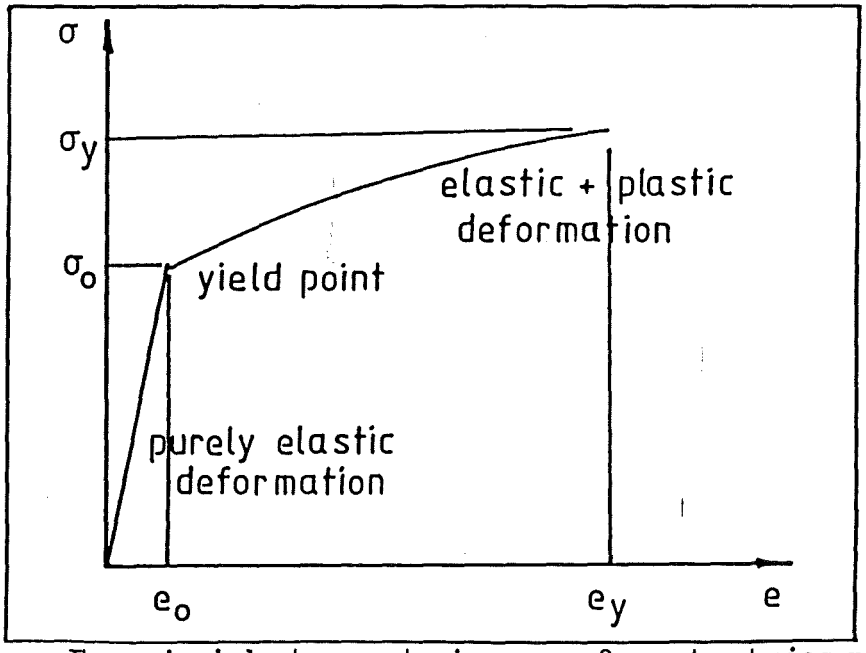

Fig.3.1. The uniaxial stress-strain curve for a hardening material.

It is convenient to define a yield function $\phi(\sigma)$, given in the uniaxial case by:

$$\phi(\sigma) = \sigma - \sigma_y$$

such that

$$\phi(\sigma) = 0 \qquad \text{(equ.3.1)}$$

is a necessary condition for plastic flow. To make the condition sufficient it is necessary to add the consistency condition:

$$d\phi = 0$$

which expresses the idea that during plastic deformation the current stress point in fig.3.1 must not be tending to unload the material. Note that ϕ can never exceed 0 since any attempt to increase σ produces plastic flow which simply increases σ_y by an amount sufficient to satisfy equ.3.1. In the general triaxial case, the problem is to find all possible combinations of the 9 stress components σ_{ij} which produce yielding. The yield function then takes the form:

$$\phi(\sigma_{ij}).$$

which may be represented geometrically as a yield surface in principal stress space. No yield function has been found which suits all materials but the Von Mises expression:

$$\phi = J_2 - k_y^2$$

is applicable to a wide class of engineering materials. Here k_y is the current yield stress in pure shear and J_2 is the second invar-

iant of the stress deviator tensor, defined in one of several equivalent ways as:

$$J_2 = (1/2)s_{ij}s_{ij}$$

where the s_{ij} are the stress deviators. This equation is symmetric in the 3 principal stresses and so describes an isotropic material. For such materials, an effective stress $\bar{\sigma}$ may be usefully defined as:

$$\bar{\sigma}^2 = (3/2)s_{ij}s_{ij} \qquad \text{(equ.3.2)}$$

where the numerical factor is included such that $\bar{\sigma} = \sigma$ in uniaxial tension. This allows the Von Mises yield function for the triaxial case to be written as:

$$\phi = \bar{\sigma} - \sqrt{3}k_y.$$

This general triaxial expression must apply in the degenerate case of uniaxial tension for which the yield function is expressible in terms of the effective stress as:

$$\phi = \bar{\sigma} - \sigma_y.$$

Hence for a material following Von Mises yield criterion:

$$\sigma_y = \sqrt{3}k_y.$$

and even for the triaxial case, the Von Mises yield function may be written:

$$\phi = \bar{\sigma} - \sigma_y \qquad \text{(equ.3.3).}$$

3.1.2. THE PRANDTL-REUSS FLOW RULE.

In the elastic regime of structural steels, strain is proportional to stress and the elastic constitutive equation has the linear form:

$$\sigma_{ij} = C_{ijkl} e^{el}_{kl}$$

? Derived from a potential

where the C_{ijkl} is the tensor of elastic constants and e^{el}_{kl} is the elastic strain tensor. For isotropic materials, the 81 elastic constants have only 2 independent values. Since all of the elastic constants are then functions of the 2 independent values, the latter may be chosen to suit local requirements. For example, if the elastic strains are known, the stresses might be most conveniently found from:

$$\sigma_{ij} = 2G e^{el}_{ij} + \delta_{ij} (K-(2/3)G) e^{el}_{kk}$$

where G is the shear modulus and K is the bulk modulus. Conversely, if the stresses are known, the elastic strains might be found from:

$$e^{el}_{ij} = s_{ij}/(2G) + \delta_{ij} \sigma_{kk}/(9K)$$

or equivalently from:

$$e^{el}_{ij} = (1+\mu)\sigma_{ij}/E - \delta_{ij} \mu\sigma_{kk}/E$$

where E is Young's modulus and μ is Poisson's ratio.

Beyond initial yield the stress-strain curve is usually non-linear but by regarding the material response as piecewise linear, the

total plastic deformation may be determined as the summation of plastic increments de^p_{ij}, obtained from an incremental plastic constitutive equation or flow rule. Melan (1938) proposed that there exists a scalar quantity $f(\sigma_{ij})$, known as the plastic potential, such that:

$$de^p_{ij} = (\partial f/\partial \sigma_{ij})d\lambda$$

where $d\lambda$ is a Lagrange multiplier which varies with deformation. Structural steels which may be described by a Von Mises yield function belong to a wide class of materials which obey normality of the plastic deformation, in that the principal plastic strain increment vector de^p_i is normal to the yield surface at the current stress point. For such normal materials the plastic potential may be identified with the yield function and all possible yield functions then have an associated flow rule defined through:

$$de^p_{ij} = (\partial \emptyset/\partial \sigma_{ij})d\lambda.$$

For a Von Mises yield function this reduces to:

$$de^p_{ij} = s_{ij}d\lambda \qquad \text{(equ.3.4)}.$$

Obviously the establishment of the plastic strain increments requires the evaluation of $d\lambda$ in each increment of deformation. This is facilitated by the definition of an effective plastic strain increment, $d\bar{e}^p$ from:

$$(d\bar{e}^p)^2 = (2/3)d\epsilon^p_{ij}d\epsilon^p_{ij} \qquad \text{(equ.3.5)}$$

where ϵ_{ij} is the strain deviator tensor and again the numerical factor is introduced to ensure that the definition reduces correctly in uniaxial tension. Writing the flow rule of equ.3.3 in terms of the effective stress and strain leads to:

$$(3/2)(d\bar{e}^p)^2 = (2/3)\bar{\sigma}^2(d\lambda)^2$$

$$\Rightarrow d\lambda = (3/2)(d\bar{e}^p/\bar{\sigma}),$$

and the flow rule takes the form of the Prandtl-Reuss equations:

$$de^p_{ij} = (3/2)(d\bar{e}^p/\bar{\sigma})s_{ij} \qquad \text{(equ.3.6)}.$$

Since $d\bar{e}^p$ and $\bar{\sigma}$ reduce to de and σ in uniaxial tension, the axes in fig.3.1 may be interpreted as effective values and $d\bar{e}^p$ expressed as a function of $\bar{\sigma}$, or vice versa. The plastic strain components de^p_{ij} may then be calculated from equ.3.6. If the total strain components de_{ij} may be additatively decomposed into an elastic and a plastic part then:

$$de_{ij} = de^{el}_{ij} + de^p_{ij}$$

$$\Rightarrow de_{ij} = ds_{ij}/(2G) + \delta_{ij}d\sigma_{kk}/(9K) + (3/2)(d\bar{e}^p/\bar{\sigma})s_{ij}.$$

3.2. DILATING PLASTICITY AND POROUS MATERIALS.

A fundamental observation of classical mechanics is that plastic deformation takes place at approximately constant volume, a result which is inherent in classical constitutive theories such as the idealised case of a Von Mises material. However for materials containing voids the assumption of constant volume deformation requires qualification. While it is true that plastic deformation does not change the volume of the metal matrix, the growth of the voids in a triaxial stress field results in an increase in volume, a dilation, of the aggregate porous material. If the constitutive equations of such materials are formulated in terms of tractions and displacements of a continuous aggregate then the assumption of constant volume deformation no longer adequately reflects the behaviour of the material.

An associated observation is that the onset of yielding and the flow rate is independent of the hydrostatic component of the applied stress, depending solely on the deviatoric stresses. This is reflected in the pressure independence of the yield function and constitutive equations and in the prismatic nature of the yield surface in principal stress space. However in a porous material the presence of voids destroys locally the symmetry of a remote hydrostatic stress field and permits plastic flow under such conditions. This results in a pressure dependent yield function and constitutive equation.

3.3. POROUS CONTINUA.

The classical constitutive equations for non-porous materials regard matter as homogeneous and continuous over arbitrarily small

volumes and imply that physical quantities such as stress, which are meaningful for bulk material, are also meaningful on a microscopic scale. However the non-homogeneous nature of matter means that continuum models break down at sufficiently small volumes. At an atomic scale even single-phase, non-porous materials cannot be regarded as homogeneous continua, while porous materials are non-homogeneous at a much larger scale. In practice however, quantities defined by a limiting process to arbitrarily small volumes are normally used to determine the macroscopic behaviour of bulk material at a larger size scale. The concept of a porous continuum should then provoke no greater objection than that of any other continuum.

For a porous continuum, a matrix stress tensor σ_{ij} is defined as the remote load per unit area of the metal in the matrix. A corresponding aggregate stress tensor Z_{ij} is defined as the load per unit area of porous aggregate material. For isotropic materials both matrix and aggregate effective stresses may then be defined, eg:

$$\bar{\sigma}^2 = (1/2)((\sigma_1-\sigma_2)^2+(\sigma_2-\sigma_3)^2+(\sigma_3-\sigma_1)^2)$$

where the σ_i are now matrix principal stresses and the s_{ij} in the equivalent form of equ.3.2 are matrix stress deviators, and by:

$$\bar{Z}^2 = (1/2)((Z_1-Z_2)^2+(Z_2-Z_3)^2+(Z_3-Z_1)^2)$$

or equivalently:

$$\bar{Z}^2 = (3/2)S_{ij}S_{ij}$$

where the S_{ij} are aggregate stress deviators. Since the voids in a

porous aggegate cannot support any load then for the same remote loading the aggregate stress components and the aggregate effective stress will generally be less than the corresponding matrix stresses by an amount which will depend on the porosity.

3.4. A PRESSURE DEPENDENT YIELD FUNCTION.

The Von Mises yield surface of equ.3.3 may be written as:

$$\phi = (\bar{\sigma}/\sigma_y)^2 - 1 = 0$$

and the effect of porosity introduced through a pressure dependent term g to give:

$$\phi = (\bar{Z}/\bar{\sigma})^2 - g(Z_{kk},f) = 0 \qquad \text{(equ.3.7)}$$

where f is the current void volume fraction and Z_{kk} is the trace of the aggregate stress tensor, related to the mean or hydrostatic aggregate stress Z_m by:

$$Z_m = Z_{kk}/3.$$

For a material in which the matrix is incompressible, all of the dilation results from void growth and the pressure dependence of ϕ exactly matches the dilation rate (Rudnicki and Rice (1975)). In the light of upper bound analyses for spherically symmetric and cylindrically symmetric cells in a perfectly plastic material, Gurson (1977) proposed that:

$$g(Z_{kk},f) = (1 + f^2) - 2f \cosh(Z_{kk}/(2\bar{\sigma}))$$

which was modified by Tvergaard (1981) to:

$$g(Z_{kk},f) = (1 + q_3 f^2) - 2fq_1\cosh(q_2 Z_{kk}/(2\bar{\sigma}))$$

to give better agreement with a numerical solution for power-hardening materials. Here q_1 and q_2 are empirical constants while $q_3 = q_1^2$. The yield surface then becomes:

$$\phi = (\bar{Z}/\bar{\sigma})^2 + 2fq_1\cosh(q_2 Z_{kk}/(2\bar{\sigma})) - (1+q_3 f^2) \qquad \text{(equ.3.8)}.$$

Tvergaard (1981) found that:

$$q_1 = 1.5,\ q_2 = 1 \text{ and so } q_3 = 2.25$$

gave the best fit to the numerical solution and hence:

$$\phi = (\bar{Z}/\bar{\sigma})^2 + 3f\cosh(Z_{kk}/(2\bar{\sigma})) - (1+2.25f^2)$$

or equivalently:

$$\phi = (\bar{Z}/\bar{\sigma})^2 + 3f\cosh((3/2)(Z_m/\bar{\sigma})) - (1+2.25f^2)$$

These forms based on Tvergaard's (1981) results have been preferred in the numerical calculations performed in the current work, although setting f = 0 recovers the Von Mises yield surface of a non-porous material, for which $Z_{ij} = \sigma_{ij}$. The function g in the Gurson (1977) model or the variant due to Tvergaard (1981) produces a yield surface which closes gradually as shown in fig.3.2. In contrast the alternative model by Thomason (1981) shows no mean stress effect

until the limit load is reached for the intervoid ligament. This produces an end closure as shown in fig.3.2.

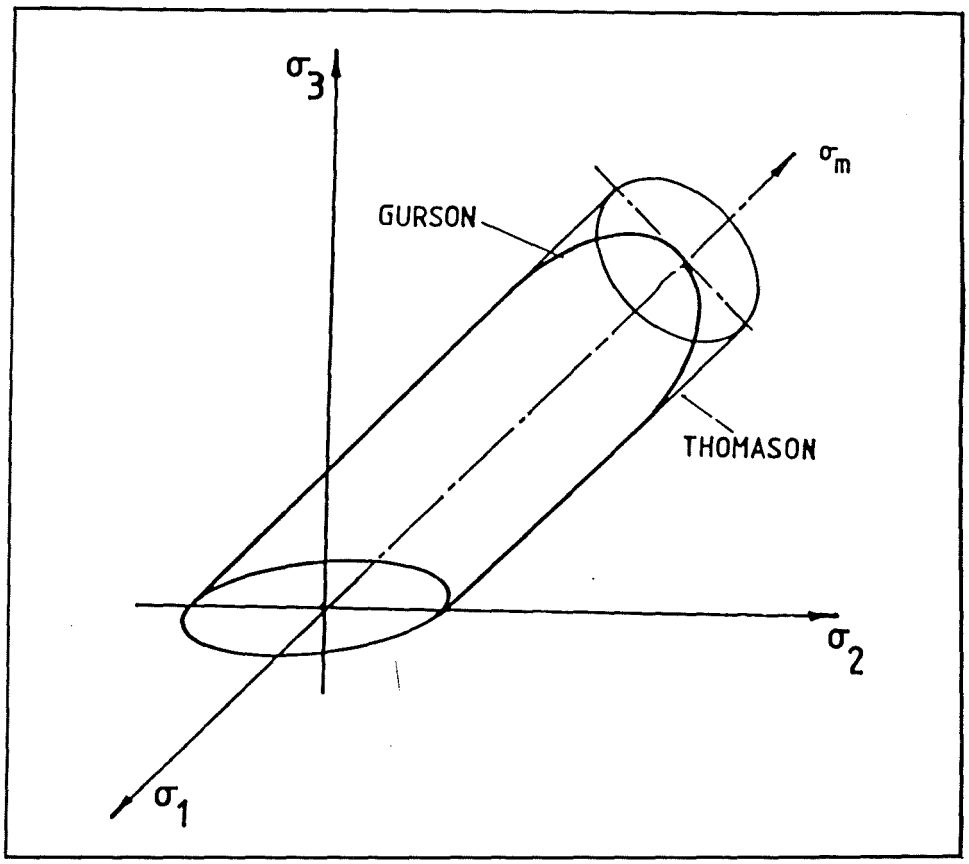

Fig.3.2. The pressure dependent yield surfaces of a dilating porous continuum.

3.5. AN APPROXIMATE YIELD FUNCTION.

Equation 3.8 cannot be solved analytically but an analytic approximation for $\bar{Z}$ may be made by a 2-term expansion of the cosh with $q_3 = q_1^2$ to give:

$$\phi = (\bar{Z}/\bar{\sigma})^2 + f q_1 (9/4) q_2 (Z_m/\bar{Z})^2 (\bar{Z}/\bar{\sigma})^2 - (1 - q_1 f)^2$$

As the deformation continues in a stress state with a tensile mean stress, the voids grow and the porosity f increases. In general the aggregate stress tensor Z_{ij} will be progressively reduced relative to the matrix stress σ_{ij}. However a comparative analysis of specimens with similar shapes was performed by Brown, Hancock, Thomson and Parks (1980) using both the constitutive equations of classical plasticity and dilating constitutive laws based on Gurson's (1977) yield surface. This analysis noted the stress relieving influence of void growth in the porous aggregate but found that while both $\bar{Z}$ and Z_m were reduced relative to the corresponding matrix quantities, this was such that the aggregate triaxiality $Z_m/\bar{Z}$ was relatively insensitive to increasing deformation. It is then often reasonable to write:

$$Z_m/\bar{Z} = \sigma_m/\bar{\sigma}$$

in which case the yield function becomes:

$$\phi = (\bar{Z}/\bar{\sigma})^2+fq_1(9/4)q_2(\sigma_m/\bar{\sigma})^2(\bar{Z}/\bar{\sigma})^2-(1-q_1 f)^2$$

For yielding, ϕ is zero and normalising with respect to σ_0 gives:

$$(\bar{Z}/\sigma_0)^2 = (\bar{\sigma}/\sigma_0)^2(1-(3/2)f)^2/(1+f(27/16)(\sigma_m/\bar{\sigma})^2)$$

where the q_i have the values due to to Tvergaard (1981). Gurson's (1977) original formulation of the dilating yield surface may be recovered by setting q_i= 1 to give the approximate yield surface:

$$(\bar{Z}/\sigma_0)^2 = (\bar{\sigma}/\sigma_0)^2(1-f)^2/(1+f(9/4)(\sigma_m/\bar{\sigma})^2)$$

3.6. A FLOW RULE FOR DILATING MATERIALS.

3.6.1. THE BASIC FLOW RULE.

Because of the large geometry changes which accompany gross plastic deformation, constitutive laws are best formulated in terms of deformation differentials, which may be implied by the use of velocities v_i rather than displacements u_i. The plastic constitutive equations then take the form of a flow rule in rate form. An appropriate measure of deformation is the rate-of-deformation tensor D_{ij} given in rectangular Cartesian coordinates by:

$$D_{ij} = (1/2)(v_{i,j} + v_{j,i}).$$

in which the commas denote material derivatives, taken from the viewpoint of an observer riding on a particle of material. In general, covariant derivatives should be taken but in rectangular Cartesian coordinates these reduce to ordinary derivatives. It is a matter of convenience whether a Lagrangian or Eulerian formulation is used and here derivatives are expressed in Eulerian form with respect to the current spatial coordinates x_i of the particle.

Again assuming that each deformation increment may be additatively decomposed into an elastic and a plastic component then:

$$D_{ij} = D^{el}{}_{ij} + D^{p}{}_{ij}$$

For the isotropic polycrystalline materials of interest here, the normality of the matrix deformation implies normality of the aggregate

deformation (Bishop and Hill (1951)) and hence the existence of an associated flow rule for the dilating yield surface of equ.3.8, which may be written:

$$\phi(Z_{ij},\bar{\sigma},f) = 0$$

This yield function may then be regarded as a plastic potential and the plastic strain increments determined from:

$$D^{p}_{ij} = \Lambda(\partial\phi/\partial Z_{ij}) \qquad \text{(equ.3.9)}$$

where Z_{ij} is the Cauchy or true stress of the porous aggregate and Λ is a Lagrange multiplier to be determined.

3.6.2. THE CONSISTENCY CONDITION.

To evaluate Λ and allow the D^{p}_{ij} to be calculated, use is made of the consistency condition, which recognises that during loading the flow stress must satisfy the yield function at all times, ie:

$$\dot{\phi}(Z_{ij},\bar{\sigma},f) = 0.$$

where the overdot indicates some time rate. Applying the chain rule:

$$(\partial\phi/\partial Z_{ij})\dot{Z}_{ij} + (\partial\phi/\partial\bar{\sigma})\dot{\bar{\sigma}} + (\partial\phi/\partial f)\dot{f} = 0$$

For large deformations it is most appropriate to choose a corotational time rate of the tensor components, since this is invariant under ro-

tation of the axes. Such a corotational time rate is the Jaumann rate and denoting this by ^{0} then:

$$(\partial\phi/\partial Z_{ij})\overset{0}{Z}_{ij} + (\partial\phi/\partial\bar{\sigma})\dot{\bar{\sigma}} + (\partial\phi/\partial f)\dot{f} = 0$$

The time rates are evaluated by considering the role of plastic work dissipation, of void nucleation and growth, and the elastic constitutive equation.

3.6.3. PLASTIC WORK DISSIPATION.

An aggregate volume V with porosity f contains a volume v of matrix:

$$v = (1-f)V$$

and since voids have no means of dissipating energy through internal work then all of the plastic work done in deforming a porous aggregate must be dissipated in the matrix. If W and w denote power dissipation per unit volume in the aggregate and matrix respectively, then:

$$WV = wv$$

and hence:

$$\Rightarrow \dot{W} = \dot{w}(1-f) \qquad \text{(equ.3.10)}.$$

The dissipation in the aggregate is:

$$\dot{W} = Z_{ij}D^{p}_{ij} \qquad \text{(equ.3.11)}$$

and the dissipation in the matrix could similarly be defined as:

$$w = \sigma_{ij} e^{p}_{ij}.$$

However since the matrix is incompressible, only shear terms contribute to the dissipation and for the matrix this reduces to:

$$\dot{w} = \bar{\sigma}\dot{\bar{e}}^{p} \qquad \text{(equ.3.12)}$$

Here the rate of equivalent plastic strain is given by:

$$\dot{\bar{e}}^{p} = d\bar{e}^{p}/dt$$

in which $d\bar{e}^{p}$ is the matrix effective plastic strain increment defined by equ.3.5 with the ϵ_{ij} interpreted as matrix quantities. Substituting equ.3.11 and 3.12 into equ.3.10 gives:

$$Z_{ij} D^{p}_{ij} = \bar{\sigma}\dot{\bar{e}}^{p}(1-f) \qquad \text{(equ.3.13).}$$

The tangent modulus of the matrix is defined as:

$$h = d\bar{\sigma}/d\bar{e}^{p}$$

and by the chain rule:

$$h = (d\bar{\sigma}/dt)(dt/d\bar{e}^{p})$$

$$\Rightarrow \dot{\bar{\sigma}} = h\dot{\bar{e}}^{p}.$$

Substituting for $\dot{\bar{e}}^p$ from equ.3.13 then leads to:

$$\dot{\bar{\sigma}} = hZ_{ij}D^p{}_{ij}/(\bar{\sigma}(1-f))$$

and with the flow rule in the form of equ.3.9, then:

$$\Rightarrow \dot{\bar{\sigma}} = hZ_{ij}\,\Lambda(\partial\emptyset/\partial Z_{ij})/(\bar{\sigma}(1-f)) \quad \text{(equ.3.14)}.$$

3.6.4. MATRIX PROPERTIES.

In order to represent strain hardening of the matrix, the matrix flow stress $\bar{\sigma}$ can be updated from the aggregate properties through the dissipation relationship (equ.3.13) in the form:

$$Z_{ij}d\bar{E}^p{}_{ij} = (1-f)\bar{\sigma}d\bar{e}^p$$

which expresses the idea that the work done by the external stresses is dissipated by incompressible plastic flow in the matrix. The matrix strain $\bar{e}^p$ is a convenient measure of deformation, with the corresponding flow stress σ determined from a uniaxial tensile test. Strictly speaking, the results of such a test relate to an aggregate material which, after necking, undergoes non-homogeneous deformation. However necking restricts plastic deformation, and hence void growth and dilation, to a small volume of the specimen within the neck. The remainder may then be considered to behave as non-porous aggregate or matrix. By analogy with the definition of

the matrix effective strain in equ.3.5, an aggregate effective strain may be defined as:

$$\bar{E}^p = \int d\bar{E}^p$$

where:

$$(d\bar{E}^p)^2 = (2/3)dF^p{}_{ij}dF^p{}_{ij}$$

and F denotes the aggegate strain deviators. While the expressions for $\bar{Z}$ and $\bar{E}^p$ reduce to $\bar{\sigma}$ and $\bar{e}^p$ for a non-porous aggregate, the relation between these is dependent on the stress state and in perfect hydrostatic tension deformation can occur in a porous material with identically zero values of $\bar{Z}$ and $\bar{E}^p$. In consequence $\bar{e}^p$ is the preferred measure of deformation.

3.6.5. VOID NUCLEATION AND GROWTH.

The increase in porosity f contains a contribution from void nucleation in addition to the contribution from void growth. Writing:

$$\dot{f} = \dot{f}_{nuc} + \dot{f}_{growth}$$

the consistency condition becomes:

$$(\partial\phi/\partial Z_{ij})\overset{0}{Z}_{ij} + (\partial\phi/\partial\bar{\sigma})\dot{\bar{\sigma}} + (\partial\phi/\partial f)(\dot{f}_{growth}+\dot{f}_{nuc}) = 0 \qquad \text{(equ.3.15).}$$

If it is assumed that nucleation begins at a fixed value of $\bar{e}^p$ and continues at a uniform rate with plastic strain until nucleation is completed, at another fixed value of $\bar{e}^p$ such that:

$$\dot{f}_{nuc} = C_1 \dot{\bar{e}}^p \qquad \text{(equ.3.16).}$$

then substituting for $\dot{\bar{e}}^p$ from equ.3.13, with the flow rule of equ.3.9, gives:

$$\dot{f}_{nuc} = C_1 Z_{ij} \Lambda(\partial\phi/\partial Z_{ij})/(\bar{\sigma}(1-f)) \qquad \text{(equ.3.17).}$$

Alternatively, Needleman and Rice (1978), have suggested that:

$$\dot{f}_{nuc} = F_1 \dot{\bar{Z}} + F_2 \dot{Z}_m \qquad \text{(equ.3.18)}$$

in which the first term depends on the flow stress and hence on the effective plastic strain while the second term depends on the hydrostatic component of the stress state. If either of these factors is assumed to have negligible influence on void nucleation then F_1 or F_2 in equ.3.18 may be set to zero.

If v_{voids} is the total volume of voids in a volume V of aggregate then the current volume fraction is:

$$f = v_{voids}/V$$

Ignoring the influence of nucleation for the present and denoting the volume of matrix in V by v gives:

$$V = v + fV$$

$$\Rightarrow df = (1-f)(dV/V)$$

$$\Rightarrow df = (1-f)dE_{kk}$$

where E_{kk} is the volumetric strain to a first order approximation. The rate of change of porosity due to void growth is:

$$\dot{f}_{growth} = df/dt = (1-f)(dE_{kk}/dt).$$

If the contribution of elastic dilation is small then:

$$\dot{f}_{growth} = (1-f)D^{p}_{kk}$$

The flow rule in the form of equ.3.9 thus gives:

$$\dot{f}_{growth} = (1-f)\Lambda(\partial\phi/\partial Z_{kk}) \qquad \text{(equ.3.19)}.$$

3.6.6. THE ELASTIC CONSTITUTIVE LAW.

For aggregate materials such as structural steels, the elastic component D^{el}_{ij} of the total deformation increment D_{ij} can be related to an aggregate stress rate through a linear elastic constitutive equation such as:

$$\dot{Z}_{ij} = C_{ijkl}D^{el}_{kl}$$

The values of the elastic constants C_{ijkl} depend on the particular

stress rate chosen and for the Jaumann stress rate this becomes:

$$\overset{0}{Z}_{ij} = C_{ijkl} D^{el}_{kl}$$

No primitive

where the C_{ijkl} are now specific to the chosen stress rate. With the flow rule of equ.3.9:

$$\Rightarrow \overset{0}{Z}_{ij} = C_{ijkl}(D_{kl} - \Lambda(\partial \emptyset / \partial Z_{kl})) \qquad \text{(equ.3.20).}$$

For isotropic aggregates, this may be written in terms of the 2 arbitrarily chosen independent elastic constants as:

$$\overset{0}{Z}_{ij} = 2GD^{el}_{ij} + \delta_{ij}(K-(2/3)G)D^{el}_{kk}$$

or, if the stresses are known, by the inverse relation:

$$D^{el}{}_{ij} = \overset{0}{S}_{ij}/(2G) + \delta_{ij}\overset{0}{Z}_{kk}/(9K).$$

3.6.7. THE DETERMINATION OF Λ.

The most useful expression for Λ will depend in part on what is already known. For example, with displacement loading, the rate of total deformation D_{ij} is specified at the current level of Z_{ij} and the problem is to determine $D^{p}{}_{ij}$ and hence $D^{el}{}_{ij}$ and Z_{ij}. Substituting for Z_{ij} from equ.3.20, $\dot{f}$ from equ.3.16 and equ.3.19 and $\dot{\sigma}$ from equ.3.14 into the consistency condition of equ.3.15 would then give:

$$(\partial\phi/\partial Z_{ij})C_{ijkl}(D_{kl} - \Lambda(\partial\phi/\partial Z_{kl})$$
$$= (\partial\phi/\partial\bar{\sigma})hZ_{ij}\ \Lambda(\partial\phi/\partial Z_{ij})/(\bar{\sigma}(1-f))$$
$$+ (\partial\phi/\partial f)(1-f)\Lambda(\partial\phi/\partial Z_{kk})$$
$$+ (\partial\phi/\partial f)C_1 Z_{ij}\ \Lambda(\partial\phi/\partial Z_{ij})/(\bar{\sigma}(1-f))$$

=>

$$(\partial\phi/\partial Z_{ij})C_{ijkl}D_{kl} =$$
$$\Lambda\ ((\partial\phi/\partial Z_{ij})C_{ijkl}(\partial\phi/\partial Z'_{kl})$$
$$- (\partial\phi/\partial\bar{\sigma})(hZ_{ij})/(\bar{\sigma}(1-f))(\partial\phi/\partial Z_{ij})$$
$$- (\partial\phi/\partial f)(1-f)(\partial\phi/\partial Z_{kk})$$
$$- (\partial\phi/\partial f)C_1 Z_{ij}(\partial\phi/\partial Z_{ij})/(\bar{\sigma}(1-f))$$

=>

$$\Lambda = (\partial\phi/\partial Z_{ij})C_{ijkl}D_{kl}\ /$$
$$((\partial\phi/\partial Z_{pq})C_{pqrs}(\partial\phi/\partial Z_{rs})$$
$$- (\partial\phi/\partial\bar{\sigma})hZ_{pq}(\partial\phi/\partial Z_{pq})/(\bar{\sigma}(1-f))$$
$$- (\partial\phi/\partial f)(1-f)(\partial\phi/\partial Z_{mm})$$
$$- (\partial\phi/\partial f)C_1 Z_{pq}(\partial\phi/\partial Z_{pq})/(\bar{\sigma}(1-f))$$

(equ.3.21).

The derivatives may be obtained from the yield function chosen, the C_{ijkl} are derivable by experiment while a uniaxial tensile test will

give h and $\bar{\sigma}$ as functions of deformation for a specific material. The current value of f may be obtained by incremental updating from an initial value f_0. Substituting for Λ into the basic flow rule of equ.3.9 then gives the D^p_{ij}. On a similar basis, Yamamoto (1978) gives an expression for Λ in the absence of nucleation while Aoki, Kishimoto, Takeya and Sakata (1984) consider the case of nucleation by the Needleman and Rice (1978) formula of equ.3.18. More recently, Aravas and McMeeking (1984) have recognised the statistical nature of nucleation by using the strain controlled relation of equ. 3.16 with a statistical function for C_1.

PART 2: THE STRESS AND STRAIN FIELDS NEAR A SPHERICAL INCLUSION IN A DEFORMING MATRIX.

4. NUMERICAL ANALYSES.

4.1. THE FINITE ELEMENT PROGRAM.

Continuum analysis is appropriately applied over size scales which are large compared to the dislocation spacing and in the present work, a continuum approach has been adopted in which the problem of a spherical inclusion in hardening and non-hardening matrices subject to large remote plastic strains has been analysed using a finite element program based on the partial stiffness approach of Marcal and King (1967) as modified by Rice and Tracey (1973). Appendix A.1.1 explains the essential features of the program which has a finite strain capability based on the analysis of McMeeking and Rice (1975). The stress and strain fields are determined incrementally using the variational principle of Nagtegaal, Parks and Rice (1974) to apply a uniform dilation over a mesh of isoparametric quadrilateral elements. Classical non-dilating plastic constitutive relations were used for the inclusion analyses although it is possible to specify plastically dilating elements which behave according to the constitutive laws associated with Gurson's (1977) yield surface and so model the effect of increasing porosity in the aggregate material. The elements may be either linear-elastic/ perfectly-plastic, linear-elastic/power-hardening or piecewise-linear and the program allows both axisymmetric and plane strain solutions to be obtained.

4.2. THE POST-PROCESSOR.

The existing solutions for the inclusion problem have noted the importance of the maximum radial stress on the interface, while void nucleation theories emphasise the role of the maximum interfacial radial stress and of the local strain concentration at the inclusion interface. The former may be calculated by first determining the normal to the interface at the centroid of each interfacial element. Application of the coordinate transformation equations to the components of the local stress tensor relative to the global (x-y) axes, as determined by the finite element analysis, then gives the normal (ie radial) and tangential stresses at the interface. Such calculations must be repeated at each element around the interface and are most conveniently performed by a post-processor drawing directly on the output files from the finite element program. Such a program was written (appendix A.1.2) to calculate these and other significant quantities and to produce graphical output (GINO Manual).

4.3. THE ANALYSIS OF A SPHERICAL INCLUSION.

Considering the inclusion to be spherically symmetric, only the first quadrant of the cross-section of the axisymmetric problem need be modelled as in fig.4.1 with the origin of the coordinate system at the centre of the inclusion. The finite element mesh was generated automatically using a procedure developed by Zienkiewicz and Phillips (1971) and comprises 160 quadrilateral elements bounded by generators extending radially from the origin and by concentric rings. The origin is common to 2 nodes of each of the 10 quadrilateral elements in the smallest ring, which therefore appear as triangles. The

element size was progressively increased towards the remote boundary where stress and strain gradients become less severe. The inclusion comprises the 50 elements in the 5 innermost rings with the remaining elements representing the matrix. This gives a remote boundary at approximately 6 times the inclusion radius. Symmetry implies that nodes on the y-axis be constrained such that no displacement occurs in the x-direction and nodes on the x-axis be constrained such that no displacement occurs in the y-direction.

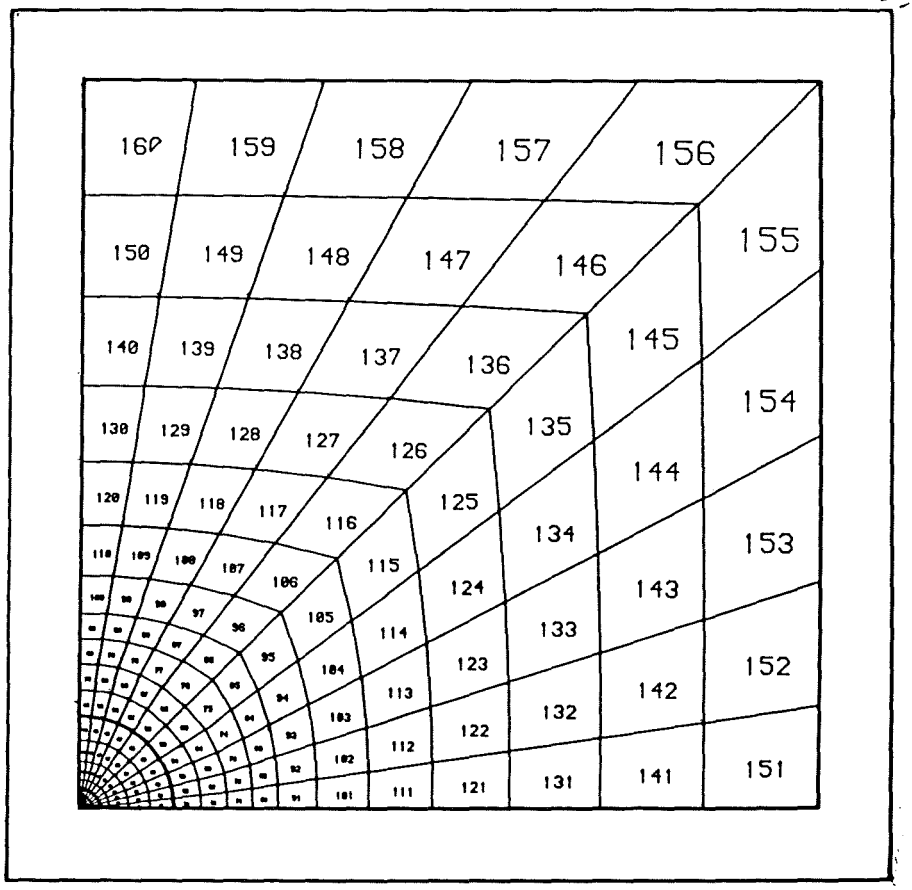

Fig.4.1. The finite element mesh used to model an inclusion in an elastic/plastic matrix. The inclusion is bounded by the heavy arc.

The conditions at the interface between an inclusion and the surrounding matrix will depend on the properties of the inclusion relative to the those of the matrix, in particular on their relative stiffnesses. At one extreme the inclusion may be considered to have

zero stiffness and is in effect a void while the other extreme is the case of a rigid inclusion: real materials lie somewhere in between. The interesting case of equal matrix and inclusion stiffnesses will be considered in some detail. In real materials the matrix will be both elastic and subject to work or strain hardening while any second phase particles will be elastic at first but will subsequently fracture in a brittle manner or deform plastically. However, it is not practicable to completely describe the behaviour of such real materials in finite element terms without some simplification of inclusion and matrix responses. This simplification may take the form of allowing only elastic deformation of the inclusion or indeed of considering the inclusion to be rigid. A rigid inclusion was simulated by constraining the nodes along the inclusion-matrix interface to have no displacement in either the x or y directions. Equilibrium and compatibility are then satisfied through the prescribed interfacial boundary conditions rather than through the adjacent elements on either side of the interface. Such a model therefore allows analysis of the matrix flow field but gives identically zero stress and strain fields within the inclusion and cannot provide information about its interior or of any internal stress and strain gradients. In addition, the severe constraint on the interface prevents elastic deformation of the inclusion which would in practice allow some relaxation of the matrix stress field.

A number of solutions were obtained for different combinations of inclusion and matrix response. As a precursor to the specific case of strongly hardening Swedish Iron in which the elastic modulus of the inclusions is of the same order as that of the matrix, the general features of the stress and strain fields associated with rigid inclusions are discussed. It is initially instructive to con-

sider a rigid inclusion in a rigid/perfectly-plastic matrix. This cannot be modelled exactly using the available finite element program but the response of such a material is approximated by considering the matrix to have a high but finite elastic modulus. The effect of the elasticity of the matrix may be illustrated by a similar analysis of a rigid inclusion in an elastic/perfectly plastic matrix with an elastic modulus typical of structural steels. The role of matrix strain hardening may then be inferred from an analysis of a rigid inclusion in an elastic/power-hardening matrix. These solutions are presented in the following sections, the most general case being discussed first. In this, a power law stress-strain curve of the form:

$$(\bar{\sigma}/\sigma_0)^{(1/n)}-(\bar{\sigma}/\sigma_0) = (\bar{e}^p/e_0) \quad \text{(equ.4.1)}$$

was used for the matrix although such a simple expression has a limited ability to describe the stress-strain relationship of real materials. This limitation is felt in the analysis of hardening materials at large plastic strains where it is important that the curvature of the stress-strain curve for the material be correctly modelled through an appropriately chosen power hardening index n. If the initial yield stress σ_0 is determined by experiment then the choice of n fixes the value of the remaining parameters in equ.4.1, in particular that of the constant e_0, normally the initial yield strain. The 'elastic modulus' defined by:

$$E = \sigma_0/e_0$$

then bears no relation to the true elastic modulus of the material and together with e_0 must simply be regarded as a curve fitting parameter with no direct physical meaning. It is then implicit that the

elastic response of the material is of no significance at large plastic strains. Conversely, if the response at plastic strains of the order of the elastic strains is to be determined, it is essential that elastic constants assume their true values for the material. An experimentally determined initial yield stress σ_0 and elastic modulus E will fix the initial yield strain e_0. The 'power hardening index' n in equ.4.1 is then a curve fitting parameter which need not exactly represent the long range curvature of the stress-strain law. In physical terms, such an approach implies that the analysis becomes less reliable at increasing plastic strains.

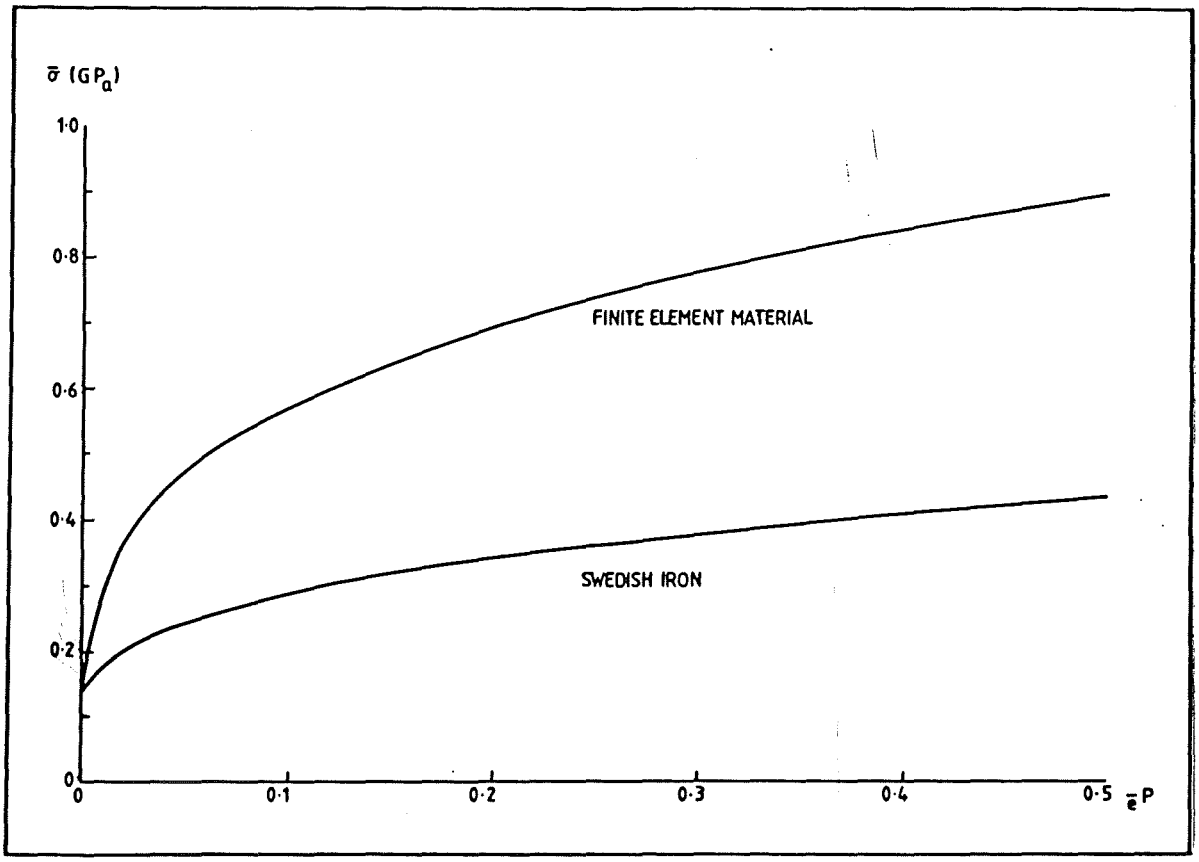

Fig.4.2. The stress-strain characteristics of the material used for the finite element analysis. For comparison, the lower curve gives the corresponding relation for Swedish Iron.

An elastic modulus 210.0 GPa and an initial yield stress of 0.14 GPa were chosen in the present work with a power hardening index n of 0.28 to give a constitutive response (fig.4.2) representative of low yield, strongly strain hardening materials. In cases where it is necessary to model a specific material throughout both the elastic and plastic range, a piecewise linear relation is more appropriate.

5. RESULTS.

5.1. A RIGID INCLUSION IN AN ELASTIC, POWER-HARDENING MATRIX.

The finite element model was subjected to 53 increments of displacement controlled uniaxial tensile loading along the remote boundary parallel to the x-axis, reaching a final remote plastic strain of approximately 15% or 220 times the initial yield strain. The results typically showed the greatest stresses and strains in elements near the interface while contour plots of field variables such as the local flow stress $\bar{\sigma}$ (fig.5.1) and the effective plastic strain $\bar{e}^p$ showed very small stress and strain gradients in the remote boundary elements. Significant gradients only developed near the inclusion-matrix interface (fig.5.2) which justified the representation of an isolated inclusion in an infinite matrix by a remote boundary at 6 times the inclusion radius.

Contour plots such as fig.5.1 and fig.5.2 can give a useful appreciation of the variation of quantities throughout the field of the analysis but some care is required in interpreting the region near the inclusion-matrix interface. Since the finite element solution gives values for field variables only at the centroids of the elements then contouring routines which interpolate between these centroidal values will attempt to draw contours within the inclusion itself, although the interfacial prescribed boundary conditions imply that field variables will be identically zero within the interface. A finer mesh near the interface would reduce the spread of contours here but the difficulty exists in principle for any grade of mesh.

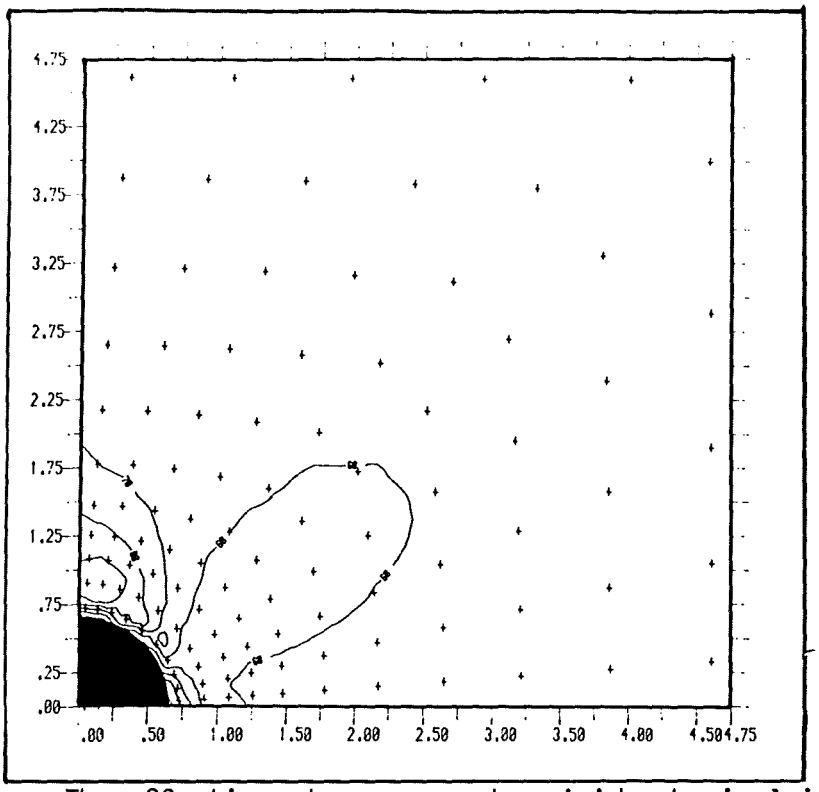

Fig.5.1. The effective stress around a rigid spherical inclusion in an elastic/power-hardening-plastic matrix subject to a remote uniaxial tensile load. $\bar{\sigma} = 0.6\sigma_0$ on contour 60.

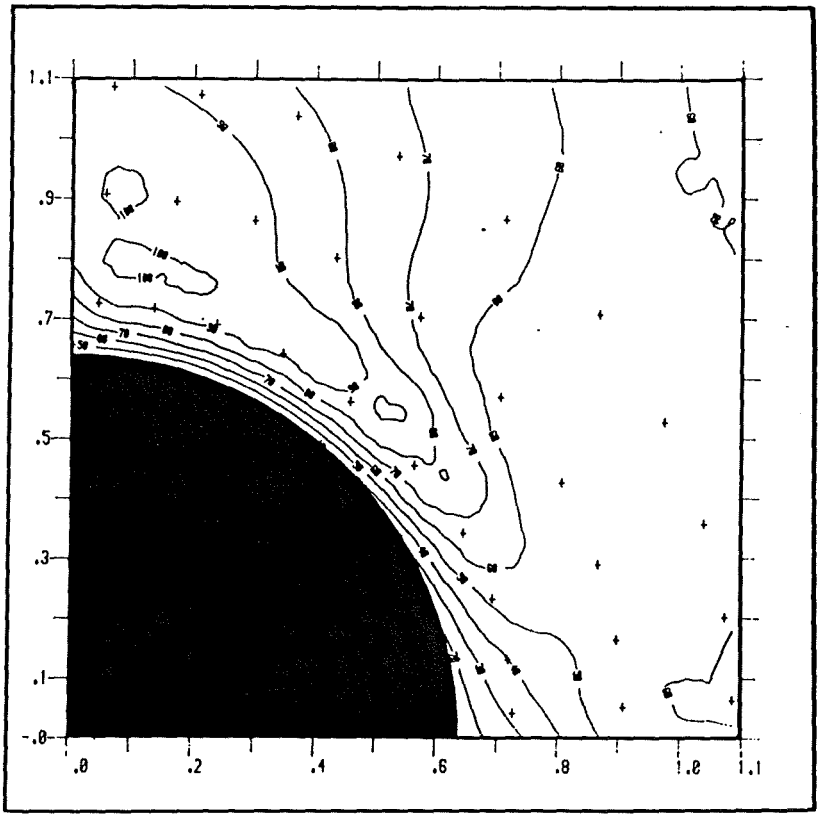

Fig.5.2. The effective stress near the interface of a rigid spherical inclusion in an elastic/power-hardening matrix subject to a remote uniaxial tensile load. $\bar{\sigma} = 0.9\sigma_0$ on contour 90.

Yielding first occurred at the pole of the inclusion at a small distance from the interface, in element 70, rather than at the inclusion itself (fig.5.3). The resulting plastic zone spread with each increment of remotely applied load but the polar interfacial element, element 60, did not yield until some time after its neighbours. This plastic zone extended to leave an elastic lobe at about 60^0 to the loading direction before full plasticity was finally reached. No large plastic strain concentrations were found on the interface while at large remote plastic strains the maximum plastic strain over the whole field was found to occur above the pole of the inclusion, a small distance from the interface, in element 80.

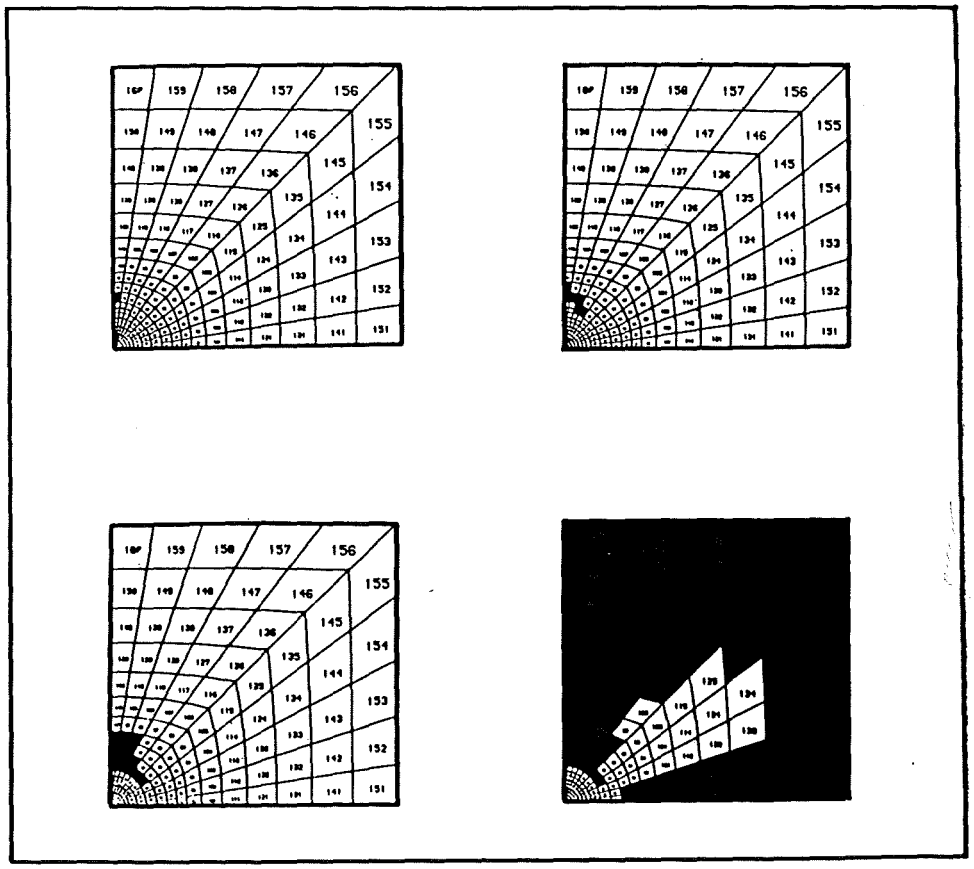

Fig.5.3. The development of the plastic zone, shown in solid black, around a rigid spherical inclusion in an elastic/power-hardening plastic matrix subject to a remote uniaxial tensile load.

The maximum plastic strain on the interface developed at approximately $\pi/4$ to the loading direction in elements 55 and 56, as shown by the contours in fig.5.4 and remained there throughout the loading history.

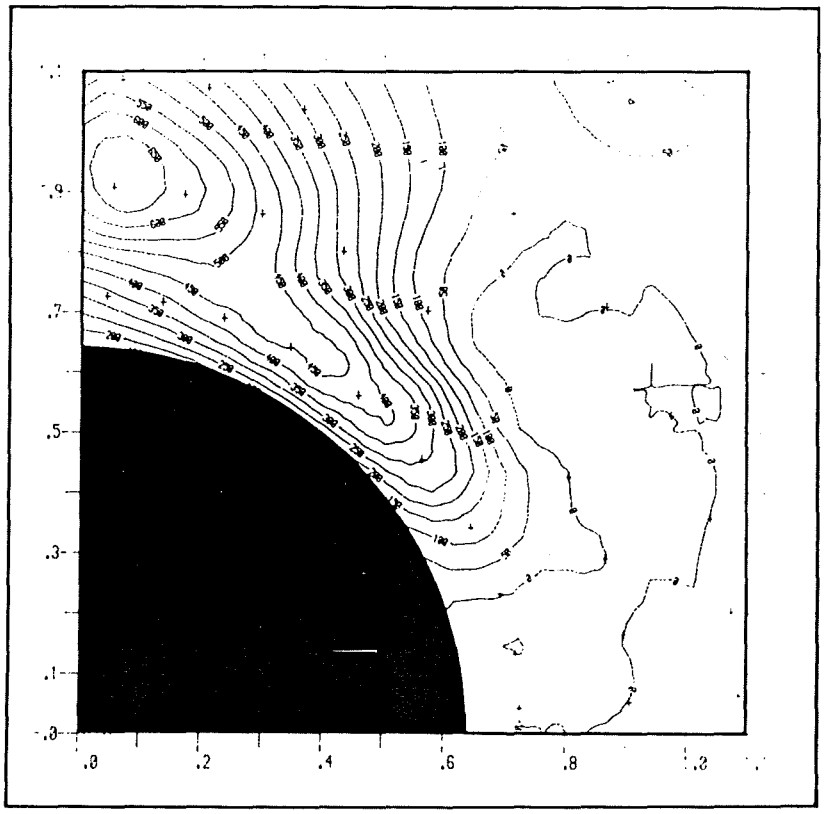

Fig.5.4. The effective plastic strain near a rigid spherical inclusion in an elastic/power-hardening plastic matrix subject to remote uniaxial tension. $\bar{e}^p = 0.5e_0$ on contour 500.

Figure 5.5 compares the effective plastic strain concentration ($\bar{e}^p/\bar{e}^p_\infty$) in a number of significant elements. Since the remote elements were initially elastic, ordinates are plotted against the total remote strain component e_{yy} in the loading direction, normalised with respect to the initial yield strain e_0 in uniaxial tension. From fig.5.5 it is apparent that the plastic strain becomes progressively smaller as the pole of the inclusion is approached

through elements 80, 70 and 60 directly above it. These moderate strain concentrations became almost constant at large remote plastic strains, tending, for example, to approximately 1.1 times e_0 in element 56 at approximately $\pi/4$ to the loading direction and to 0.8 in the polar element, element 60. The maximum interfacial effective stress must coincide with the maximum interfacial effective plastic strain at approximately $\pi/4$ to the loading direction.

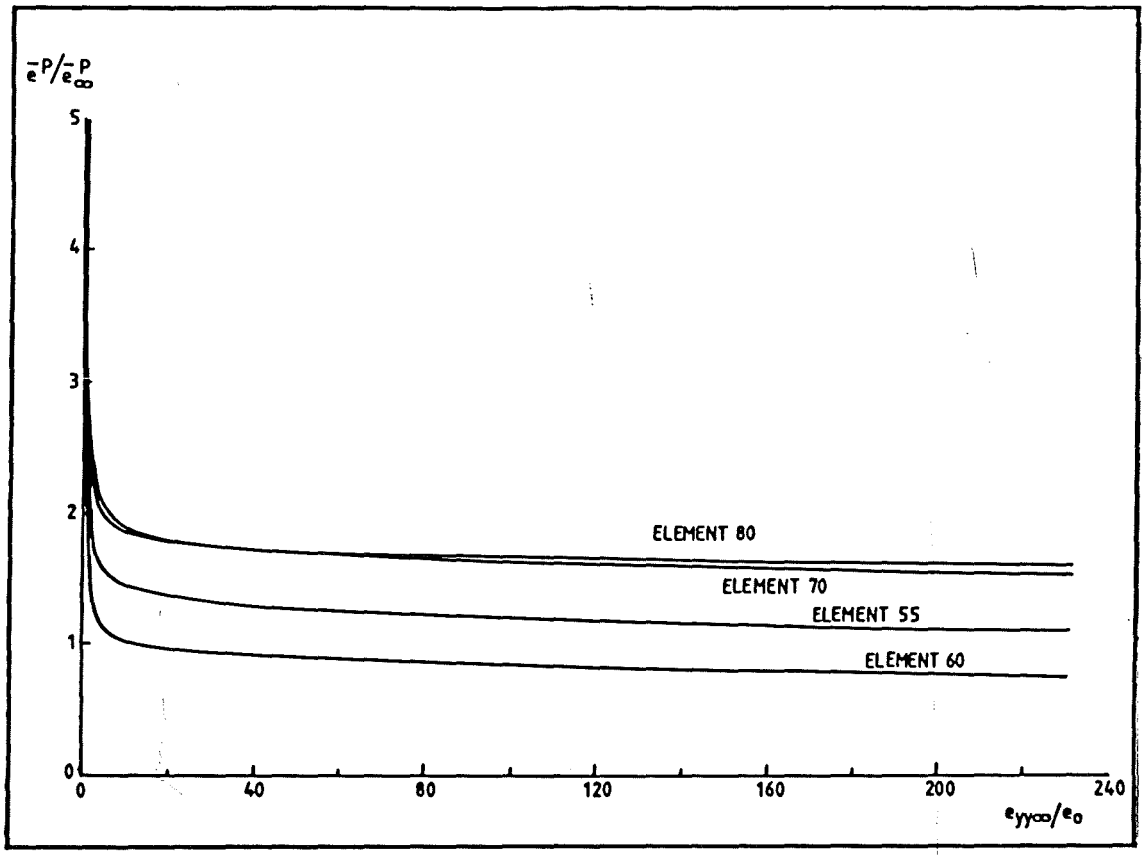

Fig.5.5. The effective plastic strain concentration in significant elements near a rigid spherical inclusion in an elastic/power-hardening-plastic matrix subject to remote uniaxial tension.

In contrast, the maximum interfacial normal or radial stress σ_{rrmax}, calculated by transforming the stress components, was

found to develop initially at the pole of the inclusion (element 60) as shown in fig.5.6.

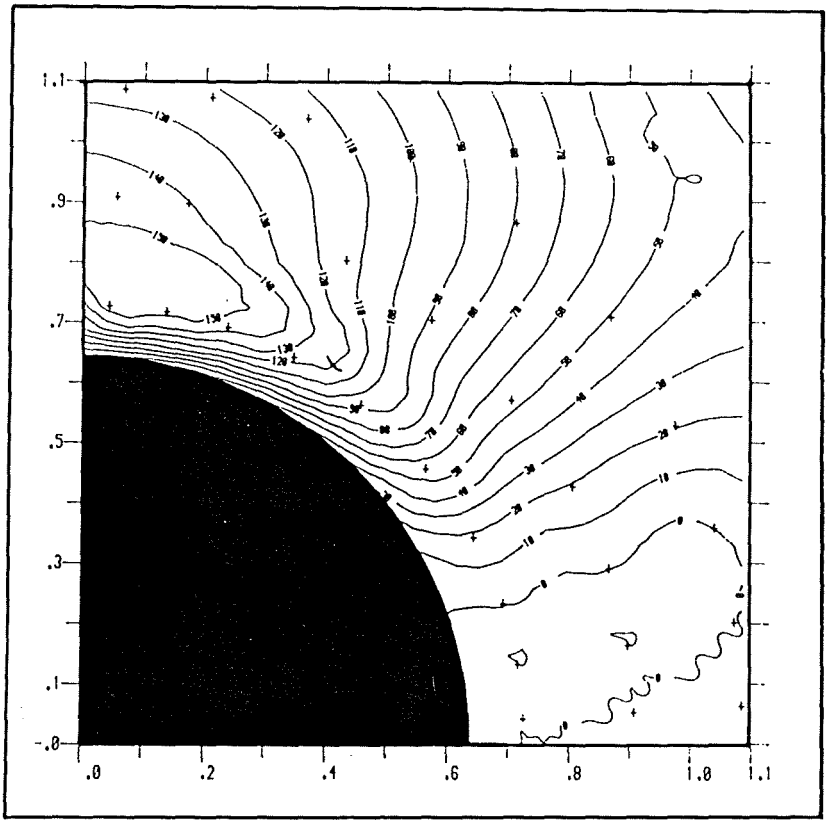

Fig.5.6. The interfacial radial stress around a rigid spherical inclusion in an elastic/power-hardening matrix for small remote uniaxial tensile strains. $\sigma_{rr} = 0.9\sigma_0$ on contour 90.

As the deformation continued, the greatest interfacial radial stress moved away from the pole to the adjacent element (element 59) as shown in fig.5.7. This feature is also shown in the work of Orr and Brown (1974) and of Argon, Im and Safoglu (1975) although the difference in the radial stress at the two locations is small for small remote deformations.

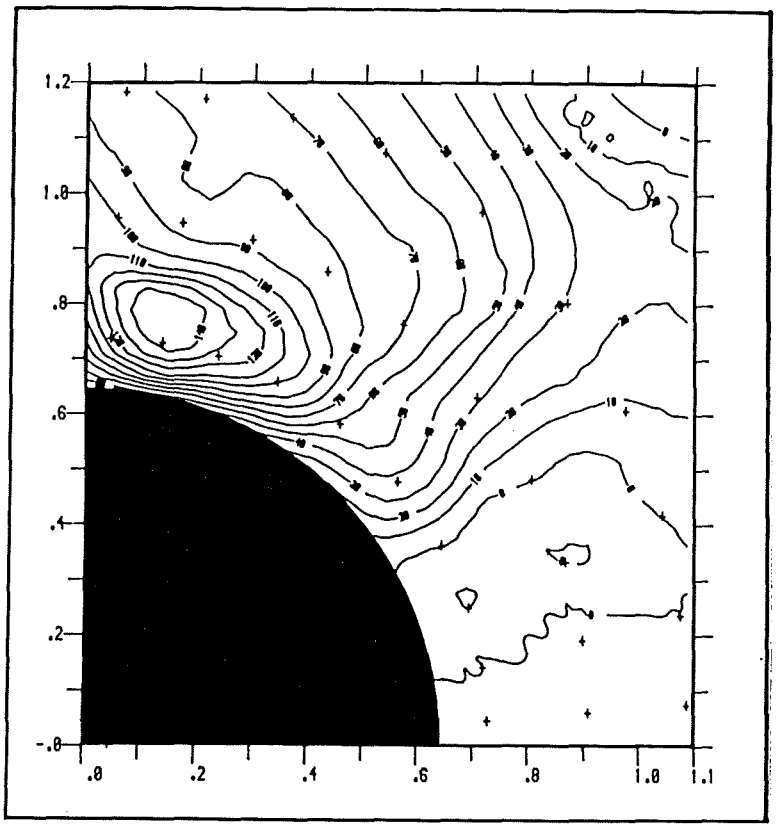

Fig.5.7. The interfacial radial stress around a rigid spherical inclusion in an elastic/power-hardening matrix for large remote uniaxial tensile strains. $\sigma_{rr} = 9.0\sigma_0$ on contour 90.

Figure 5.8 shows the maximum radial interfacial stress σ_{rrmax} for element 59 normalised with respect to the remote flow stress. For strain hardening materials, the mean stress continued to rise with increasing deformation but following the observation of Argon, Im and Safoglu (1975) on the results of Orr and Brown (1974), the maximum interfacial radial stress was assumed to be of the form

$$\sigma_{rrmax} = C\bar{\sigma}_{\infty} + \sigma_{m\infty}$$

in which the appropriate remote mean stress $\sigma_{m\infty}$ is simply superimposed on the local interfacial stress field resulting from a purely

deviatoric remote stress state of magnitude $\bar{\sigma}_\infty$. C may be considered either as the maximum interfacial radial stress concentration factor or as the normalised maximum interfacial radial stress in a purely deviatoric remote stress field.

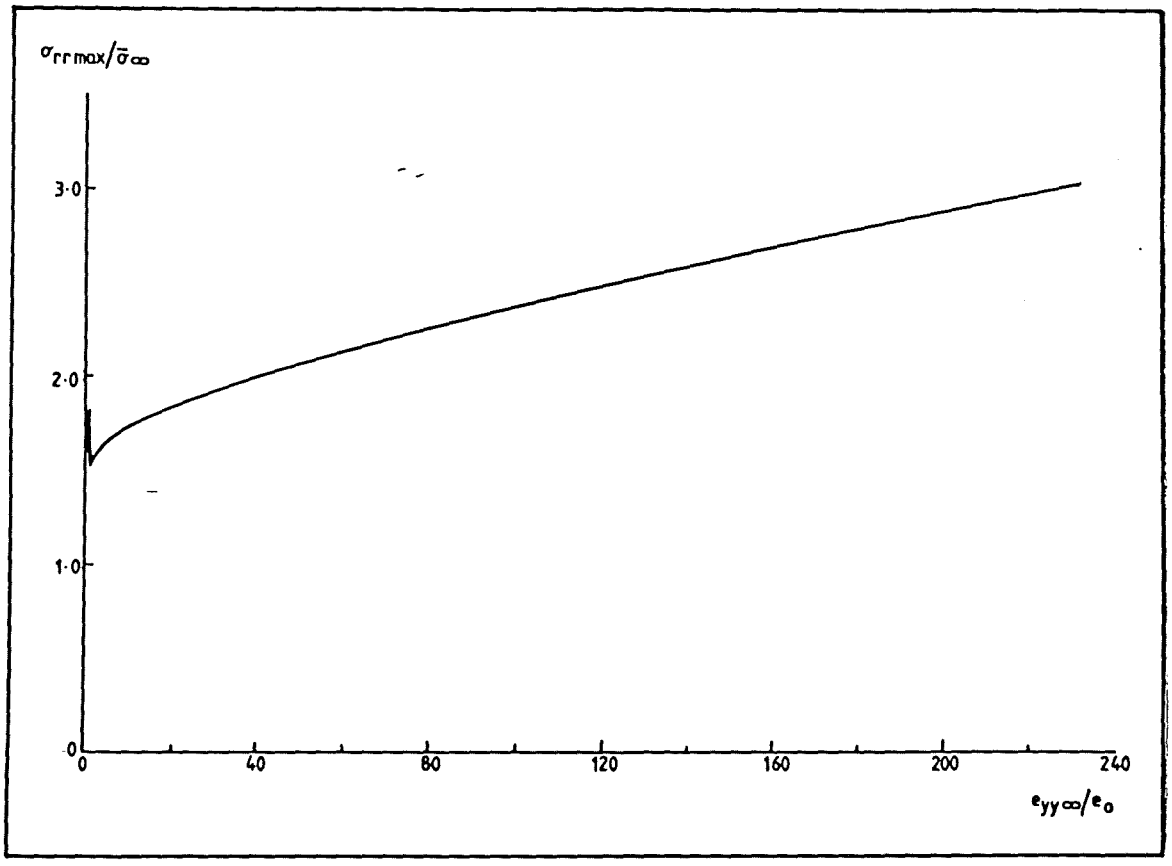

Fig.5.8. The development of the maximum interfacial radial stress around a rigid spherical inclusion in an elastic/power-hardening-plastic matrix subject to remote uniaxial tensile loading.

Figure 5.9 plots the value of C for increasing remote strain and shows that the interfacial radial stress concentration is not a constant. Indeed this curve may be inferred from the graph of $\sigma_{rrmax}/\bar{\sigma}_\infty$ for any loading under constant remote triaxiality (fig.5.8). This is in contrast to the approximation of Argon, Im and Safoglu (1975) that the interfacial radial stress concentration is

constant for non-linearly hardening materials.

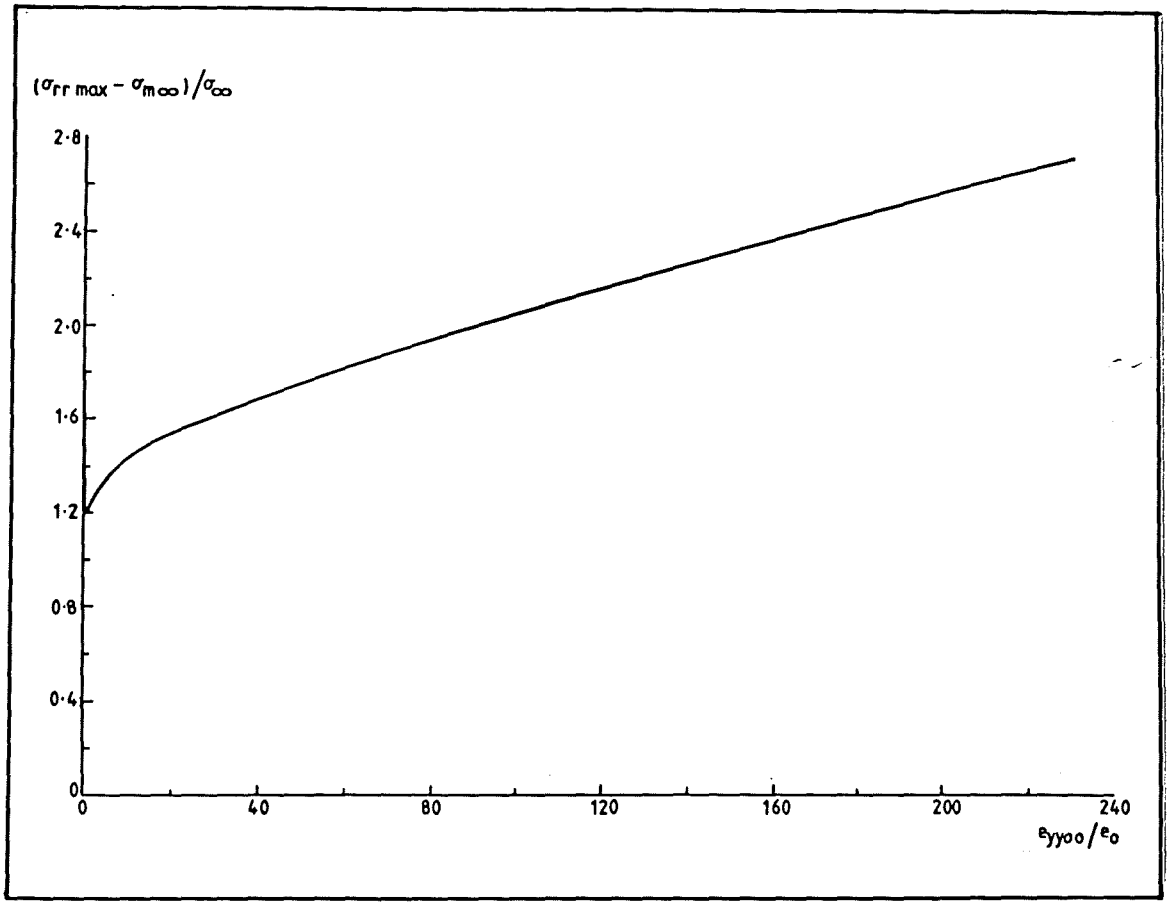

Fig.5.9. The development of the maximum interfacial radial stress around a rigid spherical inclusion in an elastic/power-hardening-plastic matrix in a remote deviatoric stress field.

It was noted from the numerical results that positive hydrostatic stresses developed in the direction of the pole of the inclusion even at small remote plastic strains while negative hydrostatic stresses develop opposite the equator as the deformation continues. This is a feature of all the inclusion analyses and results from the pinning effect of the rigid inclusion. In this context the effect is to increase the local triaxiality near the inclusion, indicating that the local stress state need not reflect the remote loading conditions.

5.2. A RIGID INCLUSION IN AN ELASTIC, PERFECTLY PLASTIC MATRIX.

A similar analysis to that described in section 5.1 was performed for a rigid inclusion in an elastic/perfectly plastic matrix. The elastic constants were identical to those in the power hardening case ie σ_0 = 0.14 GPa and E = 210 GPa. The same finite element mesh was retained and was again subjected to increments of remote uniaxial displacement loading. The results of this large strain analysis of a non-hardening material showed similar trends to that of the power hardening analysis in the development of the plastic strain field (eg fig.5.10) and the corresponding stress fields.

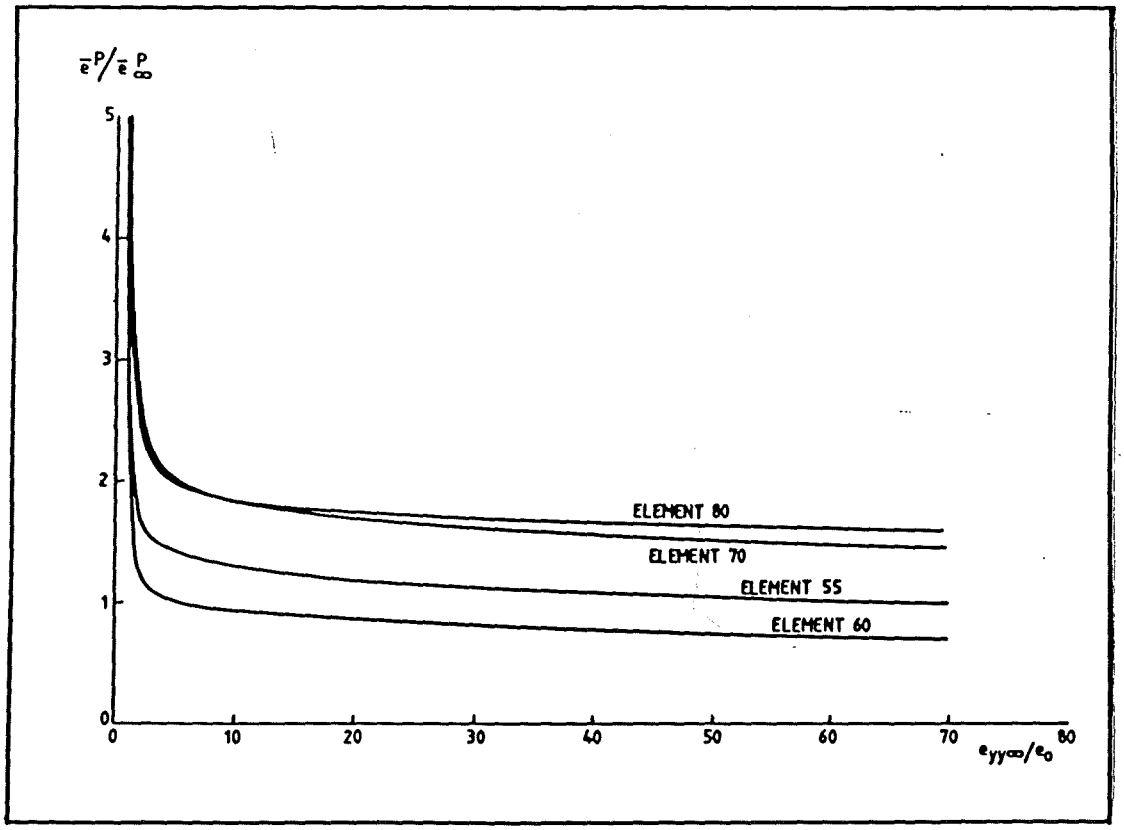

Fig.5.10. The development of the plastic strain in some significant elements near a rigid spherical inclusion in an elastic/perfectly-plastic matrix subject to remote uniaxial tension.

The mean stress concentration due to the inclusion again results in a local increase in the triaxiality of the stress state, but for a non-hardening matrix, the flow stress in every plastically deforming element will be the initial yield stress $\sigma_0 = 0.14$ GPa. The corresponding concentration of the effective stress will produce local plastic flow near the interface even for remote stresses which are still in the elastic range. Hence a graph of σ_{rrmax} normalised with respect to the (constant) flow stress will have a different form to that normalised with respect to the remote effective stress (fig.5.11).

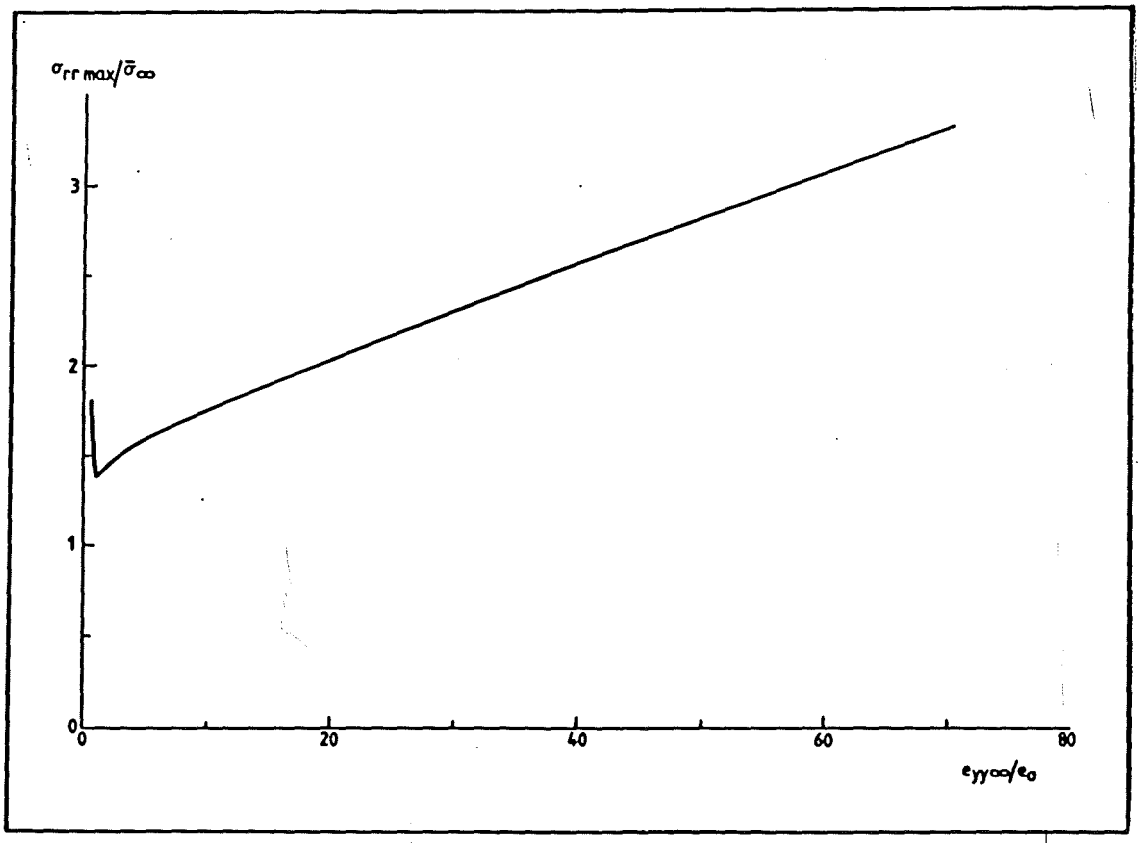

Fig.5.11. The development of the maximum interfacial radial stress around a rigid spherical inclusion in an elastic/perfectly-plastic matrix subject to remote uniaxial tension.

Since the remote triaxiality is constant (=1/3) in uniaxial tension, the variation of the maximum interfacial radial stress in a purely deviatoric remote stress state (fig.5.12) has a similar form to fig.5.11.

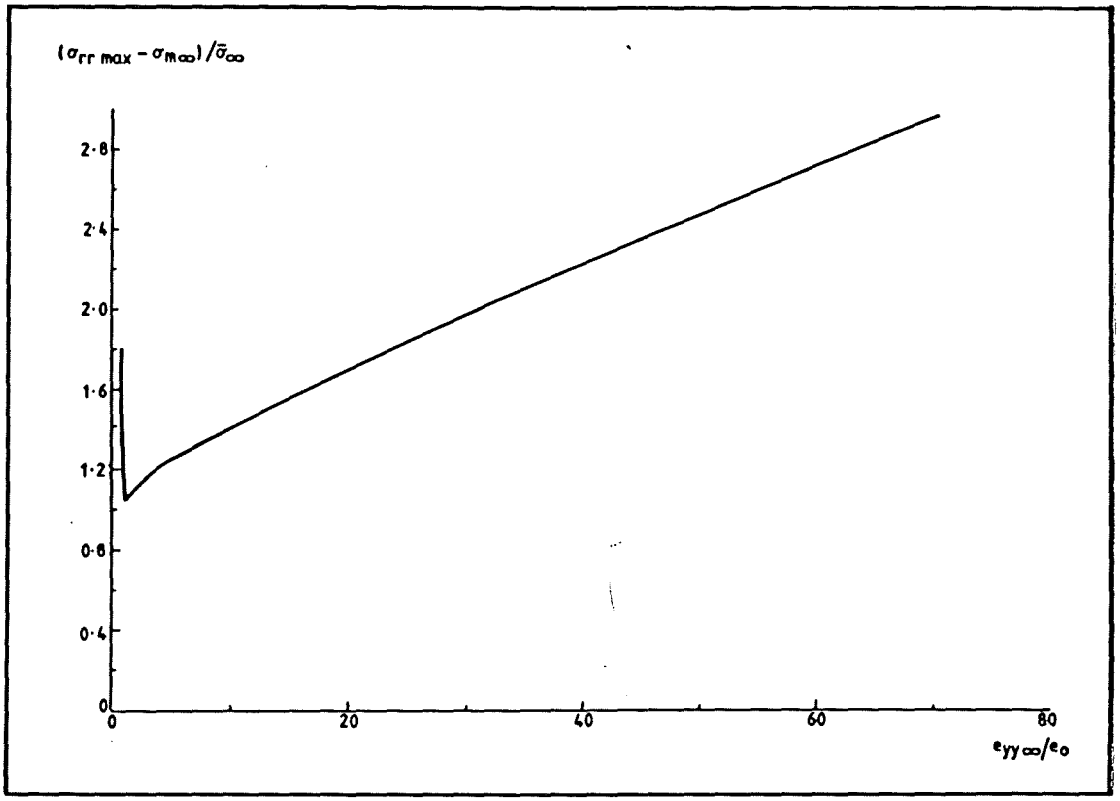

Fig.5.12. The development of the maximum interfacial radial stress around a rigid spherical inclusion in an elastic/perfectly-plastic matrix in a purely deviatoric remote stress field.

5.3. A RIGID INCLUSION IN A HIGH MODULUS, PERFECTLY PLASTIC MATRIX.

It is not possible to specify infinite elastic stiffness in the finite element program used but the behaviour of such a material may be inferred from that of an elastic/perfectly-plastic material with a high elastic modulus. A finite element analysis was therefore performed with a matrix elastic modulus of 10^6 GPa. Increments of remote displacement loading were applied up to a total remote strain

of 0.05% which though absolutely small, nevertheless corresponds to approximately 3500 times the initial yield strain. The trends of the results were similar to the previous analyses in that while the plastic strain concentration did appear to approach a constant value no steady state occurred for the maximum interfacial radial stress.

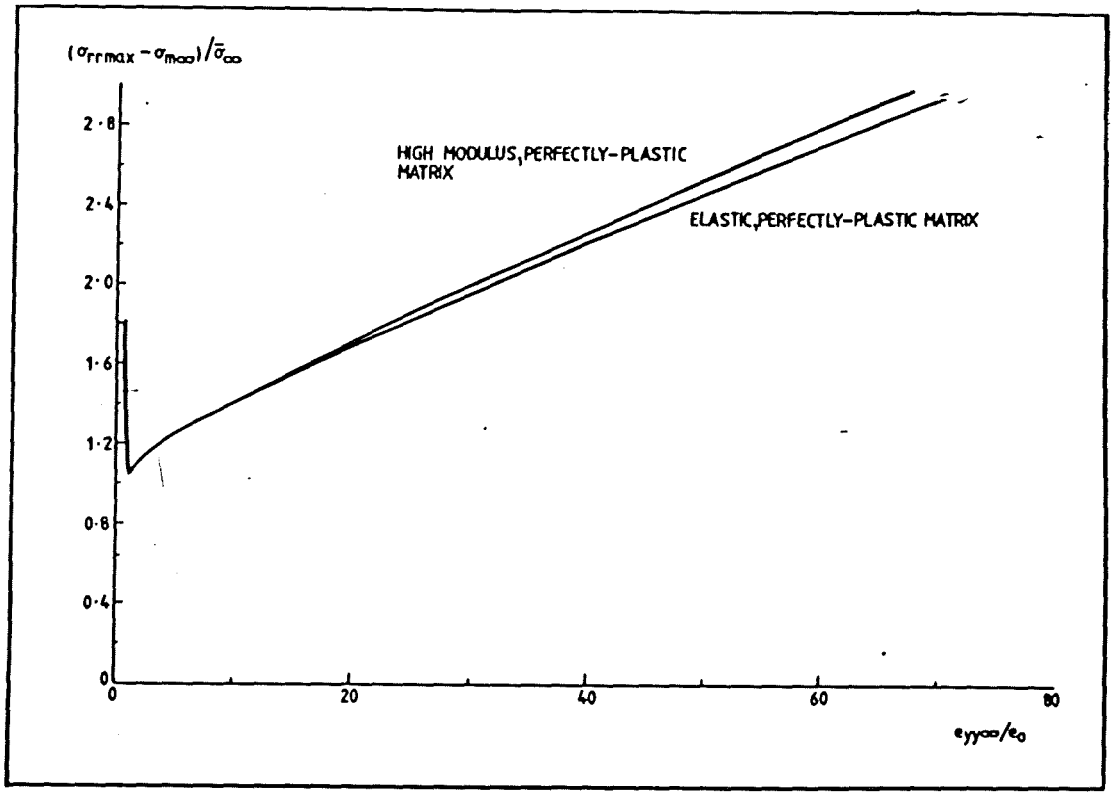

Fig.5.13. The development of the maximum interfacial radial stress around inclusions in elastic/perfectly-plastic and high-modulus/perfectly-plastic matrices in purely deviatoric remote stress fields.

The increase of the maximum interfacial radial stress was too rapid to be expressed as a meaningful function of absolute remote load but can be conveniently shown by plotting the interfacial radial stress concentration against the remote strain normalised with respect to the initial yield stain e_0 of $0.14/10^6$. With this scaling factor, the interfacial radial stress concentration is seen to develop in

a manner which is very similar to that for the elastic/ perfectly-plastic material up to strains of the order of 80 times e_0 (fig. 5.13), although the curves are very different when plotted as functions of absolute strain. This emphasises the importance of the elastic response of the matrix.

5.4. AN OXIDE INCLUSION IN AN IRON MATRIX.

Swedish Iron is a metallurgically simple material containing a single population of large iron oxide inclusions. The nature of the inclusion/matrix interface in this material is of direct relevance to associated experimental work described later. However the elastic constants of iron and the only oxide for which figures were available (Fe_3O_4) are (American Handbook of Physics):

	C_{11}	C_{12}	C_{44}
Fe	237	141	116 GPa
Fe_3O_4	273	106	97 GPa

A finite element model which considers the inclusion to be rigid will thus not give a reasonable description of the behaviour of Swedish Iron, in which the iron matrix and oxide inclusions have similar elastic constants. The behaviour of this system has been investigated by a finite element analysis of an elastic inclusion in an elastic/ strain-hardening matrix.

Deformation of the inclusion was permitted by removing the

displacement boundary conditions around the inclusion/matrix interface and extending the constraints along the coordinate axes to the origin, including the nodes within the inclusion itself. The inclusion and matrix were both specified as having an elastic modulus of 210 GPa with Poisson's ratio of 0.3, but while the matrix was given a yield stress of 0.14 GPa as before, the specification of a yield stress of 10^6 GPa for the inclusion elements ensured that the deformation of the inclusion was purely elastic.

For the analysis of this real material it was considered advisable to avoid the limitations of a power law through the use of a piecewise-linear approximation to the stress-strain equations of Swedish Iron (fig.4.2), through the relations.

$\bar{\sigma}/\bar{\varepsilon}^p$	$< \bar{\varepsilon}^p_\infty <$
2.00	0.00 - 0.05
1.00	0.05 - 0.01
0.50	0.10 - 0.20
0.33	0.20 - 0.35
0.28	0.35 - 0.75
0.24	0.75 - .

This finite element analysis was found to be numerically stable up to very large plastic strain and remote displacements were applied to give a final absolute remote strain of 47% or 700 times the initial yield strain. This range is sufficient to cover the expected limits of void nucleation. Stress and strain gradients develop progressively within the inclusion itself with the maximum values of

σ and e_{yy}^{el} (there is no plastic strain within the inclusion) occurring near the interface at approximately $\pi/4$ to the axes in element 44 and the minimum values occurring in the central elements eg element 4. Graphs of the effective stress and elastic strain component in these elements (figs.5.14 and 5.15) show this progressive development but it would be acceptable to consider the elastic deformation of the inclusion to be homogeneous up to remote strains of the order of 10 times the matrix yield strain.

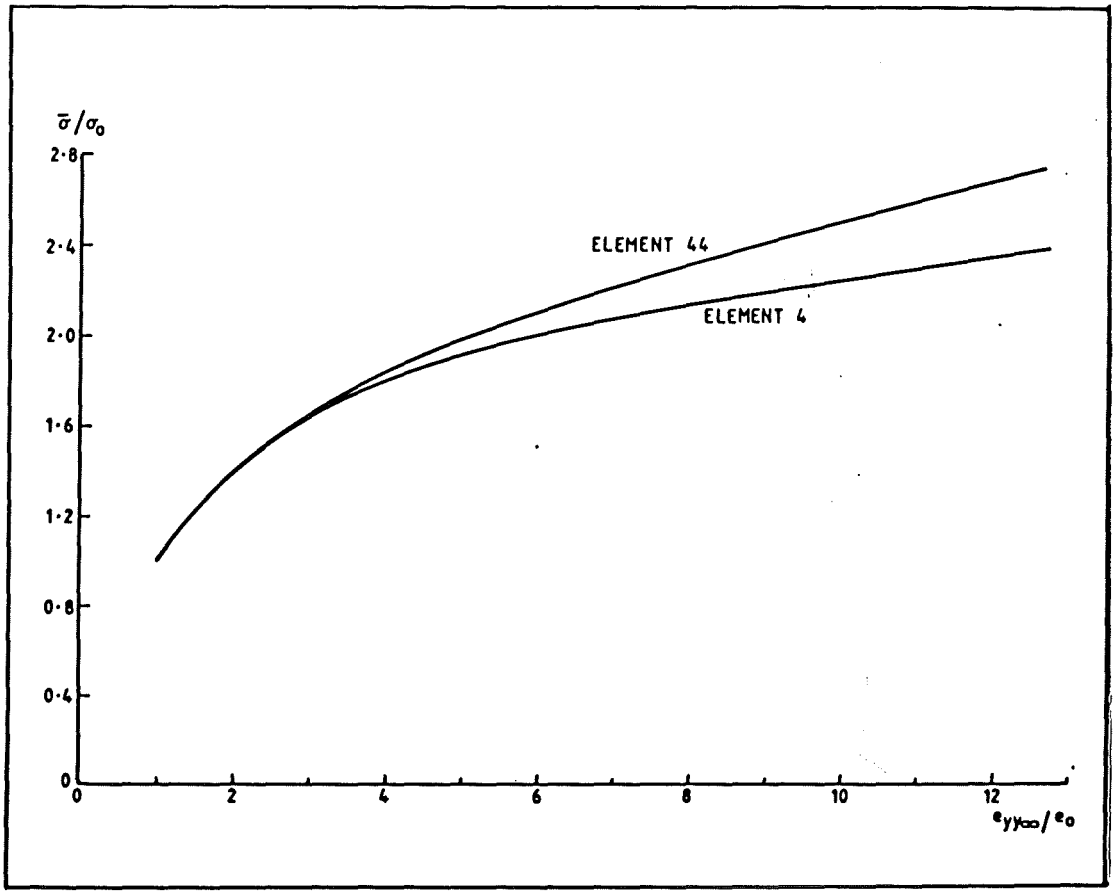

Fig.5.14. The development of the effective stress gradient across a spherical elastic inclusion in an elastic/piecewise-linear-plastic matrix in a purely deviatoric remote stress field.

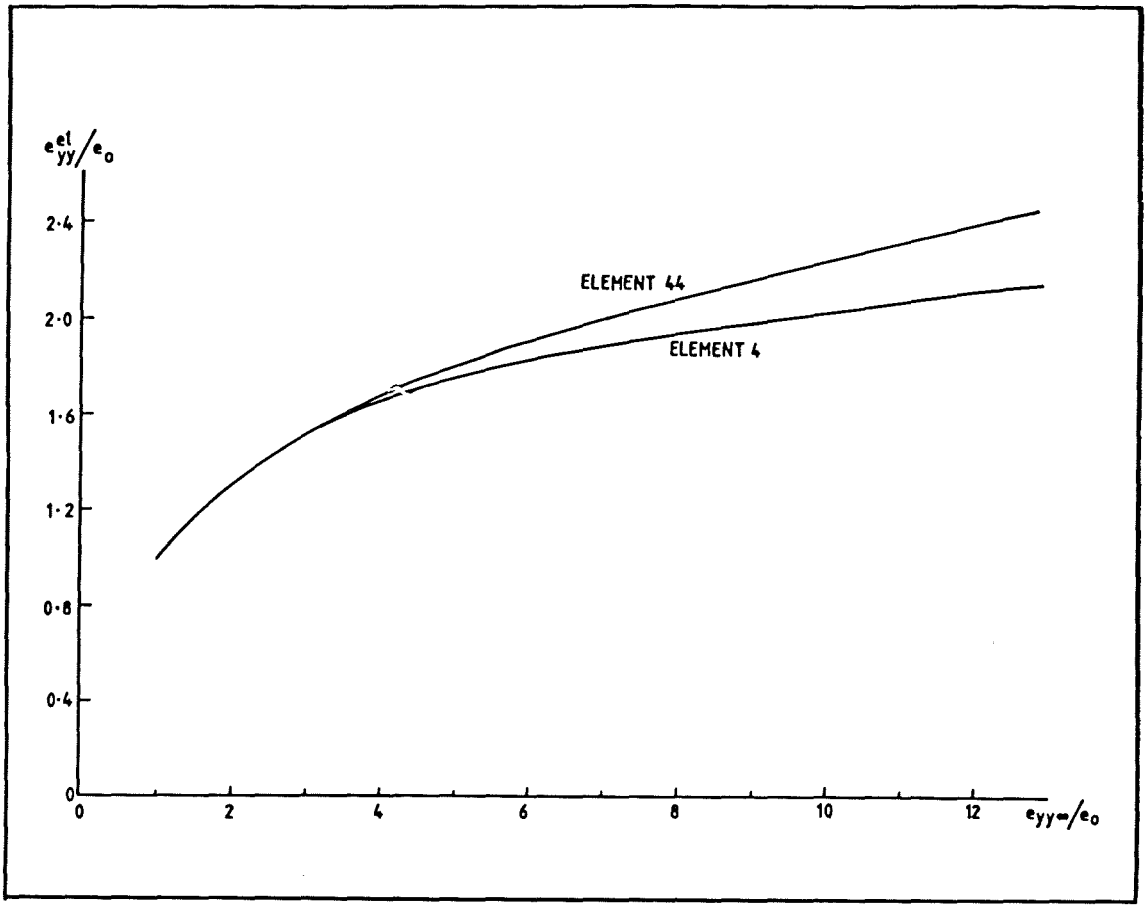

Fig.5.15. The elastic strain gradient across a spherical elastic inclusion in an elastic/piecewise-linear plastic matrix in a purely deviatoric remote stress field.

The plastic strain concentrations near the interface behave in a similar manner to the previous analyses although in the case of the elastic inclusion the approach to a steady state is less rapid than previously (fig.5.16). The variation of the maximum interfacial radial stress concentration with $\bar{e}^p_\infty/e_0$, approximately equal to $e_{yy\infty}/e_0$, is shown in fig.5.17. Again the radial stress concentration on the interface does not reach a steady state.

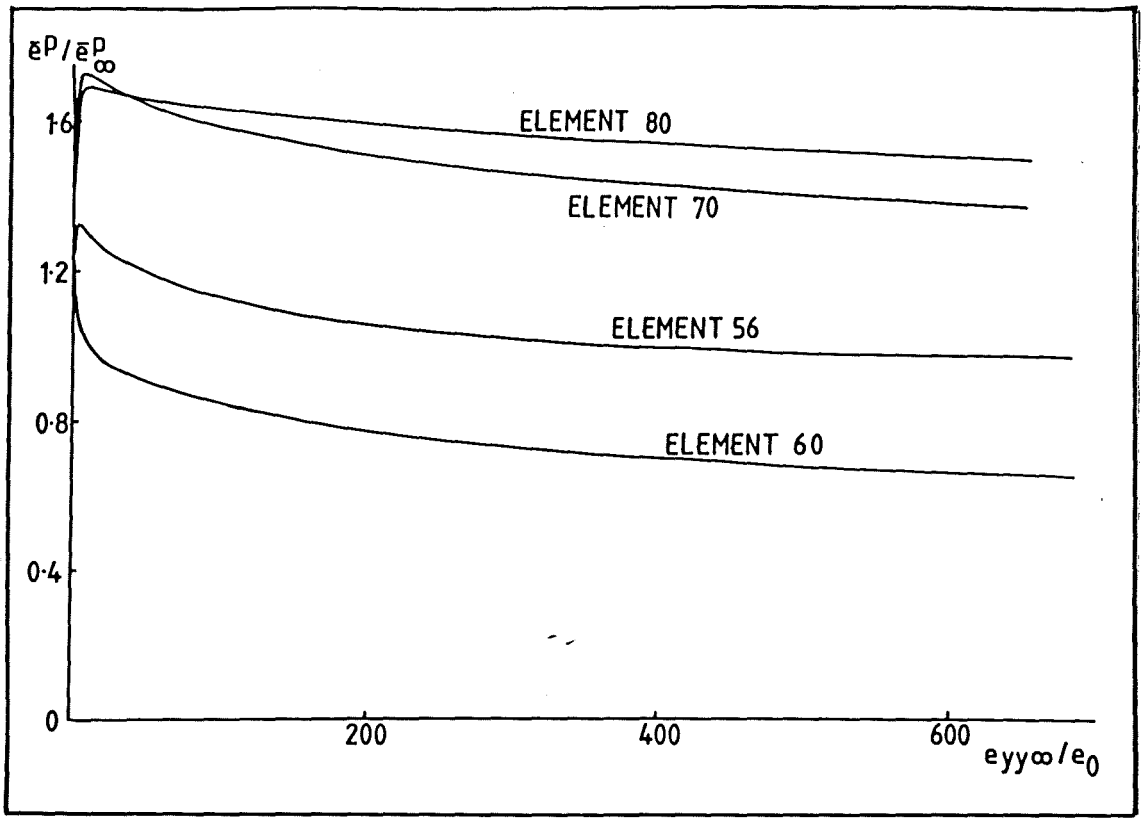

Fig.5.16. The development of the plastic strain in some significant elements near a spherical elastic inclusion in an elastic/piecewise-linear-plastic matrix subject to remote uniaxial tension.

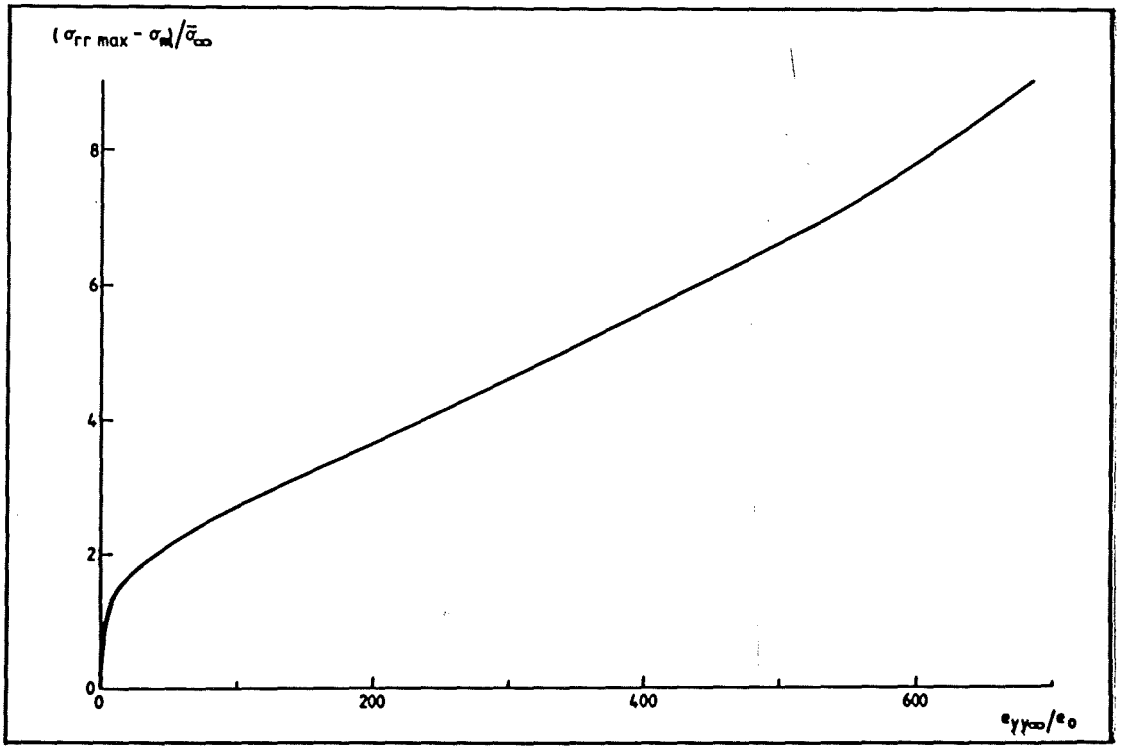

Fig.5.17. The development of the maximum interfacial radial stress around a spherical elastic inclusion in an elastic/piecewise-linear-plastic matrix in a purely deviatoric remote stress field.

Using a minimax curve fitting routine (NAG Manual), σ_{rrmax} was fitted to power laws of the form:

$$y = ax^n \quad (n \in R \text{ ie not necessarily an integer})$$

and polynomials of various orders of the form:

$$y = a_0 + a_1x + a_2x^2 + a_3x^3 + \ldots$$

No suitable power law was found (fig.5.18) and the best compromise between simplicity and accuracy of the polynomial was found with a 6th order equation (fig.5.19):

$$C = 8.33.10^{-1} + 5.16.10^{-2}e_n - 7.13.10^{-4}e_n^{\,2} + 4.62.10^{-6}e_n^{\,3} - 1.40.10^{-8}e_n^{\,4} + 1.96.10^{-11}e_n^{\,5} - 1.02.10^{-14}e_n^{\,6}$$

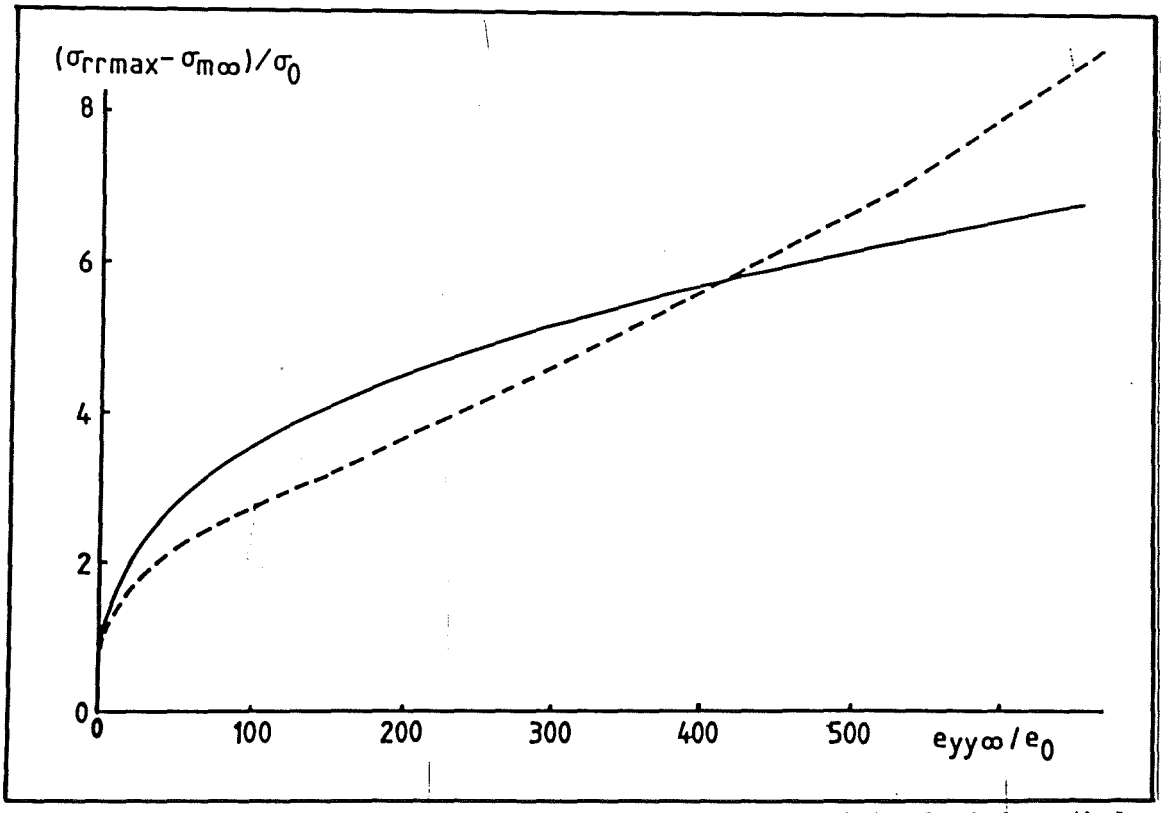

Fig.5.18. The best power law fit to the maximum interfacial radial stress around a spherical elastic inclusion in an elastic/piecewise-linear-plastic matrix in a purely deviatoric remote stress field.

where e_n is the effective plastic strain $\bar{e}^p_\infty$ normalised with respect to the initial yield strain e_0 and C is the maximum interfacial radial stress concentration factor as before. Such a relation is however prone to conditioning problems at large values of e_n due to the high powers involved. Although no simple analytic expression was found to relate maximum interfacial radial stress to the remote loading, for specific materials such as Swedish Iron, subjected to finite strains it is perfectly adequate to express the variation of maximum radial stress in a piecewise analytic form.

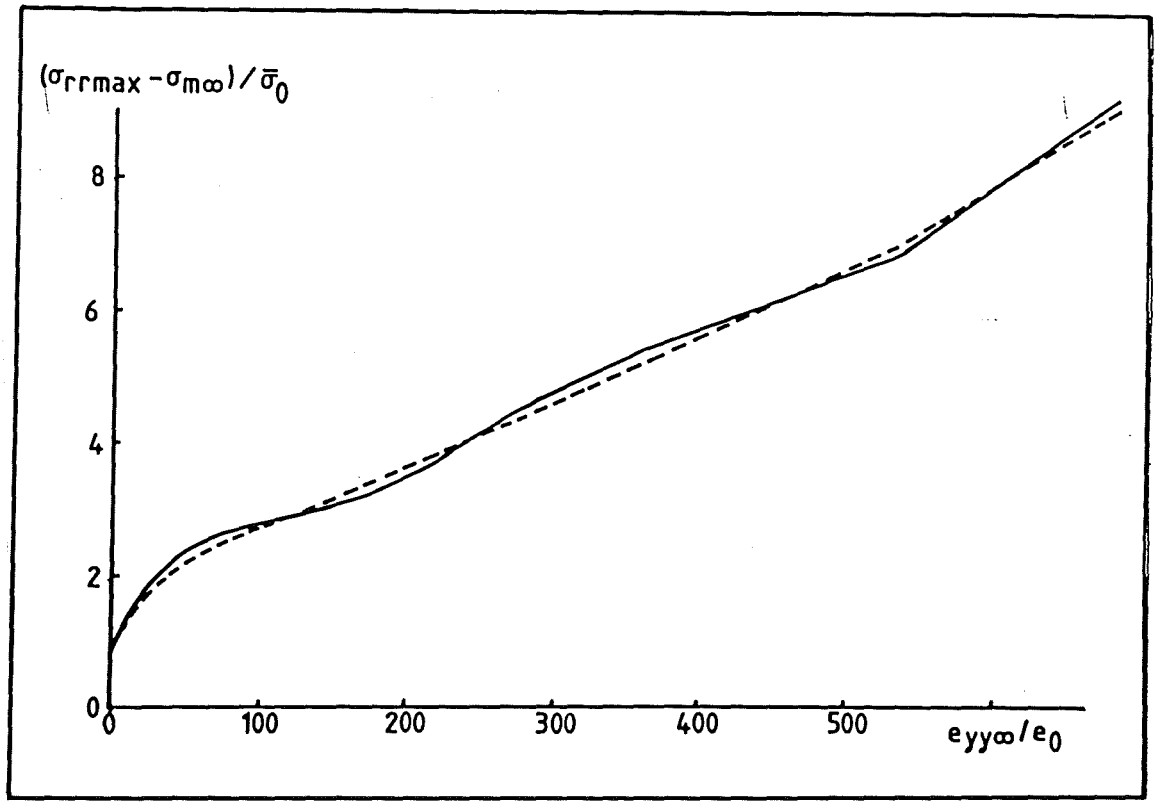

Fig.5.19. The best polynomial fit using a minimax technique to the maximum interfacial radial stress around a spherical elastic inclusion in an elastic/piecewise-linear-plastic matrix in a purely deviatoric remote stress field.

In the case of Swedish Iron, the simplest expression which gave a good description of the interfacial radial stress concentration was found to comprise a quadratic segment and two linear segments such that:

$$C = -3.89.10^{-4} e_n^{\,2} + 4.83.10^{-2} e_n + 0.8 \qquad 0 < e_n < 60$$

$$C = 9.79.10^{-3}(e_n - 60) + 2.3 \qquad 60 < e_n < 530$$

$$C = 1.40.10^{-2}(e_n - 530) + 6.9 \qquad 530 < e_n \quad .$$

(equ.5.1).

6. DISCUSSION.

The study of the stress and strain fields around an elastic inclusion in a plastically deforming matrix is motivated towards the determination of the local conditions which lead to failure of the interface. Initially it is instructive to examine the conditions at the pole of an inclusion where symmetry conditions require that the interfacial shear strain be zero. For the rigid inclusion, compatibility demands that the total matrix hoop strains $e_{\theta\theta}$ and $e_{\phi\phi}$ are zero. These total strains can however have an elastic and a plastic component such that:

$$e^{el}_{\theta\theta} + e^{p}_{\theta\theta} = 0$$

$$\text{and} \quad e^{el}_{\phi\phi} + e^{p}_{\phi\phi} = 0$$

Plastic flow at the pole is then only possible provided that plastic strains are balanced by equal and opposite elastic strains. It must then be concluded that in the polar region the elastic strains cannot be neglected. The coupling between the elastic and plastic strains is illustrated by comparing the behaviour of the high modulus/perfectly plastic material with that of the elastic/perfectly plastic material. While the maximum interfacial stresses develop much more rapidly in absolute terms for the high modulus matrix, σ_{rrmax} develops in a similar way when scaled in terms of the initial yield strain.

A feature of all the numerical solutions presented is the lack of a steady state solution. In such a solution, the stress and strain concentrations are time-independent provided geometry changes are insignificant and in a rigid/perfectly-plastic problem this us-

ually occurs soon after general yield. In finite-elastic/perfectly-plastic materials it might be expected that a steady state would be reached when the elastic strains become insignificant relative to the plastic strains but for the inclusion this condition is never reached at the pole as long as it continues to deform plastically. A steady state stress concentration may be attained in this location only if the polar material stops deforming and becomes rigid but the plastic strain concentration tends very slowly to zero and while the polar elements might ultimately stop deforming, this condition has not been reached by any of the numerical solutions, including those of Argon, Im and Safoglu (1975) and of Orr and Brown (1974).

In the elastic solution the maximum interfacial radial stress occurs at the pole. A common feature of all the elastic/plastic solutions is that the development of the maximum effective plastic strain at $\pi/4$ to the loading direction displaces the position of the maximum radial stress by one element around the interface, away from the pole. This shift in the position of the maximum interfacial stress not does affect the validity of the argument for the pole but the existence of a shear strain may allow steady state to be reached earlier at this location. It is clear however that the proximity of the maximum interfacial stress to the pole means that the elastic strains are significant and the finite elastic response of the matrix inhibits the development of steady state to such an extent that interfacial failure in real materials is unlikely to occur in steady state conditions.

The conclusion that in all the large strain solutions the maximum interfacial radial stress will continue to rise as the remote strain increases to more than two orders of magnitude times the init-

ial yield strain, even for a non-hardening matrix is similar to that reached by Orr and Brown (1974), in contrast to that of Argon, Im and Safoglu (1975). The latter analysis was however restricted to effective plastic strains of the order of the matrix yield strain and when the scale at the lower end of fig.5.9 for the elastic/power-hardening matrix was expanded to give fig.6.1, the value of the interfacial stress concentration was found to initially fall to a value of 1.2 at a remote strain of the order of the initial yield strain in broad agreement with Argon, Im and Safoglu (1975).

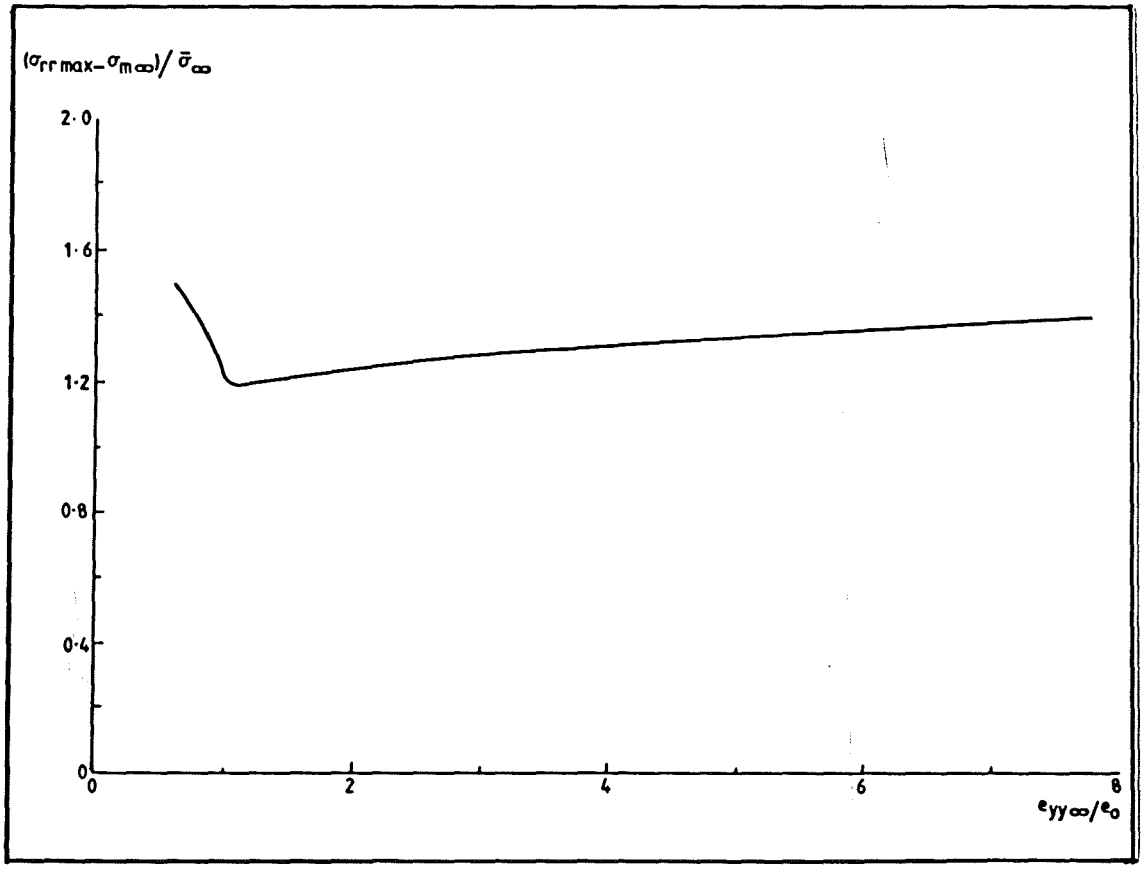

Fig.6.1. The development of the maximum interfacial radial stress around a rigid spherical inclusion in an elastic/power-hardening-plastic matrix in a small, purely deviatoric remote stress field.

As the loading continued the interfacial stress concentration began to rise again and the apparent approach to a steady state is shown as the approach to a minimum point. This minimum and the lack of a steady state in the development of the maximum interfacial radial stress are also features of the analyses of a hardening material.

The nature of the interface in Swedish Iron was investigated using an elastic inclusion embedded in a matrix whose experimentally determined stress-strain curve was modelled in a piecewise-linear fashion. As noted by Eshelby (1957), the initial stresss and strain fields within the inclusion are homogeneous but with increasing deformation, stress and strain gradients develop with maximum values of $\bar{\sigma}$ and e_{yy}^{el} occurring near the interface at approximately $\pi/4$ to the axes and with minimum values in the central elements. For Swedish Iron, the development of the interfacial radial stress (fig.5.17) has been approximated by the piecewise analytic expressions.

$$C = -3.89.10^{-4}(e_n)^2+4.83.10^{-2}(e_n) +0.8 \qquad 0<(e_n)< 60$$
$$C = 9.79.10^{-3}((e_n) - 60) +2.3 \qquad 60<(e_n)<530$$
$$C = 1.40.10^{-2}((e_n) -530) +6.9 \qquad 530<(e_n) \quad ,$$

where:

$$e_n = \bar{e}^p_{\infty}/e_0.$$

These expressions will be used to determine the interfacial conditions leading to void nucleation at hard particles. Similar expressions for elastic/power-hardening and elastic/perfectly-plastic matrices with rigid inclusions may be extracted from fig.5.9 and fig. 5.12 but care should be exercised in extrapolating beyond the ranges shown on the graphs.

PART 3: VOID NUCLEATION IN DUCTILE MATERIALS.

7. EXPERIMENTS.

7.1. THE LABORATORY SIMULATION OF SERVICE LOADING.

Hancock and Mackenzie (1976) have noted the effect of the triaxiality of the state of stress, measured by the non-dimensional parameter $\sigma_m/\bar{\sigma}$, on the strain to initiate failure in several materials. It then seems reasonable to assume that the nucleation of voids at hard particles may also depend on the local stress state and, perhaps, the strain state. Experiments should therefore be performed in a range of stress and strain states.

The simple uniaxial tensile test is the easiest experiment to perform but the analysis is complicated by the fact that the triaxiality of the stress state is only constant (= 1/3) up to the onset of necking. Thereafter the constraint on the material within the neck starts to increase. A machined initial curvature of the neck can however be used as a means of increasing the triaxiality in a tensile test and following McClintock (1968), Hancock and Mackenzie (1976) machined blunt notches of predetermined dimensions in tensile specimens in order to begin deformation at a triaxiality greater than 1/3. In the present work such notch tensile tests were chosen as a convenient method of nucleating voids and initiating failure in a range of stress states.

7.2. THE MATERIAL.

Swedish Iron is a commercially pure iron (fig.7.1) containing 1% volume fraction of iron oxide particles. With diameters distributed about a mean of 5μm the average particle spacing is approximately 20μm between centres, which is small compared to the grain size of 500μm (fig.1.5).

Element	% by weight
C	0.040
Mn	0.001
Si	0.013
S	0.005
P	0.014

Fig.7.1. The chemical composition of Swedish Iron (% by weight).

This single generation of large inclusions does not contribute significantly to the strength of the alloy, which therefore has little structural use, but ensures that there is only one major source of voids which are well distributed throughout the material. Furthermore, the low carbon content of the matrix produces a low yield stress of 0.14 GPa but high ductility and the strongly strain hardening characteristics shown in fig.7.2. Failure may then be observed by the classical mechanism of void growth and coalescence and the material is ideally suited to the present work.

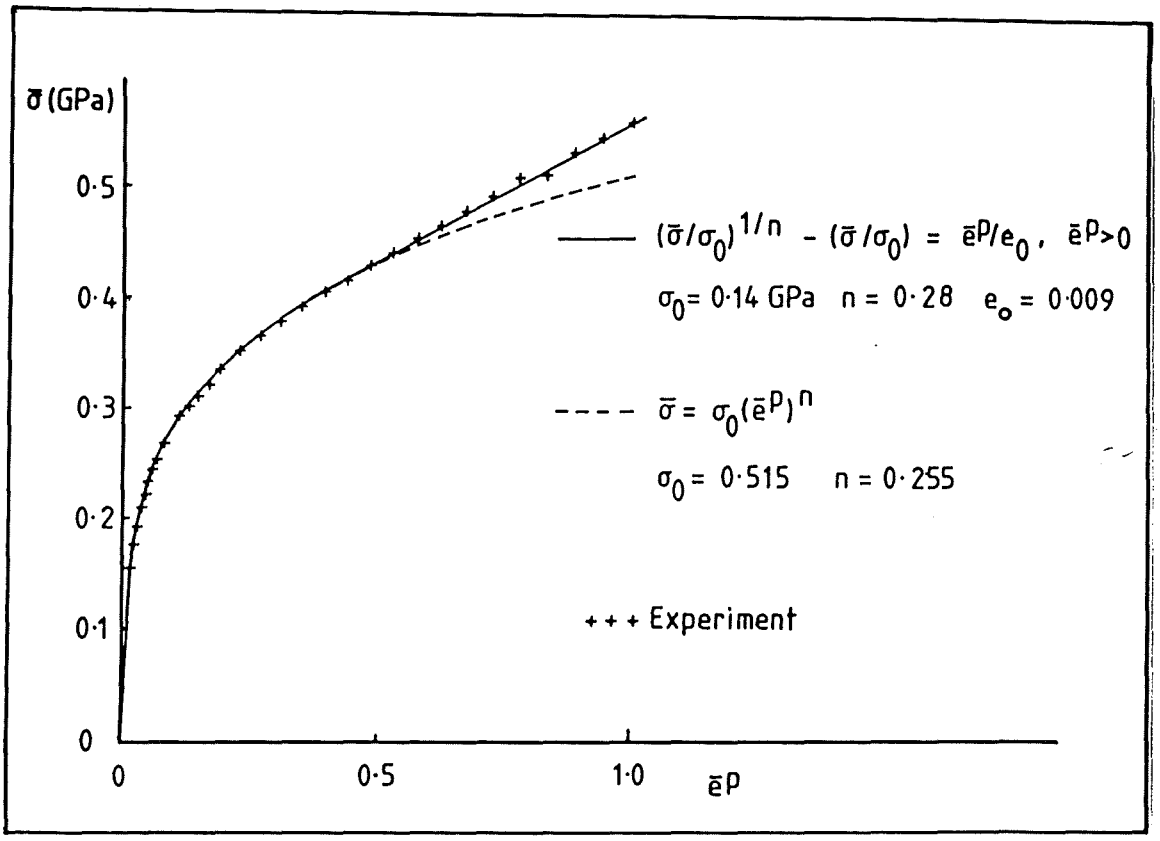

Fig.7.2. The stress-strain curve for Swedish Iron. The experimental points are shown together with two different forms of power-law used in the void growth equations and the finite element analysis respectively.

7.3. PROCEDURE.

Axisymmetric and plane strain specimens with the dimensions shown in fig.7.3 and fig.7.4 were tested under transverse strain control up to 'failure initiation' identified by Hancock and Mackenzie (1976) and Mackenzie, Hancock and Brown (1977) with the formation of a distinct internal crack. The main feature of the notched specimens is that plastic strain fields develop between the shoulders of the notch in a triaxial state of stress which is most severe at the centre of the specimen but falls away towards the free surface. Appropriate

choice of specimen geometries then allows void nucleation and growth to occur in a wide range of triaxial stress states.

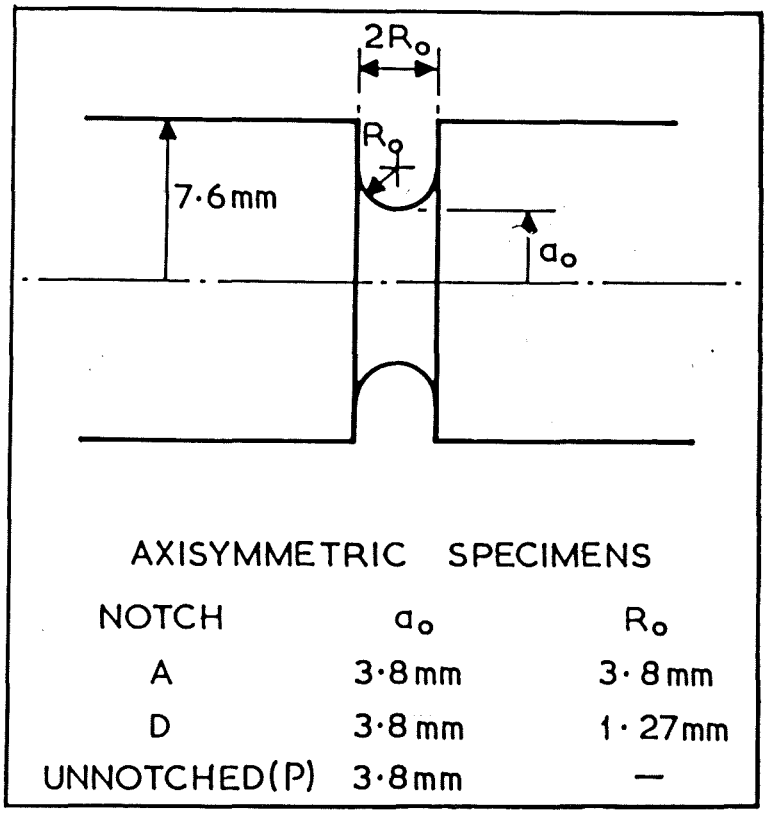

Fig.7.3. The dimensions of the notches in axisymmetric uniaxial tensile specimens.

The tests were carried out on an Instron 250 kN hydraulic machine with feedback control to the crosshead. The combination of a sufficiently stiff machine and load cell, and the small time constant of the controller, allowed load to be shed rapidly enough to maintain a constant strain rate in the neck of a tensile specimen to strains beyond the instabilities associated with both diffuse necking and failure initiation. Control was taken from the output of a longitudinally mounted extensometer clipped to the shoulders of the testpiece. For the notched tensile specimens tested, experience has shown that this gives

a constant rate of transverse strain at the minimum cross- section but avoids the instabilities resulting from surface roughness caused by the emergence of slip-bands at the minimum section.

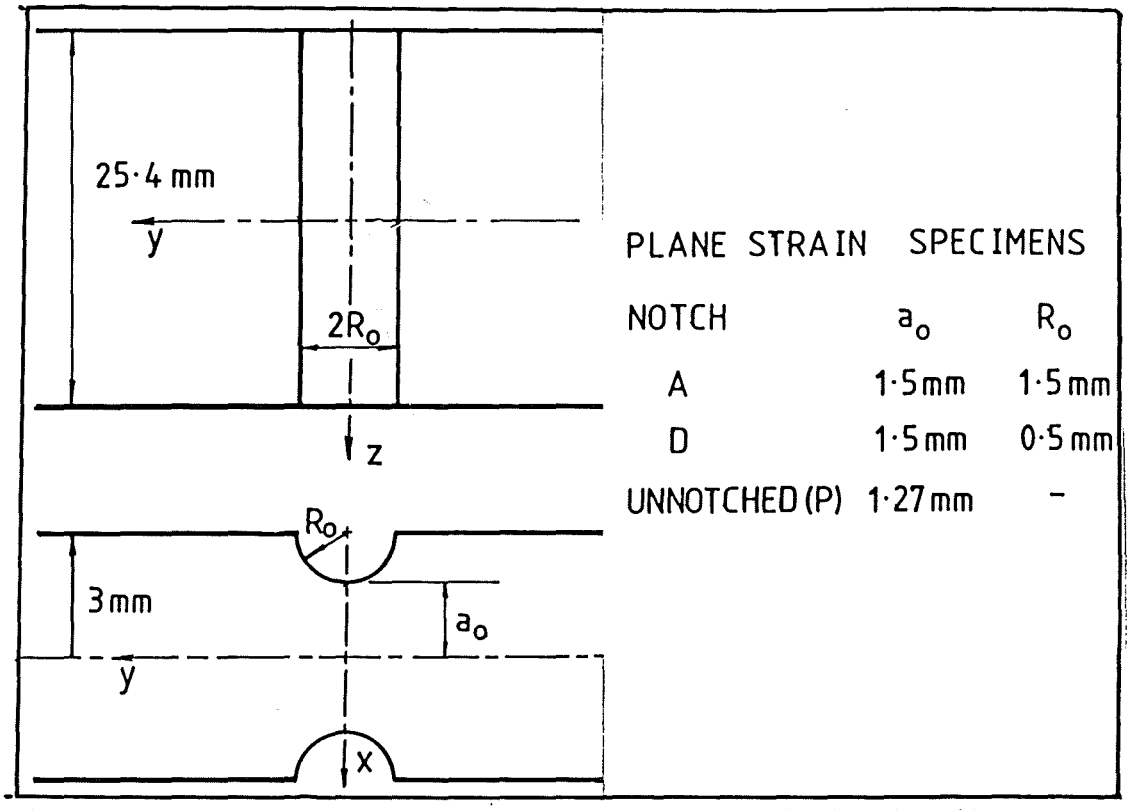

Fig.7.4. The dimensions of the plane strain uniaxial tensile specimens.

The local deformation at the minimum cross section was measured by a transversely mounted extensometer and displayed with the current load on a chart recorder. Other than in small regions of high porosity, deformation occurs at approximately constant volume and the decrease in the minimum diameter d can be related to the local effective plastic strain through:

$$\bar{e}^p = 2 \ln(d_0/d).$$

The reduction in the minimum diameter also gives the decrease in the

cross-sectional area which allows the effective true stress to be determined. On this basis, the results of a simple tension test were used to give the stress-strain curve for Swedish Iron (fig.7.2).

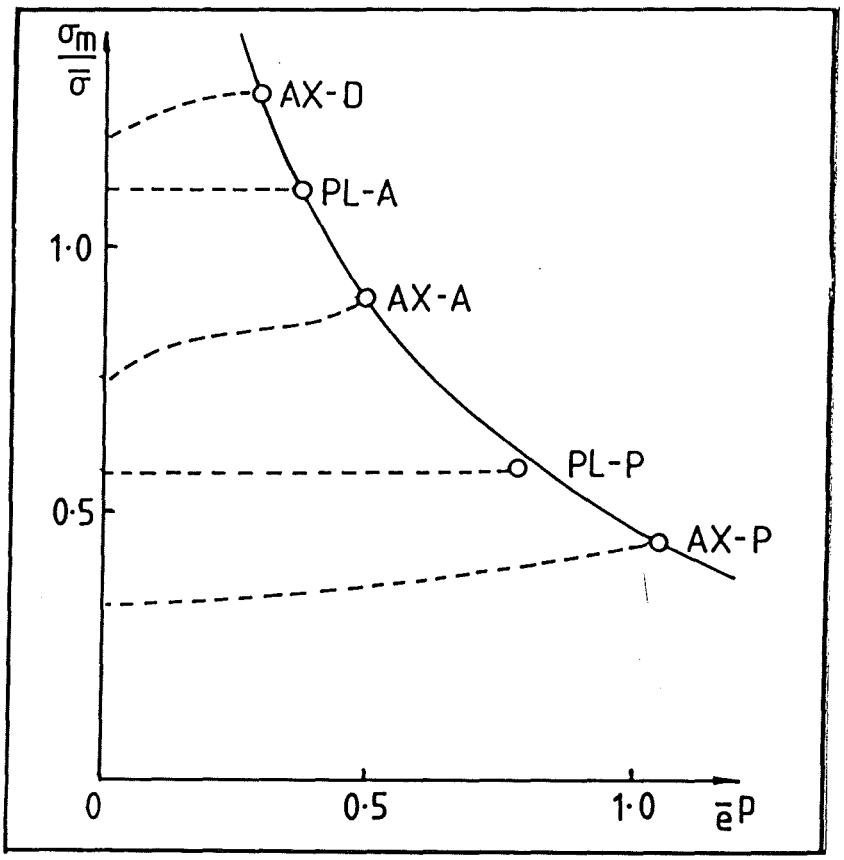

Fig.7.5. The failure locus for Swedish Iron, showing the development of the stress state with deformation for each specimen. The prefix AX denotes an axisymetric specimen while PL denotes a plane strain specimen. The suffix indicates the notch profile (fig.7.3).

The deformations which result in failure initiation for different specimen geometries are shown in fig.7.5 and the line drawn through the final points has been termed a failure locus. The particular notch geometries used were chosen since the triaxiality at any point on the transverse axis remains relatively constant throughout the loading history. Similar axisymmetric specimens to those used to

determine this failure locus were then tested to arbitrary strains sufficient to nucleate voids at most of the inclusions but not sufficient for void growth to initiate failure by internal cracking. A metallographic section through each specimen revealed the voids formed by decohesion of the inclusion-matrix interface as ellipses whose major diameters lay parallel to the direction of the local maximum principal stress (fig.7.6).

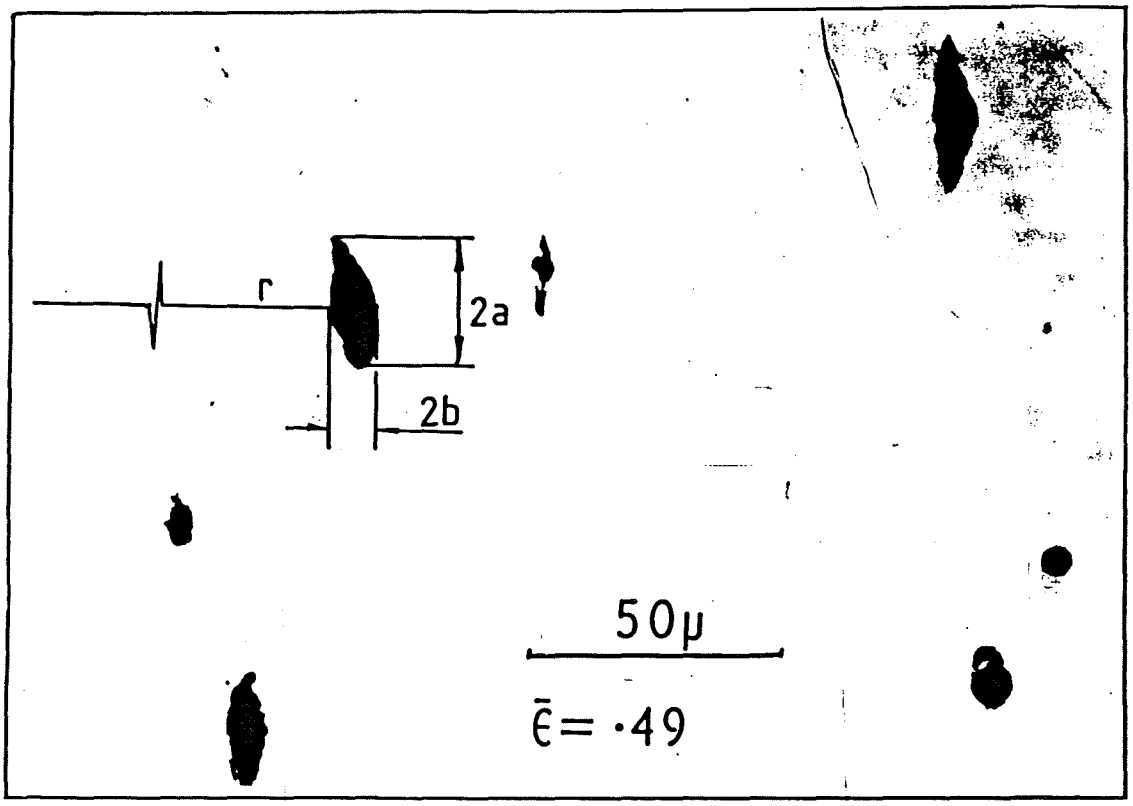

Fig.7.6. A metallographic section through a deformed specimen of Swedish Iron.

Micrographs taken across the transverse axis give measured values of the coordinate r of the centre of each ellipse and its semi-axes a and b. Since the void growth equations (equs.2.13) are non-dimensional, only the aspect ratio a/b of each ellipse is relevant to nucleation, and this is independent of the sectioning plane provided it is para-

llel to the axis.

Given a field analysis of each specimen geometry, as determined in the following chapter, the local deformation history for the centroids of elements lying on the transverse axis of each specimen may be extracted. Then, knowing the final coordinate r of each void, linear interpolation during a backward pass through these element histories allows the local deformation history at each void location to be tabulated, including the development of $\bar{\sigma}$, $\bar{e}^p$ and $\sigma_m/\bar{\sigma}$. From these void histories and the growth equations it is possible to calculate numerically the local conditions at nucleation and at failure initiation. A full explanation of the numerical algorithm is given in appendix A.2 and appendix A.3.

8. ANALYSIS.

8.1. FIELD ANALYSES OF UNIAXIAL TENSILE SPECIMENS.

The stress and strain distributions needed to calculate the void deformation histories and hence the local conditions at nucleation and failure may be obtained from field analyses of the appropriate specimen geometry. For simple specimen geometries these may be obtained analytically but for the more complex notched specimens, numerical analyses are required.

8.1.1. AXISYMMETRIC NOTCHED SPECIMENS.

Elastic/plastic finite element analyses of the axisymmetric notched specimens were performed using the finite element program described in appendix 1. The stress-strain curve of the material was represented by the power law of equ.4.1, viz:

$$(\bar{\sigma}/\sigma_0)^{(1/n)} - (\bar{\sigma}/\sigma_0) = (\bar{e}^p/e_0).$$

For the analysis of tensile specimens it is important that this power law reflects the strain hardening behaviour of the material and hence the curvature of the stress-strain law up to large plastic strains. With an initial yield stress in uniaxial tension of σ_0 = 0.14 GPa the best fit to the experimental stress-strain law for the Swedish Iron material used in associated experimental work is obtained with n = 0.28 and e_0 = 0.009 (fig.7.3).

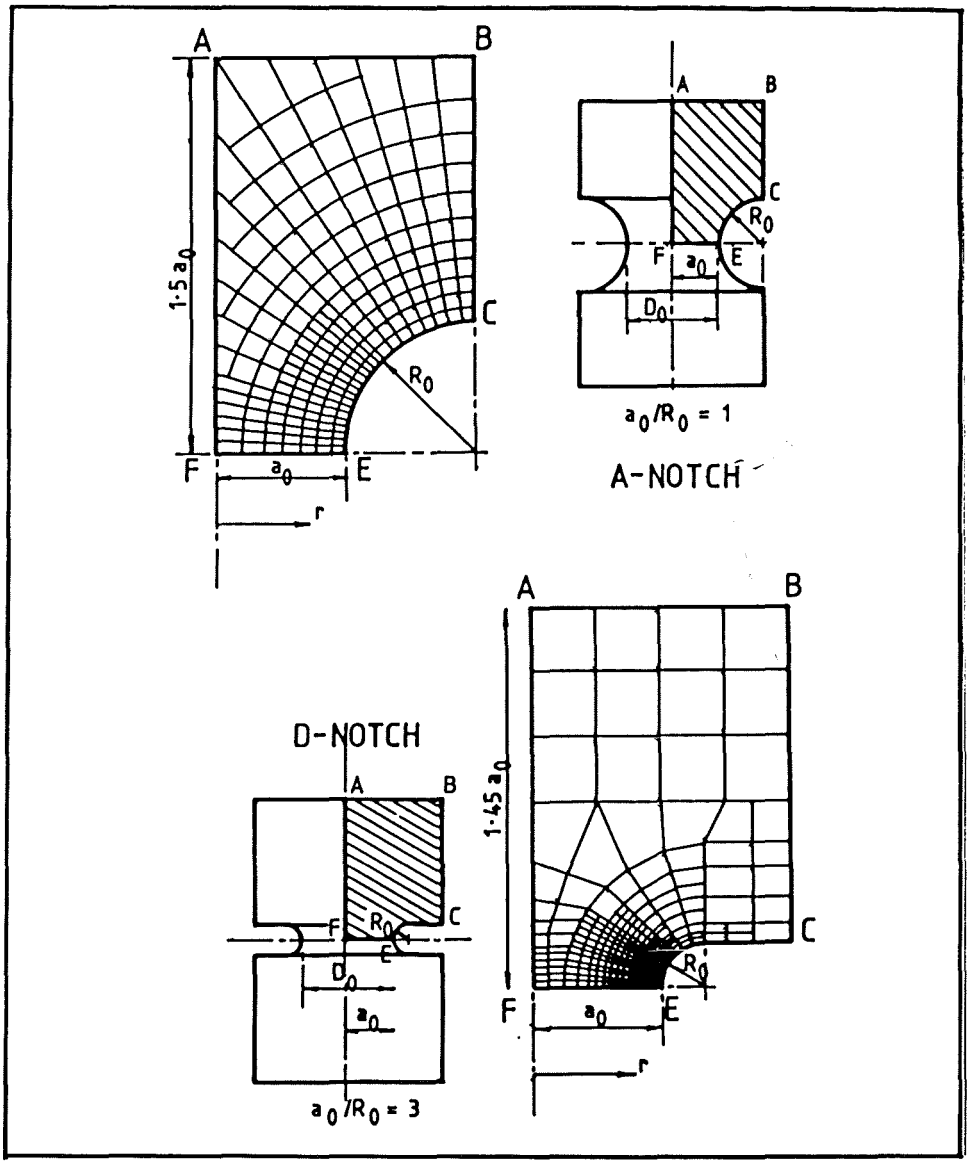

Fig.8.1. The finite element grids used in the analyses of notched tensile specimens (by permission of Dr DK Brown, Univ of Glasgow).

The matrix of the material is represented by the Von Mises yield surface of equ.3.3 written in the form:

$$\phi = (\bar{\sigma}/\sigma_y) - 1 = 0$$

where σ_y is the flow stress in uniaxial tension and the plastic strain components are determined from the associated flow rule for a

Von Mises yield function, ie the Prandtl-Reuss equations. The relevant finite element grids are given in fig.8.1.

A feature of the solutions is that plastic strain fields develop between the shoulders of the notches in a triaxial state of stress which is most severe at the centre of the specimen and falls towards the free surfaces, as in the real specimens although in the latter, void nucleation and growth imply that the porous material in the plastic zone will follow a dilating constitutive relation. However, following Brown, Hancock, Thomson and Parks (1980) the aggregate triaxiality $Z_m/\bar{Z}$ may be taken to be insensitive to increasing porosity and a non-dilating analysis using the constitutive relation of classical plasticity was chosen for the current analysis.

8.1.2. AXISYMMETRIC UNNOTCHED SPECIMENS.

The problem of the stress state in a naturally necking round bar was originally discussed by Bridgman (1952) and has subsequently been treated numerically by Needleman (1972) and by Norris, Moran, Scudder and Quinones (1978). The numerical analyses are broadly similar as regards the distribution of effective plastic strain across the minimum section which is found to be virtually constant and may be calculated from the remote displacements. The analyses do differ in the extent to which necking amplifies the remote stress state which in Needleman's (1972) analysis depends on the strain hardening rate.

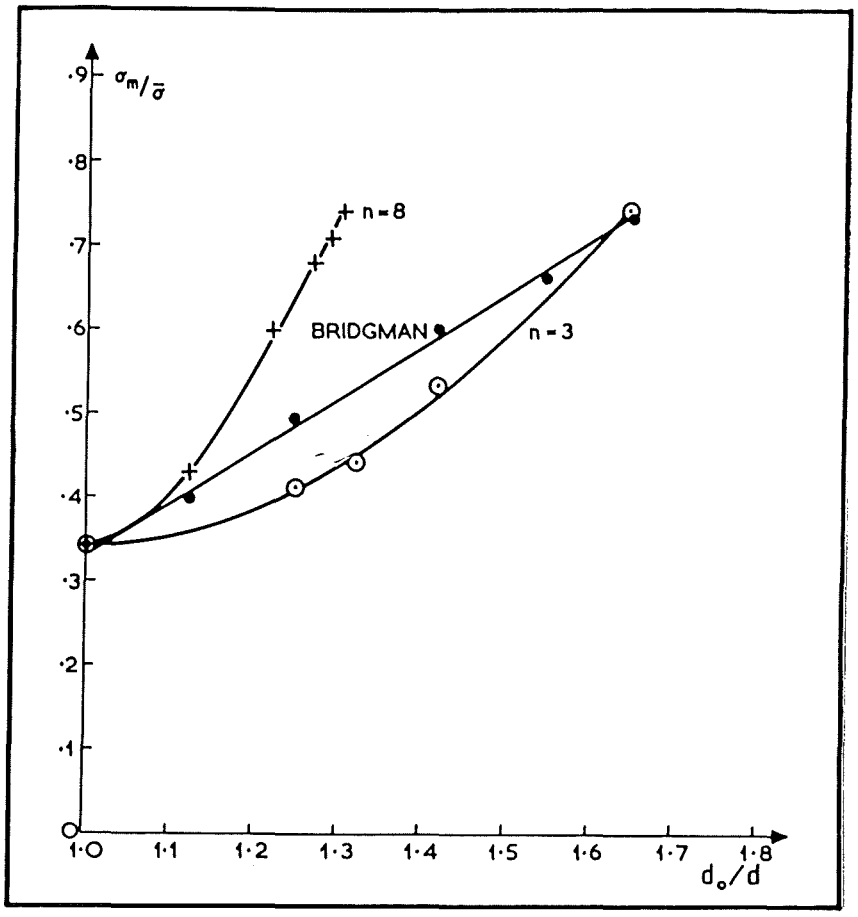

Fig.8.2. The development of the triaxiality of the stress state with deformation in a uniaxial tensile specimen. The uniaxial strain e_{yy} is given by 2 ln (d_0/d).

The notch current geometry parameter a/R for a deforming axisymmetric specimen is defined as the ratio of the radius of the minimum cross-section to the minimum radius of the longitudinal section and fig.7.3 gives the initial values a_0 and R_0. For a simple tensile specimen, R is the minimum radius of the neck and in the strongly hardening solution most appropriate to the current work, Needleman's (1972) and Bridgman's (1952) solutions concur near the centre of the specimen if a/R is zero until the onset of necking and is thereafter assumed to increase linearly with strain in accord with the experiments of Bridgman (1952) (fig.8.2).

8.1.3. UNNOTCHED PLANE STRAIN SPECIMENS.

An analytic solution is available for the unnotched specimen geometry shown in fig.7.4. In such a specimen, plane strain deformation occurs with respect to the z-axis while the assumption of plane stress with respect to the x-axis is reasonable until necking occurs. With the axes in fig.7.4:

$$e_z = e^p_z = C\,(\sigma_z - (\sigma_x + \sigma_y)/2) = 0$$

where C is a constant. Hence:

$$\sigma_m = \sigma_z = \sigma_x/2$$

and

$$\Rightarrow \bar{\sigma} = (\sqrt{3}/2)\sigma_x$$

The Prandtl-Reuss equations give the plastic strain components and in particular:

$$e^p_x = (3/2)\bar{e}^p(s_x/\bar{\sigma})$$

where s_x is the deviatoric stress component in the x direction. It follows that:

$$e^p_x = (\sqrt{3}/2)\bar{e}^p \qquad \text{(equ.8.1)}$$

and:

$$e^p_y = -(\sqrt{3}/2)\bar{e}^p \qquad \text{(equ.8.2).}$$

The effective stress and effective plastic strain are related through the uniaxial stress-strain curves in fig.7.2.

8.1.4. NOTCHED PLANE STRAIN SPECIMENS.

A numerical analysis of a plane strain notched specimen with the profile shown in fig.7.4 has been performed by Hancock and Brown (1983) using the program described in appendix A.1.1. With the axis system defined in fig.7.4, a significant result of this analysis is that:

$$(\sigma_x + \sigma_y)/\bar{\sigma} = 2.2$$

over a wide range of deformation. In plane strain then:

$$\sigma_x/\bar{\sigma} = 1.1 + (1/\sqrt{3})$$

$$\sigma_y/\bar{\sigma} = 1.1 - (1/\sqrt{3})$$

$$\sigma_z/\bar{\sigma} = 1.1.$$

8.2. VOID GROWTH IN UNIAXIAL TENSILE SPECIMENS.

In the light of the appropriate numerical or analytic field analyses, the void growth equations of Rice and Tracey (1969) or McClintock (1968) may be applied to deforming tensile specimens. For the calculation of void growth in such cases it is desirable that the equations be expressed in terms of non-directional parameters such as the mean and effective stresses, as is the case with the equations of Rice and Tracey (1969). However, recognising that local field variables relative to the complete specimen may be regarded as remote with respect to an individual void, McClintock's (1968) equations (equs.2.13) take the form:

$$\ln(R/R_0) = (\sqrt{3}/2)(\bar{e}^p/(1-n))$$
$$\sinh((\sqrt{3}/2)(1-n)(\sigma_a+\sigma_b)/\bar{\sigma})+(1/2)(e_a+e_b)$$

$$M = (\sigma_a-\sigma_b)/(\sigma_a+\sigma_b)$$
$$+ (M_0-(\sigma_a-\sigma_b)/(\sigma_a+\sigma_b))$$
$$\exp(-\sqrt{3}(\bar{e}^p/(1-n))\sinh(\sqrt{3}/2)(1-n)(\sigma_a+\sigma_b)/\bar{\sigma}))$$

which require the evaluation of the individual components of the bi-axial stress system. For the particular cases of axisymmetric and plane strain geometries however, these may be reduced to a form in which only non-directional parameters appear. This is faciliated by the introduction of a number of intermediate variables. Defining:

$$K = (\sigma_a + \sigma_b)/\bar{\sigma} \qquad \text{(equs.8.3)}$$

$$K' = (\sigma_a - \sigma_b)/(\sigma_a + \sigma_b)$$

$$L = \sqrt{3}\bar{e}^p/(1-n)$$

$$L' = (1/2)(e_a + e_b)$$

and:

$$J = \sinh((\sqrt{3}/2)(1-n)K)$$

allows equs.2.13 to be written as:

$$\Rightarrow R = R_0\exp((1/2)LJ + L') \qquad \text{(equs.8.4)}$$

and:

$$M = K' + (M_0 - K')\exp(-LJ)$$

These may be evaluated numerically to get the final shape of a void after a given amount of deformation. The strain $\bar{e}^p$ in equs.8.3 is identified in numerical solutions with the strain increment $d\bar{e}^p$ imposed at the current stress point. The current rate of growth of R and M at the current stress point may be obtained from equs.8.4 in the form of the differentials:

$$dR = R\,((1/2)LJ + L')$$

$$dM = LJ(K' - M).$$

From final values of R and M, the major and minor axes, a and b, of the ellipse are easily found by solving equ.2.10 and equ.2.11 to get:

$$a = R\,(1 + M)$$

$$b = R\,(1 - M).$$

8.2.1. AXISYMMETRIC SPECIMENS.

For an axisymmetric specimen cylindrical polar coordinates are appropriate and finite element analysis shows that:

$$e_{\theta\theta} = e_{rr}$$

and with the requirement of constant volume deformation then:

$$e_{\theta\theta} = e_{rr} = -(1/2)e_{zz}$$

Symmetry implies that there are no shear stresses in uniaxial tension and that the r,θ,z directions are principal directions. Dropping the double suffix for convenience, the effective strain defined in section 3.1 may be inserted to give:

$$e_r = e_\theta = -(1/2)\bar{e}^p$$

and

$$e_z = \bar{e}^p.$$

To determine the stresses, these equations may be used in the Prandtl-Reuss equation for the axisymmetric case, leading to:

$$\sigma_r = \sigma_\theta = \sigma_m - (1/3)\bar{\sigma} \qquad \text{(equs.8.5)}$$

and:

$$\sigma_z = \sigma_m + (2/3)\bar{\sigma}$$

Elliptical voids grow in the deforming specimens such that the major axis is coincident with the local maximum principal strain. The axial and radial directions of an axisymmetric specimen may then be identified with the major and minor axes in the McClintock (1968) void growth equations (equs.2.13) such that:

$$\sigma_z = \sigma_a \quad \text{and} \quad \sigma_r = \sigma_b$$

in which case equs.2.13 become:

$$\ln(R/R_0) = (\sqrt{3}/2)(\bar{e}^p/(1-n))$$
$$\sinh((\sqrt{3}/2)(1-n)((\sigma_z+\sigma_r)/\bar{\sigma})+(1/2)(e_z+e_r)$$

(equs.8.6)

$$M = (\sigma_z-\sigma_r)/(\sigma_z+\sigma_r)$$
$$+ (M_0-(\sigma_z-\sigma_r)/(\sigma_z+\sigma_r))$$
$$\exp(-\sqrt{3}(\bar{e}^p/(1-n))\sinh(\sqrt{3}/2)(1-n)(\sigma_z+\sigma_r)/\bar{\sigma}))$$

The groupings of stress components in equs.8.6 may be evaluated in terms of the mean and effective stress from the particular relations derived for axisymmetric specimens, making use of the intermediate variables of equs.8.3. With equs.8.5, K takes the form:

$$K = 2(\sigma_m/\bar{\sigma}) + (1/3).$$

while K' reduces from to:

$$K' = (1/K).$$

The strain terms in equs.8.4 may be expressed in terms of the effective strain as:

$$L' = (1/4)\bar{e}^p.$$

and with L and J the void growth equations in the form of equs.8.4 may be evaluated numerically.

8.2.2. UNNOTCHED PLANE STRAIN SPECIMENS.

Fig.7.4 defines the geometry of an unnotched plane strain specimen and if this specimen is viewed along the plane strain (z)

axis, the minor axis of an elliptical void will be parallel to the y axis while the major axis remains parallel to the x axis as before. In this case, plane strain conditions reduce K and K' to:

$$K = (\sigma_x + \sigma_y)/\bar{\sigma} = 2/\sqrt{3}$$

and

$$K' = (\sigma_x - \sigma_y)/(\sigma_x + \sigma_y) = 1$$

while

$$L' \simeq 0.$$

The general form of L (equ.8.3) is isotropic and may be used directly for any particular specimen geometry, given the remote effective plastic strain. Thus completes the information needed to solve the void growth equations of equs.8.4.

If the specimen is now viewed along the plane stress y-axis then the minor axis of an elliptical void will be parallel to the z-axis while the major axis remains parallel to the x-axis. In this case, equs.8.3 give:

$$K = (\sigma_x + \sigma_z)/\bar{\sigma}$$

which reduces in plane strain to:

$$K = \sqrt{3}.$$

Similarly, K' viewed in the appropriate direction reduces to:

$$K' = (\sigma_x - \sigma_z)/(\sigma_x + \sigma_z)$$

$$\Rightarrow K' = (1/3)$$

while:

$$L' = (\sqrt{3}/4)\bar{e}^{p}.$$

With the value of L as before, the void growth equations (equ.8.4) again be evaluated.

A feature of this analysis is that transverse stress terms parallel to the minor axis of the void only appear in the growth equations for the case in which the specimen is viewed along the plane stress axis. An artifact of the analysis is thus an increase in the triaxiality of the stress state as seen from this viewpoint. The predicted void growth rates for such specimens will therefore depend literally on the chosen point of view.

8.2.3. NOTCHED PLANE STRAIN SPECIMENS.

Viewing the specimen along the plane strain z axis, K in equs.8.3 takes the value:

$$K = (\sigma_x + \sigma_y)/\bar{\sigma} = 2.2$$

in accord with the finite element analysis of Hancock and Brown (1983) while:

$$K' = (\sigma_x - \sigma_y)/(\sigma_x + \sigma_y) = 0.525.$$

Again L requires no substitution of specific components while L' becomes:

$$L' = (1/2)(e_x + e_y) = 0.$$

Looking along the y-axis now, K takes the form:

$$K = (\sigma_x + \sigma_z)/\bar{\sigma}$$

and with the results from Hancock and Brown's (1983) analysis, then:

$$K = 2.2 + 1/\sqrt{3} = 2.777.$$

Similarly, K' becomes:

$$K' = (\sigma_x - \sigma_z)/(\sigma_x + \sigma_z) = 0.208.$$

In plane strain, the strain term is:

$$L' = (\sqrt{3}/4)\bar{e}^p.$$

and again there is a difference in the void growth rates, depending on the directions identified with the a and b directions of McClintock's (1968) analysis.

Obviously, differences in the void growth rates with respect to the two different viewpoints in both plane strain specimens are not a feature of the void growth in real specimens, nor are they a feature of the Rice and Tracey (1969) void growth equations. In spite of such disadvantages however, McClintock's (1968) equations probably give the best estimate of the change in void shapes during large deformations. For this reason, the analysis based on McClintock's (1968) equations is preferred in the current work.

9. RESULTS.

The development of an inclusion-free void depends on the local stress state with the aspect ratio a/b increasing rapidly under uniaxial tension. In the early stages of deformation it was found that the presence of an inclusion effectively pinned the minor diameter but experiments on simple model systems indicated that this restriction had little effect on the growth of the major diameter and the applicability of the void growth equations. These experiments involved applying a uniaxial tensile load to a sheet of rubber in which an circular hole was cut in the unloaded state. As the load was applied, the shape of the elliptical hole was monitored as shown in fig. 9.1. The experiment was repeated with the pinning effect of an inclusion provided by a perspex cylinder of the same diameter inserted in the hole. As shown in fig.9.1, the rate of growth of the model void was substantially unchanged by the presence of the inclusion.

While the extrapolation of the results from this model system to inclusions in deforming metal matrices is by no means obvious, the same conclusion was ultimately reached by numerical analyses in which the minor diameter of the voids could be pinned at the initial value while the major diameter was allowed to grow in the deforming matrix.

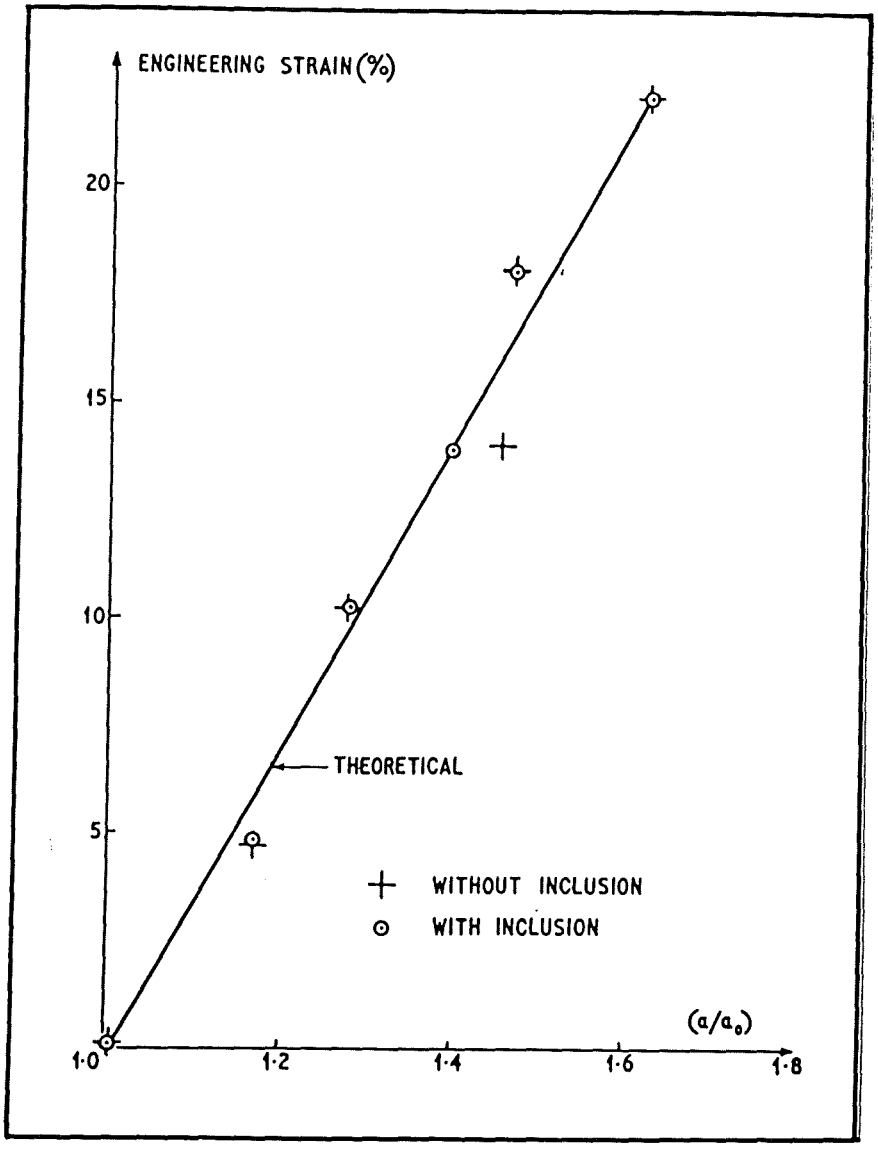

Fig.9.1. The growth of the major axis of an initially circular hole in a rubber sheet subject to uniaxial tension, both with and without a perspex 'inclusion' in situ.

The development of the mean radius and eccentricity of a void during an increment of plastic strain $d\bar{e}^p$ may be calculated from equs.8.4. By tracking the growth of R and M incrementally through each individual void deformation history, it was possible to determine the strain at which nucleation must have occurred in order that subsequent void growth would result in voids of the actual dimensions ob-

served at the end of each test. This numerical procedure is described in appendix A.2. The corresponding local flow stress at nucleation follows from the stress-strain law and the local triaxiality as determined from the appropriate local deformation history.

The stress-strain law used in the development of McClintock's (1968) void growth equations is a power law of the type (equ.2.14):

$$\bar{\sigma} = \sigma_0(\bar{e}^p)^n$$

which may be contrasted with the power law used in the finite element analyses (equ.4.1). Here $\bar{\sigma}$ and $\bar{e}^p$ have their usual meanings but n and σ_0 are curve fitting parameters. The best fit to the experimental stress-strain curve was obtained with n = 0.255 and σ_0 = 0.515 (fig.7.3).

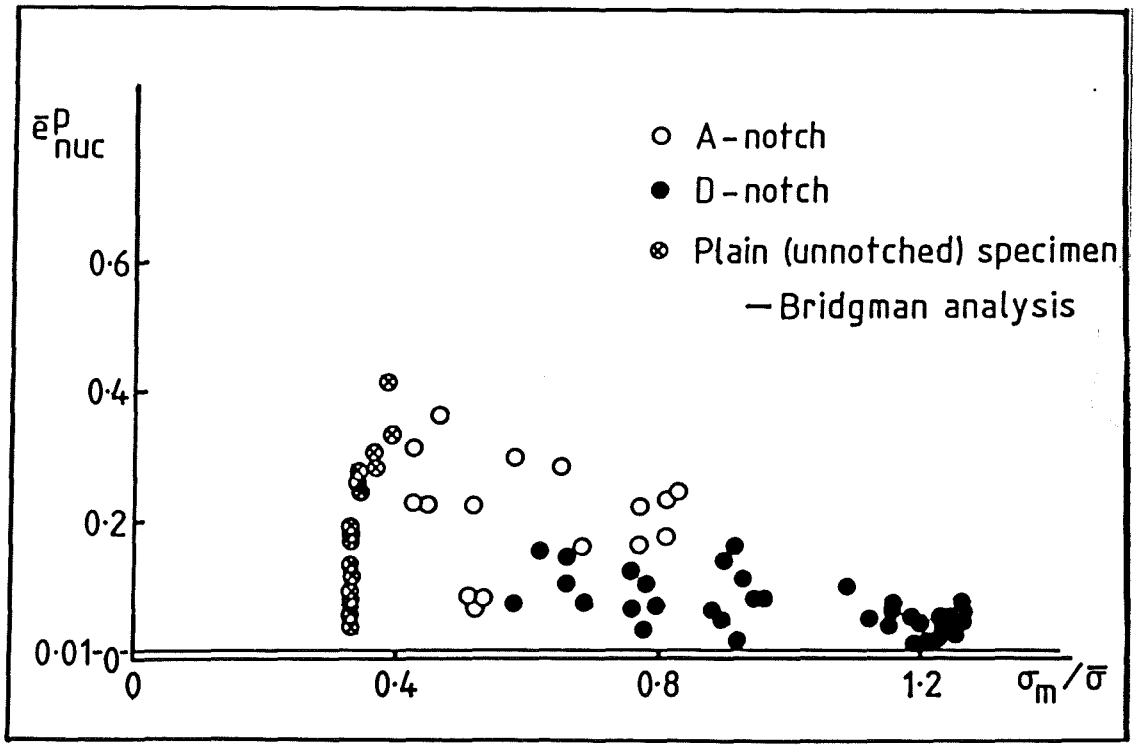

Fig.9.2. The distribution of nucleation strains e_{nuc} for the void sample, plotted against triaxiality.

For the nucleation analysis, it was considered important to model correctly both the elastic properties and the rate of strain hardening in order to predict the true maximum radial stress around the interface, but neither form of power law can adequately reflect both these aspects of the material behaviour. A piecewise linear approximation to the stress-strain curve in fig.4.2 was therefore derived for use in the finite element model of an oxide inclusion in a Swedish Iron matrix. Figure 9.2 shows the equivalent plastic strain required to nucleate each of 159 measured voids is shown as a function of the instantaneous local stress state parameter $\sigma_m/\bar{\sigma}$, which the inclusions nevertheless see as a remote field.

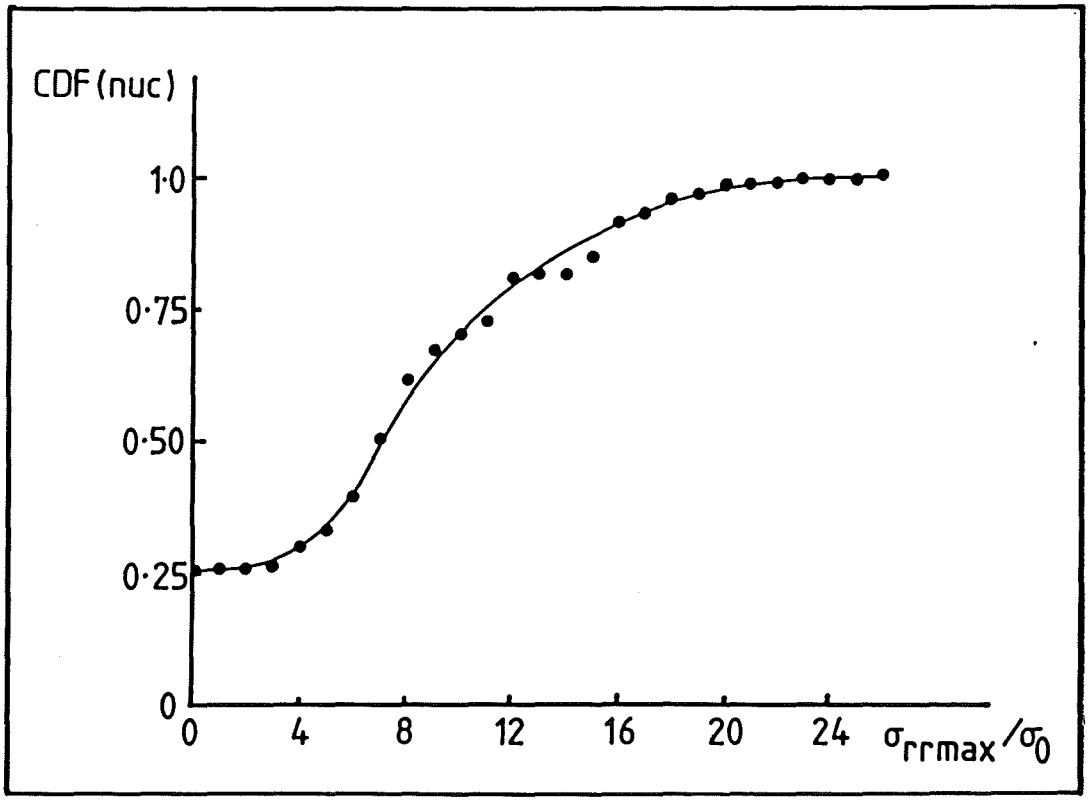

Fig.9.3. The cumulative distribution of the probability of nucleation at any maximum interfacial radial stress σ_{rrmax} around the inclusion.

From the stress and strain conditions at nucleation and the numerical solution for the maximum interfacial radial stress as a function of the deformation, it is possible to determine the maximum interfacial radial stress at nucleation. Figure 9.3 shows the distribution of interfacial strength in the form of a cumulative distribution function (CDF) from which the probability of nucleation at any value of the interfacial radial stress may be inferred. This leads to the bi-modal probability distribution in fig.9.4.

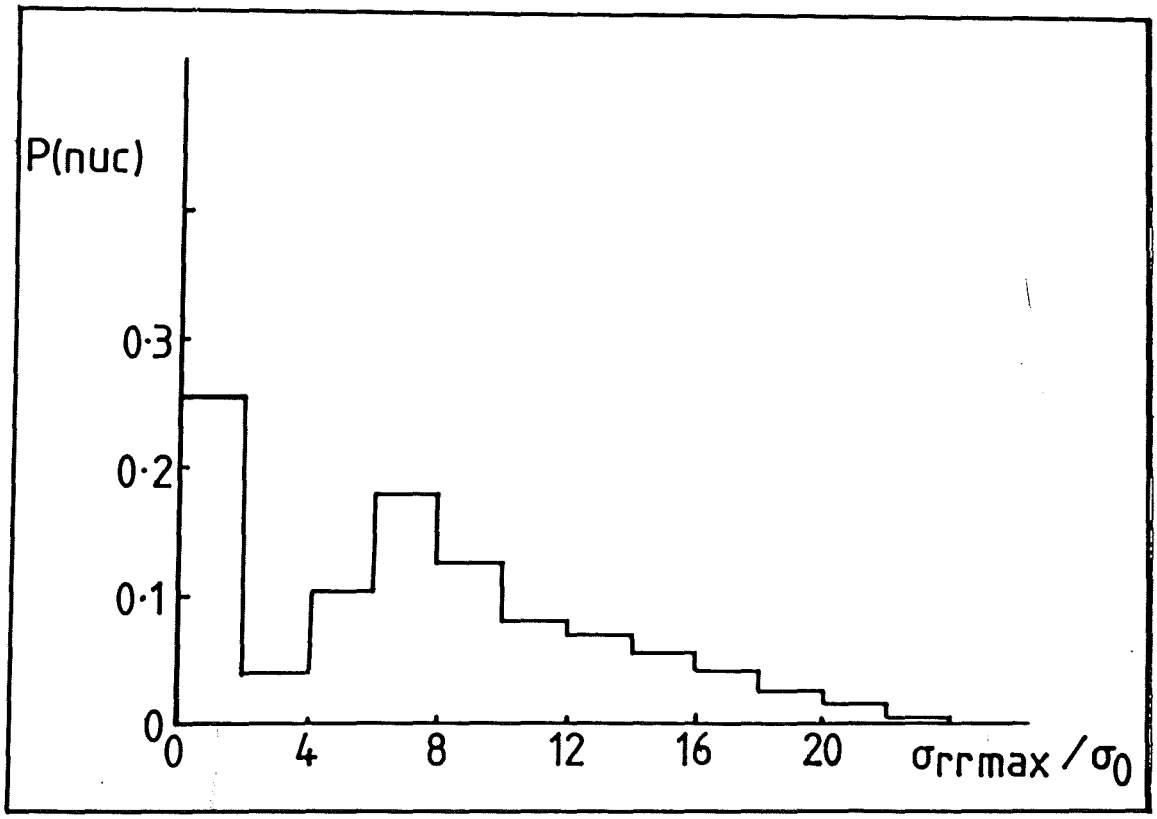

Fig.9.4. The probability of nucleation P(nuc) as a histogram with respect to the maximum interfacial radial stress σ_{rrmax} around an inclusion.

10. DISCUSSION.

10.1. THE LOCAL PLASTIC STRAIN.

It is apparent from this analysis of a significant population of voids nucleated in a range of triaxial stress states that there is no critical value at which nucleation occurs but there is a tendency for nucleation strain to decrease with increasing triaxiality. The scatter in fig.9.2 implies that nucleation is a statistical process and many of the voids are nucleated at plastic strains of less than 1%, the limit of the numerical analysis. That the statistical basis of nucleation is a real phenomenon and not an artifact of the numerical routines is illustrated by fig.7.6 which shows the variation in the size of neighbouring voids subject to essentially identical deformation histories. In extreme cases the interface may be substantially stronger on one side of the particle, leading to nucleation on the other side only.

10.2. THE MAXIMUM INTERFACIAL RADIAL STRESS.

From fig.9.4 it is apparent that there are two distinct populations of particles, one of which shows little interfacial strength while the other represents particles well bonded to the matrix. It is reasonable to assume that the first peak, corresponding to voids nucleated at less than 1% plastic strain (approximately 25% of the total population), have interfaces with no strength at the start of testing and behave as pre-existing voids. Pre-existing voids will usually exist in laboratory specimens, perhaps as result of prior deformation of the material from which the specimen was machined, but these can

give no indication of the nature of the local conditions leading to nucleation.

The second peak, representing inclusions bonded to the matrix at the start of the tests, shows clearly the statistical nature of the interfacial strengths even for well-bonded particles. These results are consistent with a nucleation criterion based on a maximum interfacial radial stress, with the modal value of the nucleation probability distribution at $7\sigma_0$ and a few particles approaching the theoretical cohesive strength of the interface at about $20\sigma_0$. A physical basis to this distribution of interfacial strength can be given in terms of flaws in the particle/matrix interface, comprising areas of the interface which are less well bonded to the matrix. The statistical strength of the interface is then naturally related to the distribution of such flaws and the process by which they lead to failure of the particle/matrix interface. It also seems reasonable to suppose that the strength of the interface is related to the physical mechanism of decohesion, in this case the separation of a plastic matrix from an elastic particle. If the same radial stress was reached with an elastic matrix, it is unlikely that the mechanism of decohesion would be the same and hence that the interfacial strength would correspond to that measured with a plastic matrix. Experiments described in the next chapter, with highly constrained specimens which develop high stresses in elastic strain fields, are inconclusive and so the results do not preclude a two-parameter criterion in which nucleation strain decreases with increasing triaxiality.

11. NUCLEATION IN ELASTIC STRAIN FIELDS.

The nucleation of voids at second phase particles has been seen to be best described in terms of a probabilistic criterion based on the maximum interfacial radial stress around the inclusion/matrix interface. However the numerical analysis relates to experiments in which the stress state was varied but in which the material was always subject to gross plastic deformation. By definition, ductile failure is accompanied by large plastic strains but the analysis as presented begs the question of whether nucleation may be described in terms of a single stress parameter alone, which implies that voids nucleate at the appropriate stress level irrespective of all other local fields. Strictly therefore, the nucleation criterion in chapter 10 should be regarded as necessary rather than sufficient.

To investigate the sufficiency of the nucleation criterion an attempt was made to reproduce the high interfacial radial stresses necessary for nucleation in the absence of any plastic strain. Such conditions exist in the centre of deep, double-edged crack specimens, in which the constraint due to a fully developed Prandtl field produces high elastic stresses but delays yielding. Such a specimen was loaded until the interfacial stresses were sufficient to trigger substantial nucleation. On unloading, the cracks were machined away to leave a simple uniaxial tensile specimen which was subsequently loaded until the initiation of failure. Within experimental limits, this specimen failed at a strain equal to that of the plain tensile specimen shown on the failure locus of fig.7.5, from which it is inferred that void nucleation occurred under similar conditions in both cases.

This result tends to imply that the initial prestressing had no influence and that void nucleation does not occur in elastic stress fields but requires some undetermined amount of plastic strain. However, the analysis of void nucleation showed that a large proportion (approximately 25%) of the inclusion population was not well-bonded to the matrix for Swedish Iron in the as-received condition. A numerical simulation of the total void growth to failure, described fully in the following chapters, indicates that the amount of nucleation available from purely elastic deformation inside the deep, double-edged crack will increase this proportion, but that the potential increase is not sufficient to significantly affect the ductility. In consequence, the possibility of nucleation in elastic stress fields remains unresolved.

PART 4: FAILURE INITIATION.

12. ANALYSIS.

12.1. METALLOGRAPHIC ANALYSIS.

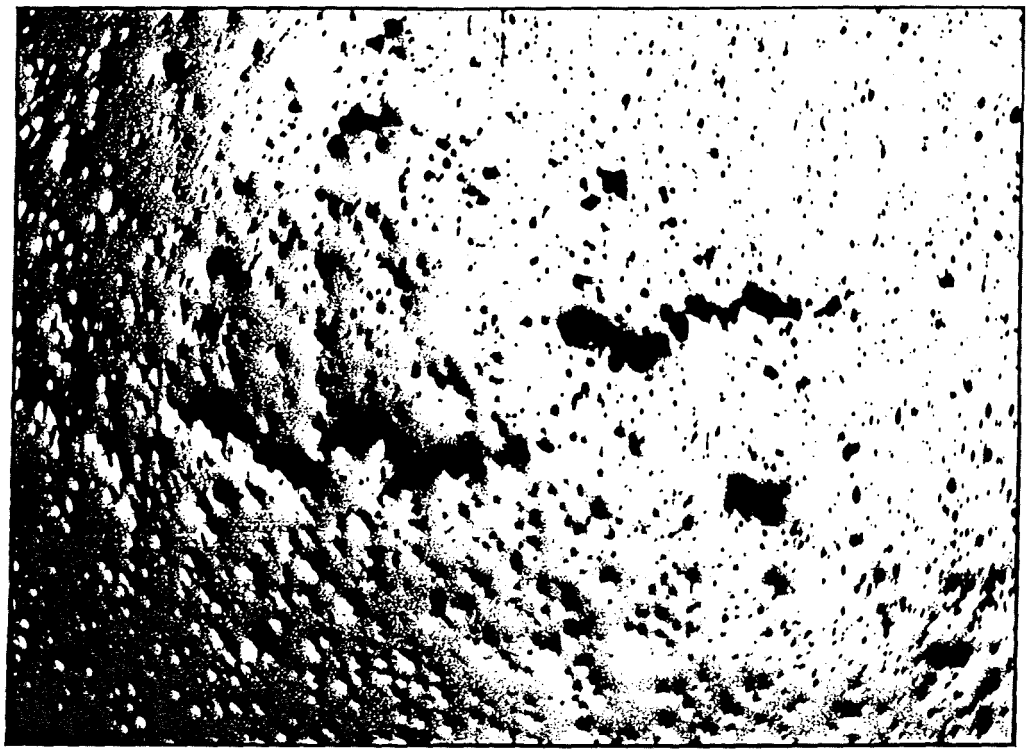

Fig.12.1. The propagation of an internal crack in an axisymmetric specimen in a direction macroscopically normal to the principal loading direction.

The deformation histories which result in failure initiation for different specimen geometries are shown in fig.7.5, and the locus drawn through the final points has been termed a failure locus. This shows the decrease in ductility associated with increasing triaxiality and implies a correlation of failure with stress state, independent of the state of strain. For all the notched specimens and the naturally

necking axisymmetric specimen, failure initiates internally at the centre of the minimum cross section and proceeds in a direction macroscopically normal to the applied tensile load (fig.12.1).

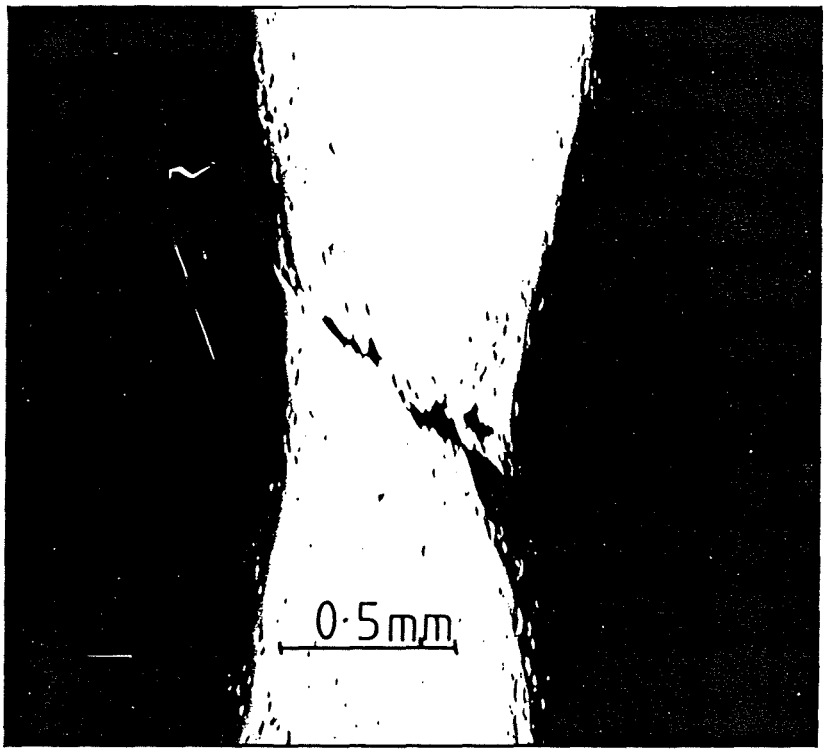

Fig.12.2. The propagation of an internal crack in a plane strain specimen along a shear band.

For the unnotched plane strain specimen, failure starts at a free surface and tends to proceed by void coalescence on an inclined plane as shown in fig.12.2. However, since ductile failure depends on the deformation history, the failure locus only applies to deformations with relatively small changes in triaxiality, as is the case with the particular notch geometries chosen: attempts to produce radically different deformation histories are described later.

12.2. NUMERICAL ANALYSIS.

The data in fig.9.4 can be expressed numerically as the fraction of the total void population nucleated in any increment of remote strain, while deformation histories for the failure initiation site of each specimen can be produced by restarting the finite element analyses of each notch specimen from the last increment of applied displacement and extending this up to and beyond the observed ductility. Applying the void growth equations of McClintock (1968) to each individual fraction of the void population, the average porosity due to the growth of the whole population may be determined for every increment of strain up to the initiation of failure. Details of this numerical process are contained in appendix A.3.

It has been suggested earlier that the hardening rate of the matrix is of crucial importance to the initiation of failure. Both triaxiality and the porosity affect the hardening rate of the porous aggregate and this can be calculated directly from a finite element analysis of a dilating material with predefined initial porosities. Solutions for notched bars of such material have been obtained by Brown, Hancock, Thomson and Parks (1980) who found that the hydrostatic and deviatoric components of the stress tensor were reduced such that their ratio remains approximately constant and close to that for the plastically incompressible solution (equ.2.11). This simplification has been used together with the current void volume fraction calculated from the discrete void growth equations to estimate the hardening rates for a range of initial porosities without the need to perform full-field dilating finite element analyses for each case.

13. RESULTS.

The average porosities f of the material at void coalescence are shown in fig.13.1, from which it is apparent that failure occurs when the volume fraction has increased by a factor of about 4 on the initial value of 1%. However, while such a figure may be used as an empirical failure criterion, it offers no insight into the failure process. A feature of fig.13.1 is that specimens with higher triaxialities require slightly less void growth to produce failure.

Specimen	e^p_{ave}	e^p_{loc}	f
PL-A	0.37	0.37	0.025
AX-D	0.48	0.29	0.026
AX-A	0.56	0.50	0.033
PL-P	0.79	0.70	0.037
AX-P	1.05	1.05	0.052

Fig.13.1. The conditions at failure in Swedish Iron. The average effective plastic strain over the cross-section is denoted $\bar{e}^p_{ave}$, while $\bar{e}^p_{loc}$ is the local value in the specimen centre.

Figure 13.2 shows the results of the calculation of the hardening rate of the average material at failure. The essential feature of fig.13.2 is that these rates are significantly positive and again while they may be used as an empirical failure criterion, they cannot elucidate the physics of the failure process itself.

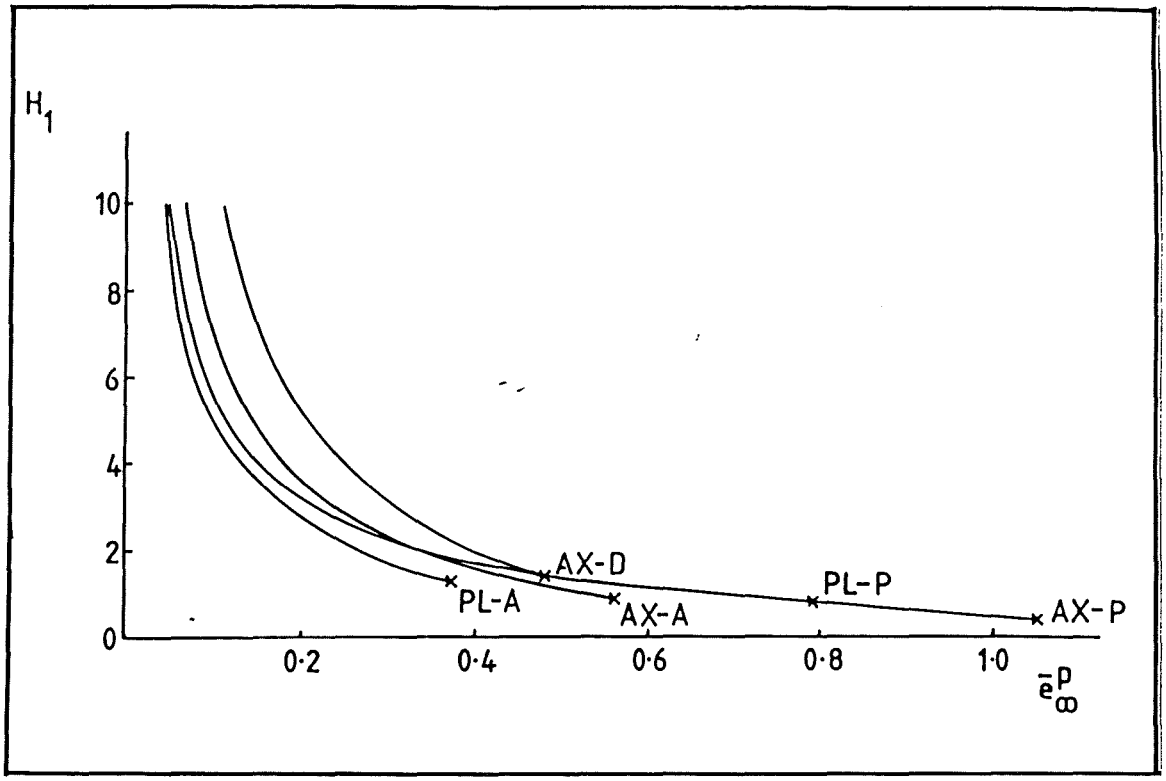

Fig.13.2. The variation of the hardening rate $H_1 = (1/\sigma_0)(d\bar{Z}/d\bar{e}^p)$ of the average porous material with deformation.

14. DISCUSSION.

14.1. THE AVERAGE AGGREGATE MATERIAL.

The results of the void growth calculations show porosities of about 3.8 ± 1.4 % at failure in Swedish Iron, a growth factor of about 4 on the original 1 %. However, the fundamental reason for the inability of a criterion on this or the corresponding aggregate hardening rate or indeed any property of the average material to explain the physics of failure is that the microstructure of most real materials is a random spatial distibution of inclusions, which results in variations in local volume fractions and in extreme cases produces clusters of inclusions as in fig.14.1. Failure will then initiate in regions of inclusion concentration long before failure of the average material is imminent. To investigate the likely porosities in such regions it is necessary to develop the statistics of the inclusion distribution.

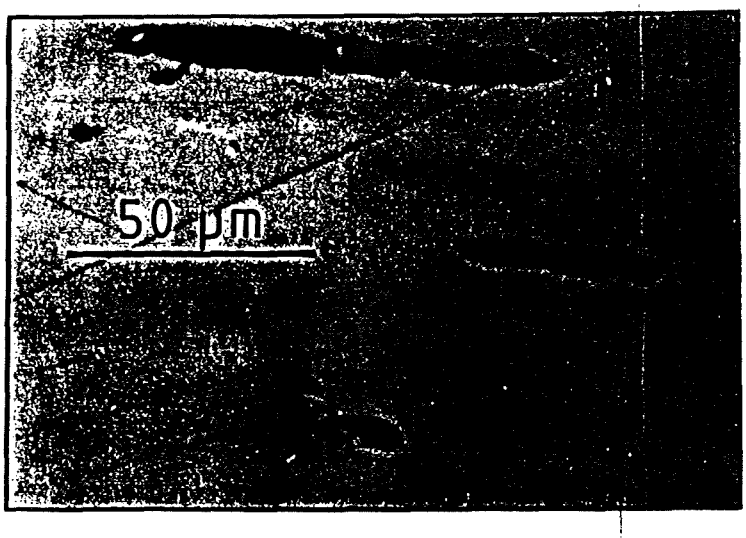

Fig.14.1. The extreme case of an inclusion cluster resulting from the random spatial distribution of inclusions.

14.2. THE STATISTICS OF VOID DISTRIBUTIONS.

The volume $\delta V_{\bar{x}}$ is defined as that volume of aggregate material which contains $\bar{x}$ inclusions of a uniformly distributed population. The volume δV_1 is then the volume of a unit cell containing on average a single inclusion and in general:

$$\delta V_{\bar{x}} = \delta V_1 \bar{x} \qquad \text{(equs.14.1)}$$

with:

$$\delta V_1 = (4/3)\pi r^3/f_0$$

where r is the average inclusion radius and f_0 is the initial void volume fraction. The probability P(x) that any cell of volume $\delta V_{\bar{x}}$, selected at random, will contain x inclusions is given by the Poisson distribution:

$$P(x) = (\bar{x}^{(x-1)})/(e^{\bar{x}}(x-1)!) \qquad \text{(equ.14.2)}$$

and the probability $P(\geq x)$ that this cell contains x or more inclusions is found by the summation:

$$P(\geq x) = \Sigma_{n=x}^{\infty} P(n).$$

$$P(\geq x) = \Sigma_{n=x}^{\infty} ((\bar{x}^{(n-1)})/(e^{\bar{x}}(n-1)!))$$

The probability $P(<x)$ that the volume $\delta V_{\bar{x}}$ contains less than x inclusions is then:

$$P(<x) = 1 - P(\geq x)$$

$$P(<x) = 1 - \Sigma_{n=x}^{\infty} ((\bar{x}^{(n-1)})/e^{\bar{x}}(n-1)!)).$$

A volume V of aggregate will contain $(V/\delta V_{\bar{x}})$ cells and the probability $P'(<x)$ that every cell in V contains less than x inclusions is:

$$P'(<x) = 1 - (P(<x))^{(V/\delta V_{\bar{x}})}$$

$$\Rightarrow P'(<x) = (1 - \Sigma_{n=x}^{\infty}((\bar{x}^{(n-1)})/e^{\bar{x}}(n-1)!)))^{(V/\delta V_{\bar{x}})}$$

Finally, the probability $P^*(<x)$ that at least one cell in V contains x or more inclusions is simply:

$$P^*(<x) = 1 - P'(<x)$$

$$\Rightarrow P^*(\geq x) = 1 - (1 - \Sigma_{n=x}^{\infty}((\bar{x}^{(n-1)})/e^{\bar{x}}(n-1)!)))^{(V/\delta V_{\bar{x}})}$$

(equ.14.3)

14.3. FAILURE IN MATERIALS WITH A STATISTICAL DISTRIBUTION OF INCLUSIONS.

Since failure invariably initiates near the centre of axi-symmetric specimens of Swedish Iron, attention may be focussed on a small volume V = 10 mm^3 extending just over 1 mm in each direction from the centre. With an average inclusion diameter of 5 μm and an initial porosity of 1%, equs.14.1 imply that the volume V contains 1.5×10^6 unit cells. Equation 14.3 then implies an 82% probability that at least one unit cell in V will have an inclusion concentration factor of 10 or more. The mechanical behaviour of such regions is considered in detail in Part 5: here it is appropriate to note that such inhomogeneities are kinematically constrained by the surrounding material and the ratio of the dilation rate within the patch to that in the remote region is approximately constant and equal to the void volume fraction. This allows the local hardening rate:

$$H_i = (1/\sigma_0)(d\bar{Z}/d\bar{e}^p) \qquad \text{(equ.14.4)}$$

in an inhomogeneity with an inclusion concentration i to be estimated. It is interesting to note that if homogeneous flow were to continue up to the observed failure strain of the material, the hardening rate H_{10} of a cell with a tenfold increase in inclusion density would be strongly negative at the observed ductilities (fig.14.2). If failure on a macroscopic scale is identified with failure of such cells then the Rudnicki and Rice (1975) model will significantly underestimate the ductility of the material.

At a microscopic level, failure initiation cannot depend on

the stress and strain at a point but must involve a characteristic length or volume related to the microstructure. This has generally been identified as the average inclusion spacing, ie the unit cell size, but the characteristic of a crack-like defect is that it must produce stress and strain concentrations which act over distances comparable to the average particle spacing. Failure over a distance equal to the average particle spacing will only perturb the local stress and strain fields over distances of the order of half the average particle spacing and void coalescence on such a scale seems insufficient to produce a defect which behaves in a crack-like manner. For isotropic failure of a volume of material, the radius of the failed volume must equal the interparticle spacing and if for simplicity this volume is divided into cubic cells, failure will involve 8 adjacent unit cells. Void coalescence over such a size scale then produces a defect which begins to behave as a crack in the usual sense in the continuing deformation field rather than as a large irregular void. Partitioning the material into volumes containing 8 inclusions on average, equ.14.3 with $\bar{x} = 8$ implies a 50% probability that at least one cell will contain 25 particles, an inclusion density of about 3 times the average. For such a cell the local hardening rate H_3 is of order zero at observed ductilities and the material will be close to localisation on the basis of a Rudnicki and Rice (1975) analysis (fig.14.2). Such analysis does admit the possibility of failure at small non-zero hardening rates but it does not seem fruitful to discuss such deviations in view of the problem of determining the size scale over which the analysis is to be applied. On a macroscopic scale, the average hardening rates at failure are positive while on the scale of a unit cell local hardening rates can be strongly negative. The statistical distribution of the porosity therefore implies

a hardening rate which depends on the size scale over which it is measured.

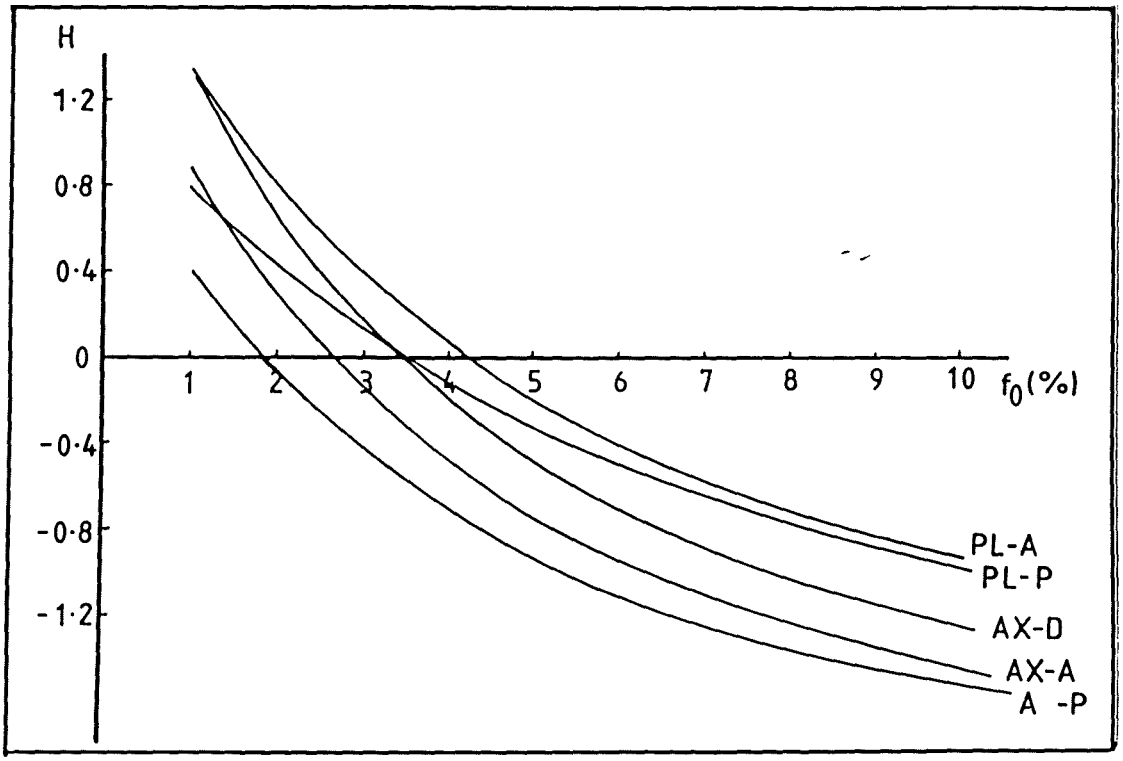

Fig.14.2. The hardening rate at failure for different values of the initial porosity f_0. At f_0=1%, representing the average material, the hardening rate at failure is positive. At f_0=10%, representing a likely inhomogeneity, the hardening rate at failure is negative.

15. FAILURE FOLLOWING COMPLEX LOADING HISTORIES.

It has been noted that the failure locus in fig.7.5 is only valid for deformation paths in which the triaxiality does not change appreciably, which raises the question of how the damage is accumulated in material subject to load paths in which the stress state varies significantly. An attempt was made to determine the residual ductility under such conditions by subjecting a plain tensile specimen of Swedish Iron to a uniaxial tensile load, for which the triaxiality $\sigma_m/\bar{\sigma} = 1/3$. The test was interrupted at a strain of 70% and an A-notch (fig.7.3) was machined on the deformed specimen before deformation was continued. The effect of the notch is to produce a step change in the triaxiality and for this particular case immediately moves the specimen outside the failure locus in fig.7.5. When the pre-deformed specimen was reloaded, fracture did in fact occur with very little additional strain but on inspection of the fracture surface it was found that failure had occurred by a cleavage mode to which the present analysis is not applicable.

PART 5: THE STRESS AND STRAIN FIELDS NEAR CONTAINED INHOMOGENEITIES IN A DEFORMING MATRIX.

16. THE ANALYSIS OF AN EQUIAXED INHOMOGENEITY.

In order to investigate the effect of non-uniformity in the distribution of voids on the ductility of the aggregate material, it is convenient to represent the average material as a porous plastic continuum rather than consider discrete voids. Statistical inhomogeneities may then be represented in the form of regions of locally increased porosity. However, the macroscopic limit of ductility is largely dependent on the approach to zero of the local hardening rates within and near such inhomogeneities and for strain hardening materials the critical state of near-zero hardening rates is only reached with large remote deformations. Such a situation will be approached in a finite element analysis after a large number of small remote displacements, with a strong possibility of significant rounding errors or after a smaller number of larger increments, for which it is difficult to maintain the stress point on the current yield surface and ensure normality of the deformation. In preference to either of these, the behaviour of hardening materials at large remote deformations was addressed by specifying an aggregate material with a perfectly-plastic matrix, for which the hardening rate of the aggregate will be negative throughout the deformation history, particularly in the highly porous patch.

The analysis of a patch of porous material embedded within average porous surroundings was performed using the finite element program described in appendix A.1.1 with dilating porous elements de-

veloped by Parks (unpublished). The porous aggregate was represented by Gurson's (1977) yield function as amended by Tvergaard (1981) (equ.3.8):

$$\phi = (\bar{Z}/\bar{\sigma})^2 + 3f \cosh((3/2)(Z_m/\bar{\sigma})) - (1+2.25f^2).$$

For an isotropic dilating material, the plastic strain components are obtained from the associated flow rule (equ.3.8):

$$dE^p_{ij} = d\Lambda \, (\partial\phi/\partial Z_{ij})$$

in which the pressure dependence exactly matches the dilation rate (Rudnicki and Rice (1975)). This can be written for the Tvergaard (1981) yield surface as:

$$\partial E_{kk}/\partial\bar{E}^p = 2.25f\sinh(Z_{kk}/(2\bar{\sigma}))/(\bar{Z}/\bar{\sigma})$$

To study the effect of the strain softening which results from large deformation of a porous aggregate strain, the matrix was represented by the perfectly plastic Von Mises yield surface of equ.3.3:

$$\phi = (\bar{\sigma}/\sigma_0) - 1 = 0$$

which may be regarded as a special case of the porous yield surface of equ.3.7 with g = 1. Plastic strain components for the matrix are determined from the associated flow rule for a Von Mises yield function, the Prandtl-Reuss relation of equ.3.6. An elastic modulus E of 210 GPa and an initial remote yield stress σ_0 in uniaxial tension of 0.14 GPa were chosen to model the response of Swedish Iron, the low-

yield material used in the experimental work previously described.

An inhomogeneity with locally reduced particle spacing was embedded within a field of average material by the finite element grid of fig.4.1, in which the 50 elements in the 5 innermost rings were given porosities greater than the average value of 1% assigned to the remaining elements. Initial porosities of 11 % were specified in the 10 elements in the innermost ring with 10 % in the 40 elements in the next 4 adjacent rings in accord with the likely case discussed in section 13.3. This ensured that yielding initiated at the centre of the bad patch and that conditions at the centre were not dominated by the proximity of a sharp interface with the less porous environment.

The remote boundary was set at a distance of 6 times the radius of the inhomogeneity and boundary nodes were constrained such that no displacement occurred normal to the axes of symmetry. Axisymmetric solutions were obtained under uniaxial tension for porous imperfections in both porous and non-porous environments. The influence of an imperfection in the intermediate stress states found in the neck of tensile specimens and in notched tensile specimen was examined through an analysis with a triaxial loading, while for comparison the extreme case of deformation under purely hydrostatic loading was performed.

17. RESULTS.

17.1. UNIAXIAL TENSION.

The finite element model was subjected to increments of displacement loading on the remote boundary y = constant up to a final strain of the order of 30 times the initial yield strain.

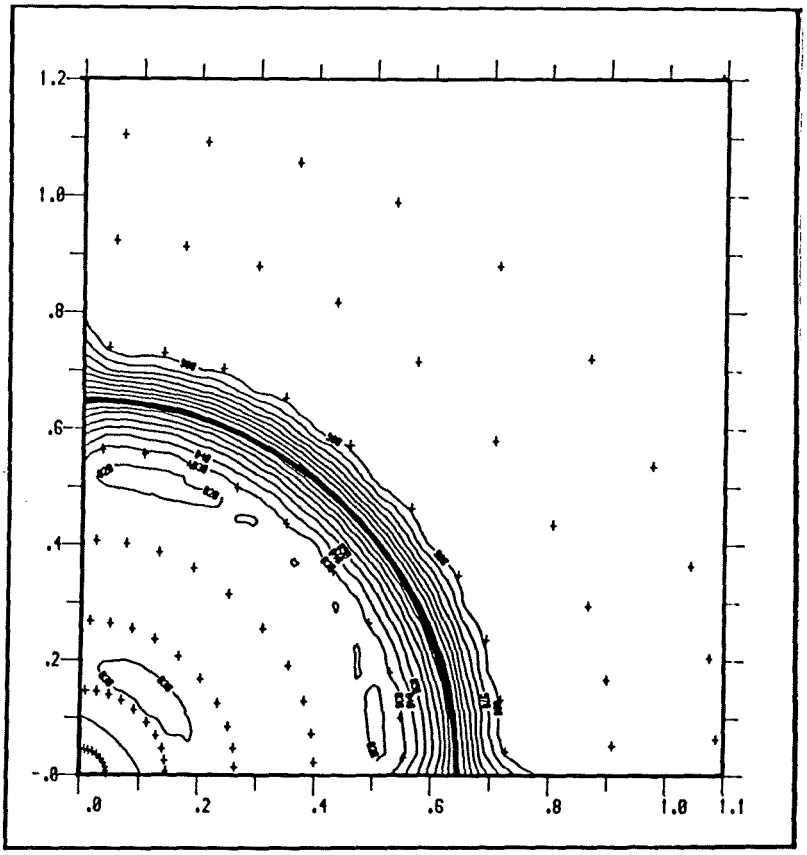

Fig.17.1. The aggregate effective stress near an equiaxed porous inhomogeneity in a porous environment. $\bar{Z} = 0.9\sigma_0$ on contour 900, $\bar{e}^p_\infty = 24e_0$.

Contour plots (fig.17.1 and fig.17.2) of stress and strain quantities show only small gradients both inside the patch and in the remote field throughout the whole of the loading history although significant stress and strain gradients are produced near the interface. Such a

sharply defined interface is an extreme case, compared with which a more realistic diffuse interface might be expected to produce less severe deformation gradients.

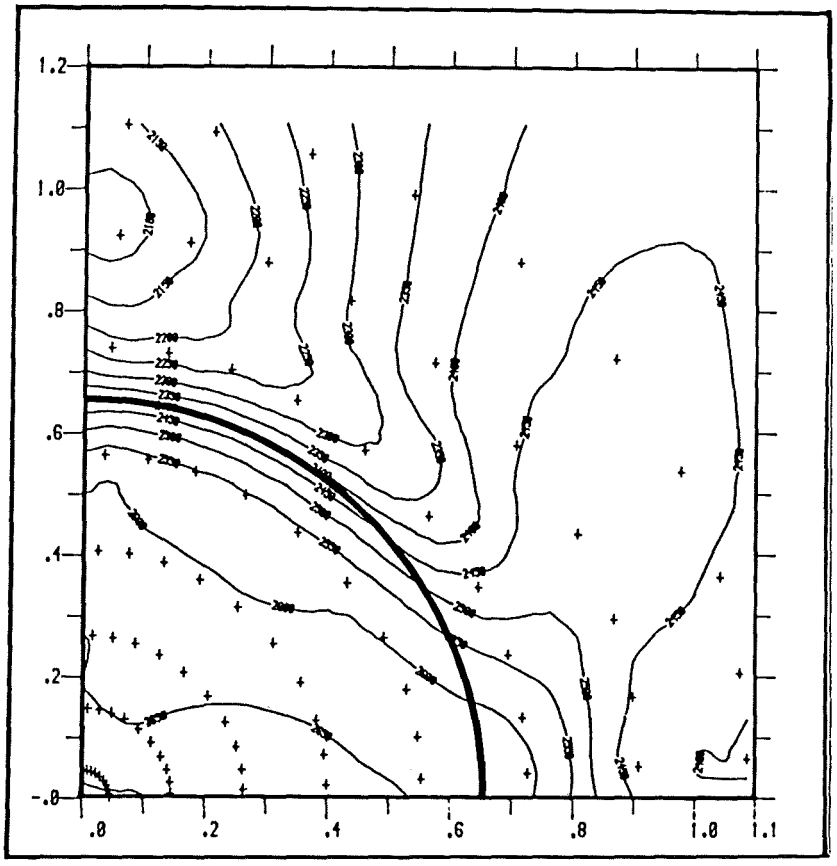

Fig.17.2. The matrix effective plastic strain near an equiaxed porous inhomogeneity in a porous environment. $\bar{e}^p = 22e_0$ on contour 2200, $\bar{e}^p_\infty = 24e_0$.

Both locally and in the remote environment, $\bar{e}^p$ developed linearly with the remote strain as shown in fig.17.3 in which the ordinates are plotted with respect to the remote total uniaxial strain in the principal loading direction.

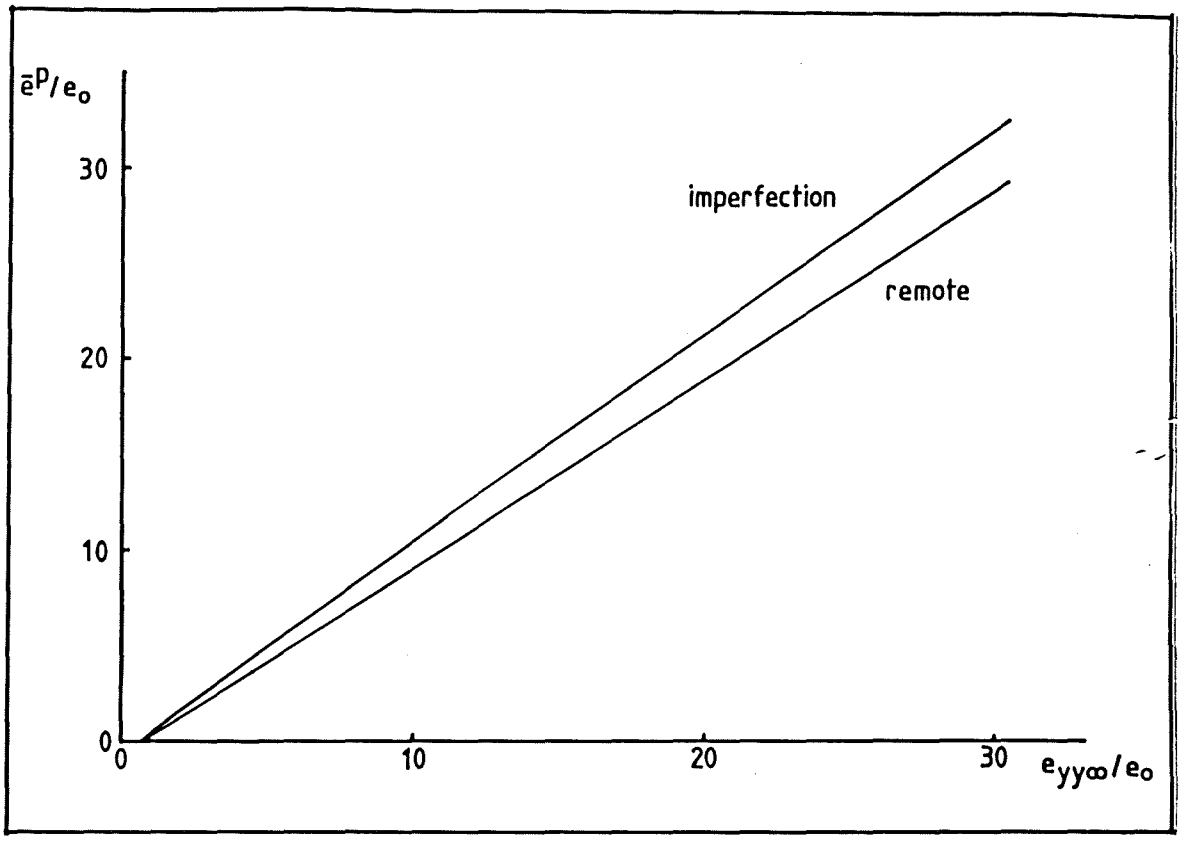

Fig.17.3. The development of the matrix plastic strain in an equiaxed porous inhomogeneity and in the porous environment as functions of the remote uniaxial strain.

From fig.17.3 it is apparent that in uniaxial tension there is little strain concentration within the imperfection, although the porosity has a marked effect in relieving the aggregate effective stress $\bar{Z}$ (fig.17.4). However, as the hydrostatic stress is also reduced in much the same way, the ratio of $Z_{kk}/\bar{Z}$ is relatively insensitive to increasing deformation. In the uniaxial case there is a small but definite increase in porosity both in the inhomogeneity and in the remote environment. However the ratio of the porosity in the patch to the remote porosity remained constant throughout the deformation history, as in fig.17.5.

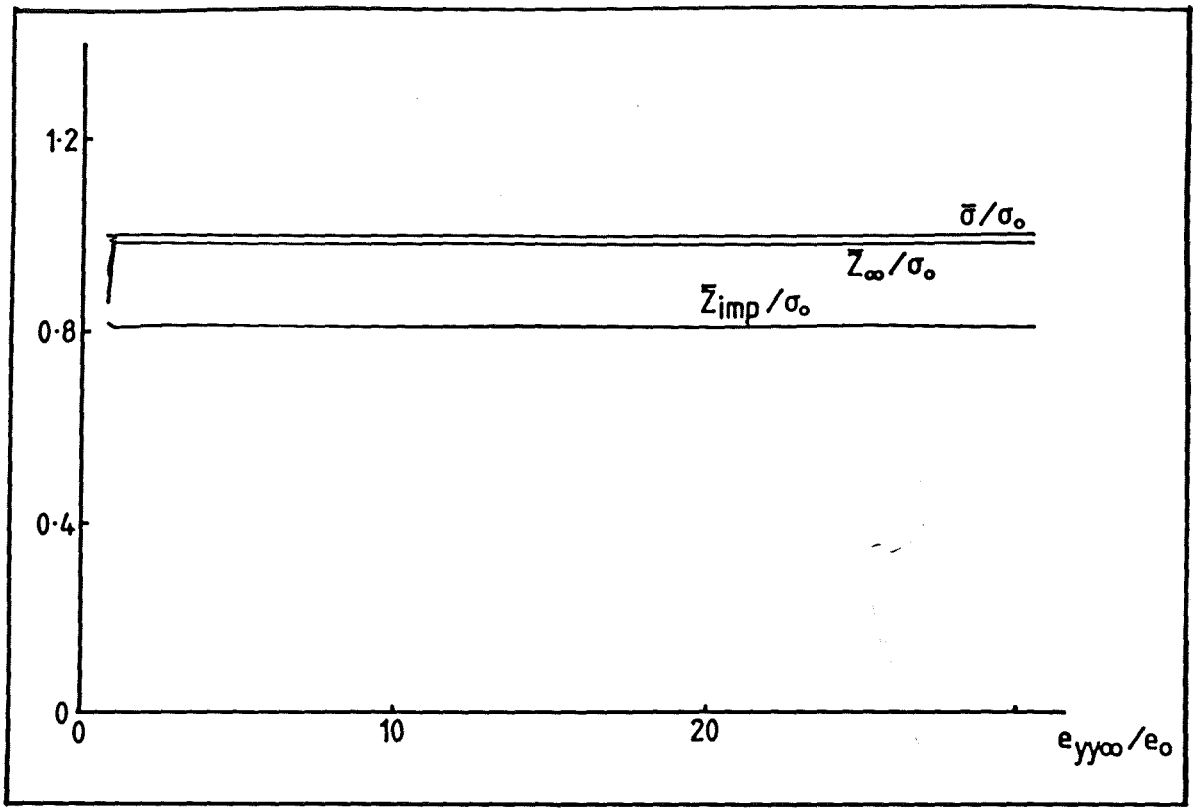

Fig.17.4. The development of the aggregate stresses with deformation for an equiaxed porous inhomogeneity and its porous environment.

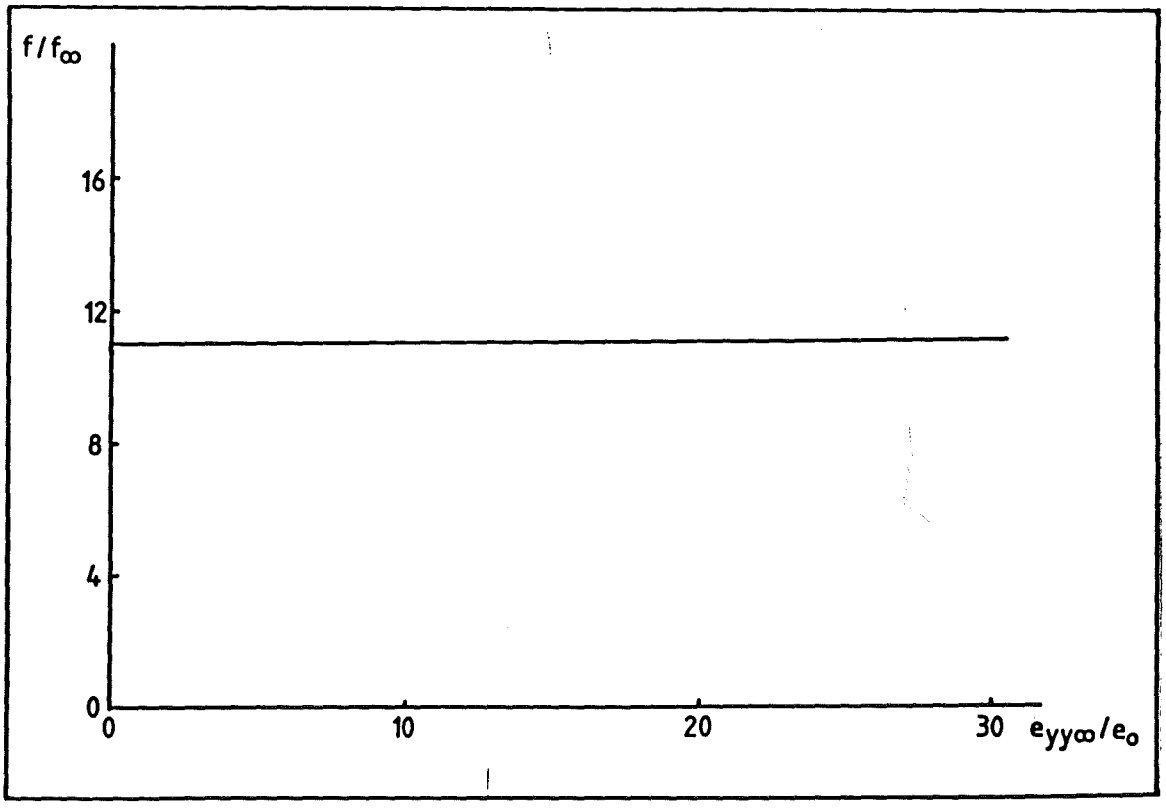

Fig.17.5. The ratio of the porosity in the inhomogeneity to the remote porosity for a porous inhomogeneity in an porous environment.

In the case of a non-porous environment, a small matrix strain concentration was evident in the average material near the equator of the patch (fig.17.6) while the $\bar{e}^p$ within the interior was considerably less than that in the surrounding material.

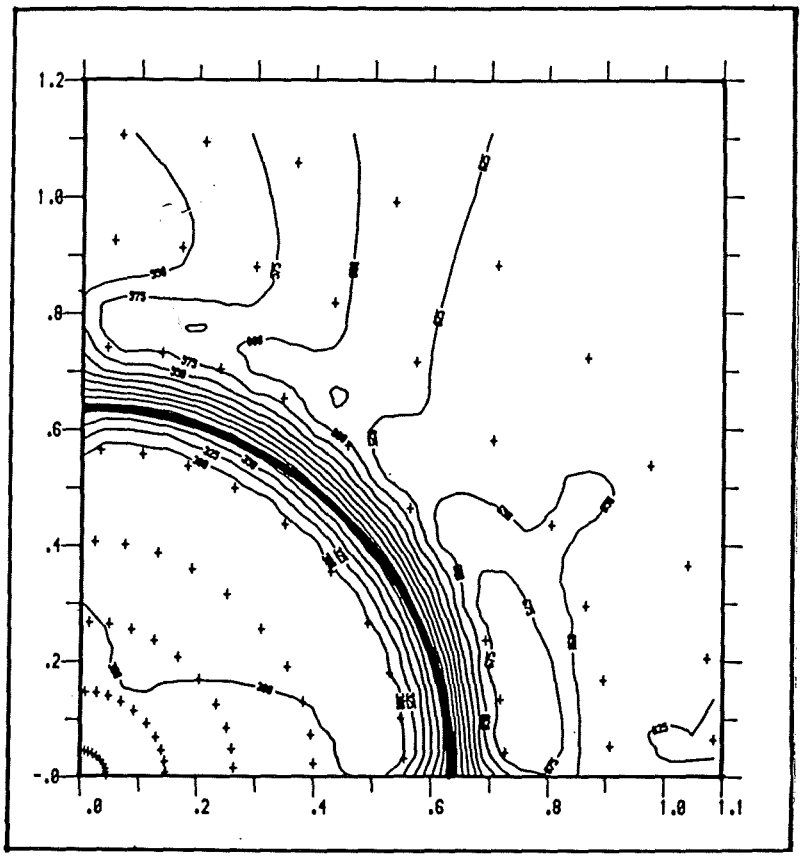

Fig.17.6. The matrix effective plastic strain near a porous inhomogeneity in a non-porous environment. $\bar{e}^p = 60e_0$ on contour 600, $\bar{e}^p_\infty = 62.5e_0$.

17.2. HYDROSTATIC TENSION.

Since the growth of the porosity in uniaxial tension is small, a similar finite element model was subjected to all round tension for which the remote triaxiality approaches infinity. With hydrostatic loading however, the numerical process became unstable before the development of full plasticity, being unable to bring the

current stress points onto the yield surface after 25 iterations. There is therefore little to be gained from the results other than to note that the local stress concentration in the imperfection is higher than that in the uniaxial case.

17.3. INTERMEDIATE STRESS STATES.

Although theoretically interesting, the behaviour of an inhomogeneity subject to hydrostatic remote loading is of limited applicability to the service loading of engineering components. In contrast the uniaxial case, while of both theoretical and practical importance, does not adequately describe the stress field in the centre of a notched tensile specimen or ahead of a crack tip. An approach to the modelling of such stress fields was made by a finite element analysis of a porous inhomogeneity in an intermediate stress state, in which the ratio of the remote displacements was adjusted such as to maintain a remote triaxiality of 1.0 ± 0.1. Such a stress state is of the order of that found in the centre of the notched tensile specimens used in the experimental work described earlier.

Due to the onset of numerical instability, the analysis of an inhomogeneity subject to intermediate triaxiality was limited to remote strains of the order of 7 times e_0. From this the behaviour at large strains must be inferred, with the caveat that such inferences may prove less reliable at greatly increased deformation. As before only small stress and strain gradients are apparent within the inhomogeneity, significant gradients being restricted to the interfacial elements (fig.17.7 and fig.17.8).

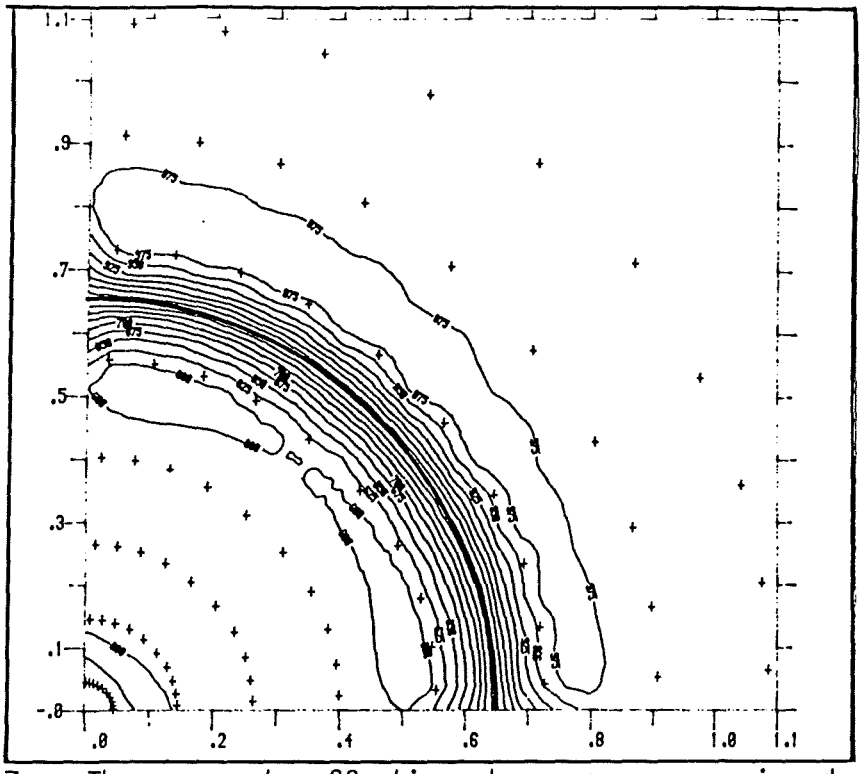

Fig.17.7. The aggregate effective stress near an equiaxed porous inhomogeneity in a porous environment subject to an intermediate triaxial loading. $\bar{Z} = 0.6\sigma_0$ on contour 600, $\bar{e}^p_\infty = 16.6e_0$.

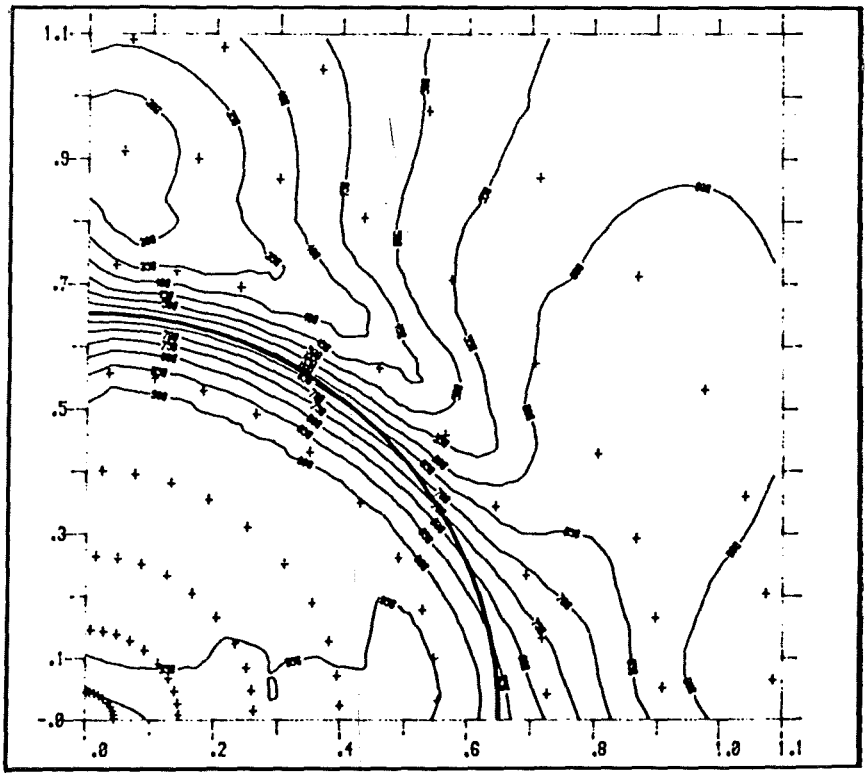

Fig.17.8. The matrix effective plastic strain near an equiaxed porous inhomogeneity in a porous environment subject to an intermediate triaxial loading. $\bar{e}^p = 6e_0$ on contour 600, $\bar{e}^p_\infty = 16.6e_0$.

While the strain concentration around the inhomogeneity is greater than in the uniaxial case, it still tends to a moderate value of approximately 1.8 as full plasticity develops in the intermediate triaxiality of the remote loading, as shown in fig.17.9. As expected the void growth rate in this inhomogenity subject to a stress state similar to that within a notched tensile specimen is greater than that with uniaxial loading, but again the ratio of the local porosity to the remote value remains virtually constant (fig.17.10).

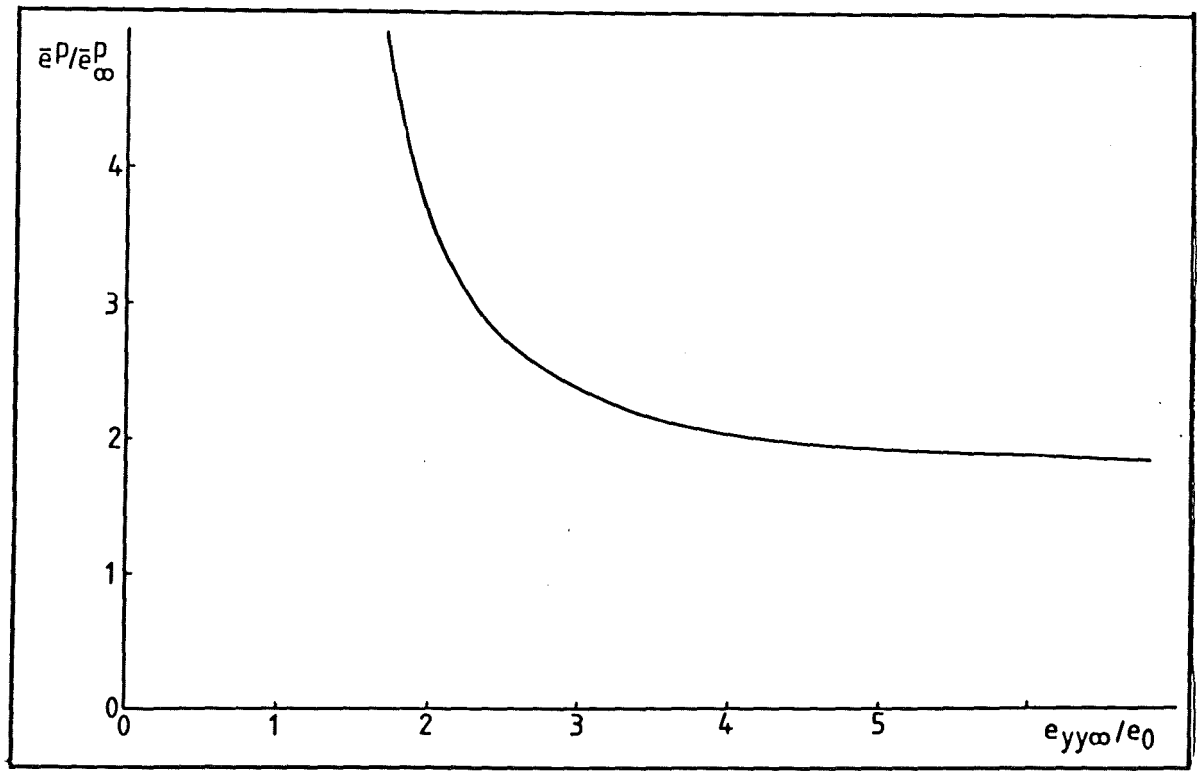

Fig.17.9. The development of the matrix strain concentration within an equiaxed porous inhomogeneity in a porous environment subject to an intermediate triaxial loading.

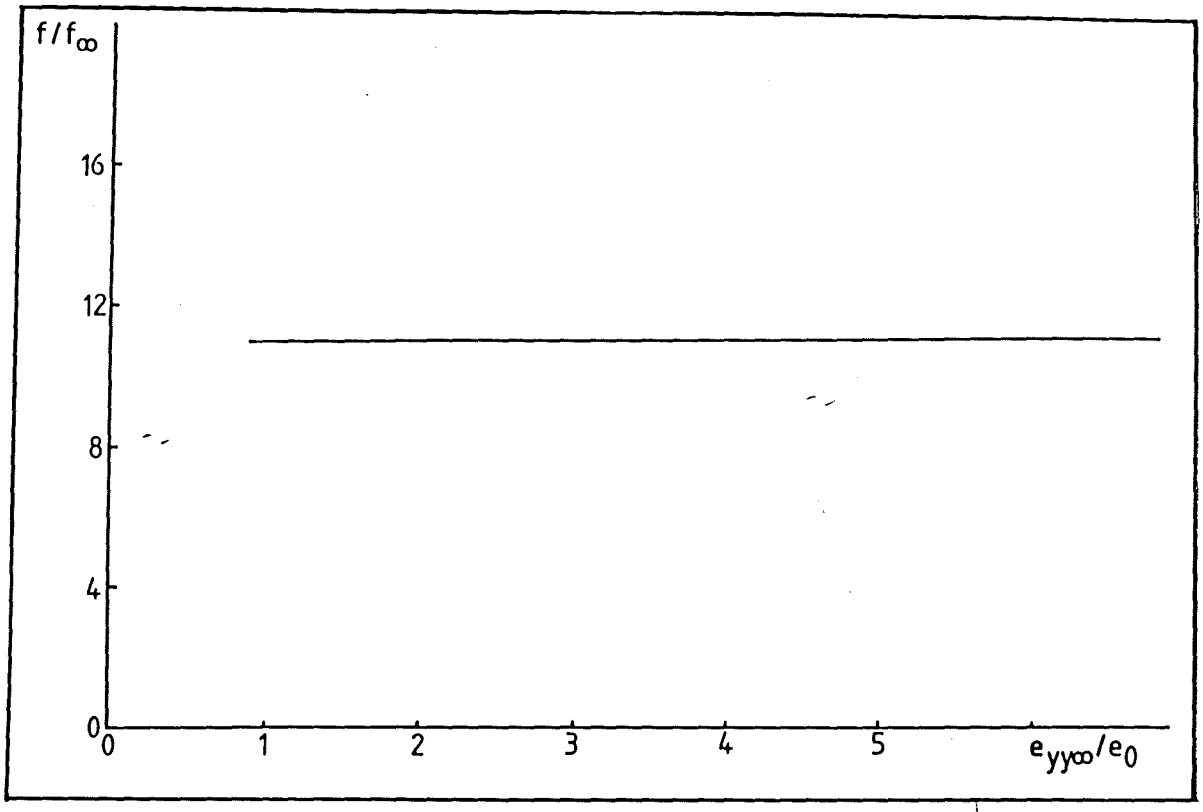

Fig.17.10. The ratio of the porosity in the inhomogeneity to the remote porosity for a porous inhomogeneity in a porous environment subject to an intermediate triaxial loading.

18. DISCUSSION.

The contained porous imperfection analysed in the present work may be regarded as intermediate between an arbitrary volume of average aggregate material and a void, which can be thought of as an imperfection in which the local porosity f = 1. The effect of hydrostatic stress in intensifying the strain concentration and deformation gradients near a single void are well known from the work of Rice and Tracey (1969), McClintock (1968) and Budiansky, Hutchinson and Slutsky (1981) and the porous inhomogeneity shows similar effects whereby increasing triaxiality intensifies the strain gradients close to the interface as well as enhancing the matrix strain concentration and the dilation rate within the inhomogeneity. Not surprisingly, for both the low and intermediate hydrostatic stress levels of relevance to tensile tests, the enhanced porosity of the imperfection has a significant effect in lowering both Z_{kk} and $\bar{Z}$, but in such a way that the ratio of $Z_{kk}/\bar{Z}$ is relatively insensitive to increasing deformation. For these stress states, the normalised void growth rate $(1/f)(df/d\bar{E}^p_\infty)$ expressed in terms of the remote strain is the same both in the inhomogeneity and in the remote field and the ratio of the dilations reflects the ratio of the initial void volume fractions at these locations. In uniaxial tension this growth rate is similar to the value of approximately 1.0 determined by Budiansky, Hutchinson and Slutsky (1981) for a single void in an infinite, strongly hardening matrix (m = 3).

While the need for a simple yield surface prevents the ideal case being realised, it is reasonable to expect, as found, that the growth rates for voids in a porous material with low void volume

fractions ($f = 0.01$), subject to moderate triaxialities, are close to those for a single isolated void in a similar stress state. It is of more significant to note that for moderate triaxialities, the enhanced porosities in the imperfection show similar growth rates to those for a single void. The effect of the deformation is to exacerbate the absolute difference in porosity between the imperfection and the remote field. Failure will then initiate in the imperfection before the surrounding material.

The strain concentrations within inhomogeneities are largely determined by the relative hardening rates on either side of the interface with more negative hardening rates in the inhomogeneity tending to favour higher strain concentrations. In the case of the unbounded planar shear band of Yamamoto (1978), very high strain concentrations become possible as the hardening rate approaches zero in the band. In such a situation, the ductility is insensitive to the detailed mechanism of flow localisation and of void coalescence but is largely determined by the strain concentration which allows massive strains in the imperfection. However, if the inhomogeneity is contained as in the current results, weak deformation gradients are obtained within the imperfection for an aggregate material whose hardening rate is negative throughout the deformation history and significantly less than that of the surrounding material. In this case the strain concentrations and dilation rates in the contained spherical inhomogeneity prior to localisation are limited by the kinematic constraint of the surrounding material and the attainment of the condition for flow localisation or failure within the inhomogeneity is insufficient to cause total macroscopic failure or even the formation of a crack-like defect. For such failure to occur, the appropriate

conditions must be met over a size scale sufficient for growth rate of adjacent voids to be enhanced by the stress and strain concentrations associated with the inhomogeneity to such an extent that the defect tends to propagate. In this context, the strain concentration depends on the shape of the imperfection and is small for an equiaxed imperfection. The application of a flow localisation criterion in real materials is complicated by the fact that the strain state within contained 3-space imperfections need not be identical to that of the remote field (Hancock and Brown (1984)) but the strain concentration associated with such imperfections clearly plays an important role in determining ductility, the highest strain concentrations and dilation rates being achieved in eccentric contained imperfections.

19. CLOSURE.

The experimental and theoretical results contained in the current work form the framework for a model of failure initiation by void growth and coalescence in ductile metals containing hard particles. The essential features of this model are as follows:

> void nucleation is a statistical process in which the probability of nucleation is consistent with a criterion based on the maximum radial stress around the inclusion interface.

For the particular material tested and with the derived expression for the maximum interfacial radial stress, the modal value of interfacial strength for well-bonded particles is found to be about 7 times the initial yield stress. However, the experimental distribution is bimodal and shows a significant proportion of particles around which the voids are effectively pre-existing.

> Void growth in a continuing deformation field has a progressively destabilising effect in opposition to the stabilising influence of strain hardening, and leads to the initiation of failure by a flow localisation process at a porosity of about 4 times the initial value.

This is however, an empirical value and provides no insight into the physics of failure. To investigate the initiation of failure, the material was regarded as a dilating porous continuum, as this approach

most clearly recognises that:

> ductility is determined by the competition between the stabilising influence of strain hardening of the flow field in the presence of the destabilising influence of void growth.

Over size scales which are large enough to represent the average material, the hardening rate at failure of the porous aggregate is positive. However:

> the random distribution of inclusions in real materials implies a statistical variation of the void volume fraction throughout the material and leads initially to failure in bad patches of material with high local porosities.

The local hardening rate is then also a random variable with significant probabilities at small size scales of finding volumes in which the hardening rate deviates significantly from the mean. In such inhomogeneities, the hardening rate at failure is negative but void coalescence in such patches will be localised and contained by the surrounding stable material. The failed region does not therefore constitute a crack-like defect but rather produces a large isolated void.

> Crack-like behaviour requires the strain concentrations from the defect to act over distances large compared to the average void spacing, which introduces the concept of a critical failed volume.

This requires void coalescence in an inhomogeneity with a radius at least equal to the average void spacing. Taking into account the statistics of the inclusion distribution, there is a high probability of such a region having a hardening rate close to zero when cracks are observed to form. Hence:

> localisation may be triggered by the instability produced by near-zero hardening rates in a critical volume comprising 8 unit cells of the material.

The statistics of the inclusion distribution imply that failure may occur in the absence of the large strain concentrations. Failure is found to depend on local conditions and there is no experimental evidence in support of any effect of the remote strain state.

The model proposed is consistent with experiments on a low yield, highly ductile material containing a single population of similarly sized inclusions. While the failure of real structural materials is generally complicated by the interaction of more than one generation of hard particles, it might reasonably be expected that individual features of the model may be applied at the appropriate size scale. This remains to be seen.....

REFERENCES

American Institute of Physics Handbook, 3rd Ed, McGraw-Hill, New York, 1972, 2-52.

Aoki S, Kishimoto K, Takeya A and Sakata M (1984). Effects of micro-voids on crack blunting and initiation in ductile materials. International Journal of Fracture, 24, 267-278.

Aravas N and McMeeking R M (1984). Microvoid growth and failure in the ligament between a hole and a blunt crack tip. To be published.

Argon A S, Im J and Safoglu R (1975). Cavity formation from inclusions in ductile fracture. Metallurgical Transactions, 6A, 825-837.

Ashby M F (1966). Work hardening of dispersion-hardened crystals. Philosophical Magazine, 14, 1157-1178.

Berg C A (1962). The motion of cracks in plane viscous deformation. Proceedings of the Fourth US National Congress of Applied Mechanics, ASME, 1962, 885-892.

Berg C A (1970). Inelastic behaviour of solids, edited by Kanninen M F, Adler W F, Rosenfield A R and Jaffee R I, McGraw-Hill, New York, 1970, 171-210.

Bishop J F W and Hill R (1951). A theory of the plastic distortion of polycrystalline aggregate under combined stress. Philosophical Magazine, 42, 414-427.

Bridgman P W (1952). Studies in large plastic flow and fracture, McGraw-Hill, New York, 1952, p9.

Brown D K, Hancock J W, Thomson R D and Parks D (1980). The effect of dilating plasticity on some elastic-plastic stress and strain concentration problems relevant to fracture. Numerical Methods in Fracture Mechanics (Proceedings of the 2nd International Conference), edited by Owen R J and Luxmoore A R, Pineridge Press, Swansea, 1980, 309-323.

Brown L M and Stobbs W M (1976). The work hardening of copper-silica. Philosophical Magazine, 34, 351-372.

Budiansky B, Hutchinson J W and Slutsky S (1981). Void growth and collapse in viscous solids. Mechanics of Solids, The Rodney Hill 60th Anniversary Volume (edited by Hopkins H G and Sewell M J), Pergamon Press, 1981.

Chen W H (1971). Necking of a bar. International Journal of Solids and Structures, 7, 685-717.

Edelson B and Baldwin W (1962). The effect of second phase particles on the mechanical properties of alloys. Transactions of the ASM, 55, 230.

Eshelby J D (1957). The determination of the elastic field of an ellipsoidal inclusion and related problems. Proceedings of the Royal Society, A241, 376-396.

GINO-F User Manual. CAD Centre, Cambridge, 1976.

Goodier J N (1933). Concentration of stress around spherical and cylindrical inclusions and flaws. ASME Applied Mechanics Magazine, 55, 39-44.

Goods S H and Brown L M (1979). The nucleation of cavities by plastic deformation. Acta Metallurgica, 27, 1-15.

Goods S H and Nix W D (1978). The kinetics of cavity growth and creep fracture in silver containing implanted grain boundary cavities. Acta Metallurgica, 26, 739-752.

Griffiths A A (1921). The phenomena of rupture and flow in solids. Philosophical Transactions of the Royal Society, A221, 163.

Gurland J (1972). Fracture of cementite particles in spheroidised steel. Acta Metallurgica, 20, 735-741.

Gurson A L (1977). Continuum theory of ductile rupture by void nucleation and growth, Part 1 - Yield criteria and flow rules for porous ductile media. Transactions of the ASME, Journal of Engineering Materials Technology, 99, 2-15.

Hancock J W and Brown D K (1983). On the role of strain and stress state in ductile failure. Journal of the Mechanics and Physics of Solids, 31, 1-24.

Hancock J W and Mackenzie A C (1976). On the mechanisms of ductile failure in high strength steels subjected to multi-axial stress states. Journal of the Mechanics and Physics of Solids, 24, 147-169.

McClintock F A (1967). 'Ductility'. Proceedings of the ASM Conference on Ductility, 1967.

McClintock F A (1968). A criterion for ductile fracture by the growth of holes. Transactions of the ASME, Journal of Applied Mechanics, 35, 362-371.

McClintock F A and Rhee S S (1962). Proceedings of the 4th US National Congress in Applied Mechanics, 2, 1002.

Mackenzie A C , Hancock J W and Brown D K (1977). On the influence of state of stress on ductile failure initiation in high strength steels. Engineering Fracture Mechanics, 9, 167-188.

McMeeking R M and Rice J R (1975). Finite element formulations for problems of large elastic-plastic deformation. International Journal of Solids and Structures, 11, 601-616.

Marcal P V and King I P (1967). Elastic-plastic analysis of 2-dimensional systems by the finite element method. International Journal of the Mechanical Sciences, 9, 143-155.

Melan E (1938). Ingenieur-archiv, 9, 116.

Mudry F (1982). Etude de la rupture ductile et de la rupture par clivage d'aciers faiblement allies. These d'Etat, Universite de Technologie de Compeigne, 1982.

NAG Fortran Library. Numerical Algorithms Group, Oxford, 1983.

Nagtegaal J, Parks D M and Rice J R (1974). On numerically accurate finite element solutions in the fully plastic range. Computer Methods in Applied Mechanics and Engineering, 4, 153-177.

Needleman A (1972). A numerical study of necking in circular cylindrical bars. Journal of the Mechanics and Physics of Solids, 20, 111-127.

Needleman A (1972). Void growth in an elastic-plastic medium. Transactions of the ASME, Journal of Applied Mechanics, 1972, 964-970.

Needleman A and Rice J R (1978). Limits to ductility set by plastic flow localisation. Mechanics of sheet metal forming, edited by Koistiner D P, Plenum Press, New York, 1978.

Norris D M, Moran B, Scudder J K and Quinones D F (1978). A computer simulation of the tension test. Journal of the Mechanics and Physics of Solids, 26, 1-19.

Orr J and Brown D K (1974). Elastoplastic solution for a cylindrical inclusion in plane strain. Engineering Fracture Mechanics, 6, 261-274.

Puttick K E (1959). Philosophical Magazine, 4, 964-969.

Rice J R (1968). A path independent integral and the approximate analysis of strain concentration by notches and cracks. Transactions of the ASME, Journal of Applied Mechanics, 1968, 379-386.

Rice J R (1976). The localisation of plastic deformation. Theoretical and Applied Mechanics, edited by Koiter W T, North-Holland, 1976, 207-220.

Rice J R and Tracey D M (1969). On the ductile enlargement of voids in triaxial stress fields. Journal of the Mechanics and Physics of Solids, 17, 201-217.

Rice J R and Tracey D M (1973). Computational fracture mechanics. Numerical and Computer Methods in Structural Mechanics, Academic Press, 1973, 599-601.

Rudnicki J W and Rice J R (1975). Conditions for the localisation of deformation in pressure sensitive dilatant materials. Journal of the Mechanics and Physics of Solids, 23, 371-394.

Tanaka, Mori and Nakamura (1970). Philosophical Magazine, 21, 267.

Thomason P F (1981). Ductile fracture and the stability of incompressible plasticity in the presence of microvoids. Acta Metallurgica, 29, 763-777.

Tipper C F (1949). The fracture of metals. Metallurgia, 39, 133-137.

Tvergaard V (1981). Influence of voids on shear band instabilities under plane strain conditions. International Journal of Fracture, 17, 389.

Tvergaard V (1982). On localisation in ductile materials containing spherical voids. International Journal of Fracture, 18, 237-252.

Tvergaard V (1982). Ductile failure by cavity nucleation between larger voids. Journal of the Mechanics and Physics of Solids, 30, 265-286.

Yamamoto H (1978). Conditions for shear localisation in the ductile fracture of void-containing materials. International Journal of Fracture, 14, 347-365.

Zienkiewicz O C and Phillips D V (1971). An automatic mesh generation scheme for plane and curved surfaces by isoparametric coordinates. International Journal for Numerical Methods in Engineering, 3, 519-528.

APPENDICES

A.1. THE FINITE ELEMENT PROGRAMS.

A.1.1. THE MAIN PROGRAM.

The finite element program used in the current work is a subset of an old form of the commercially available MARC package, modified by a number of workers. From the original small-strain package, the routines needed to perform elastic/plastic analysis were altered to perform large strain analysis of porous elastic/plastic materials. The program is based on the incremental partial stiffness formulation of Marcal and King (1967) in which the vector of deviatoric stress increments (ds_i) is related to the vector of deviatoric strain increments (de_j) through the equation:

$$(ds_i) = (D_{ij})(de_j) \qquad (A.1.1).$$

The components of the matrix D_{ij} in equation A.1.1 may be expressed by the chain rule as:

$$D_{ij} = \partial s_i / \partial e_j .$$

in which the stiffness-like terms $\partial s_i / \partial e_j$ were called 'partial stiffnesses' by Marcal and King (1967).

In the elastic zone, equation A.1.1 is linear and may be solved to give the strain increments. For plastic deformation the equation is non-linear and the partial stiffnesses may be regarded as tangent moduli. However, a difficulty arises when the element is

elastic at the start of any load increment but yields during that increment for then the partial stiffnesses change dramatically during the increment. In this case, the strain increments are determined from a mean partial stiffness:

$$(D_{ij}) = m(D_{ij})^{el} + (1-m)(D_{ij})^{el/p} \qquad (A.1.2)$$

where m is a weighting factor expressing the proportion of the current load increment for which the deformation is purely elastic. Here $(D_{ij})^{el}$ is the elastic partial stiffness, given by the diagonal matrix:

$$(D_{ij})^{el} = 2G\delta_{ij}$$

while $(D_{ij})^{el/p}$ is the elastic/plastic partial stiffness, which must transform the appropriate strain increment into a stress increment which satisfies the yield function. This is calculated by the iterative method of Rice and Tracey (1973), in which an initial estimate for the strain increment vector Δe in the current load step is chosen parallel to the strain increment vector in the previous load step, scaled by a factor equal to the ratio of the magnitudes of the corresponding load increments. Considering this strain increment to be initially elastic would give a deviatoric stress increment:

$$\Delta s = 2G\Delta e$$

as in the π-plane projection in fig.A.1.1. The final stress in this case would then be:

$$s_2 = s_0 + \Delta s$$

and yielding in the non-hardening case would occur at the stress s_1, with m specified from the relation:

$$s_1 = s_0 + m\Delta s.$$

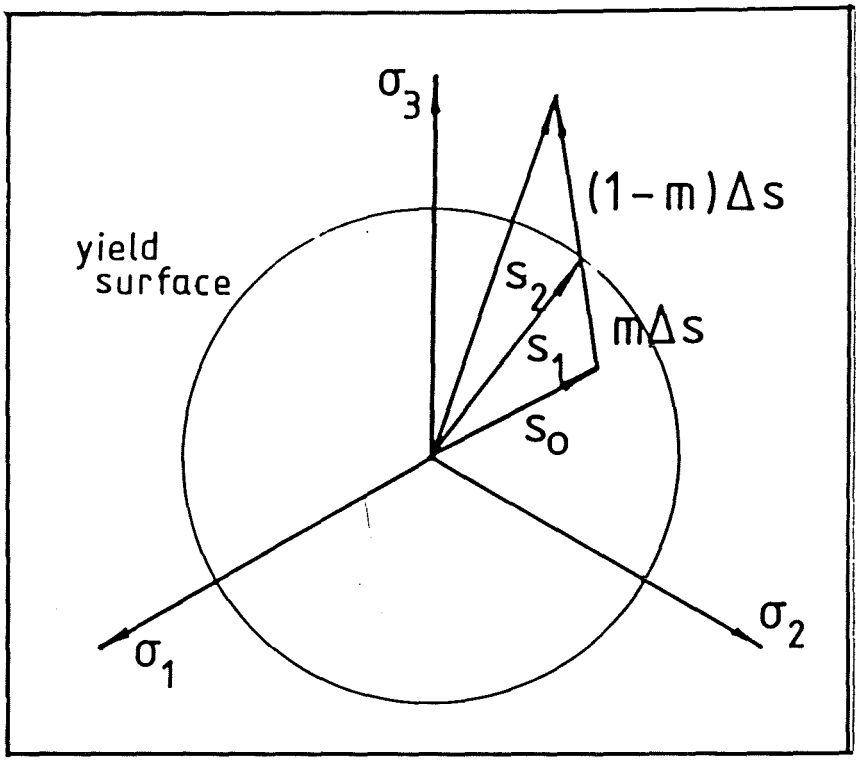

Fig.A.1.1. The π-plane projection of the stress increments for an element which yields in the current load increment.

This value of m based on an initial estimate Δe is then used to calculate a unit normal n, given by:

$$n = (s_1 + s_2)/|s_1 + s_2|$$

$$\Rightarrow n = (s_1 + G(1-m)\Delta e)/|s_1 + G(1-m)\Delta e|$$

which, with:

$$(D_{ij})^{el/p} = 2G(\delta_{ij} - n_k n_k)$$

defines a partial stiffness $(D_{ij})^{el/p}$ to transform a strain increment $(1-m)\Delta e$ into a stress increment which lies exactly on the yield surface. This procedure may be extended to hardening materials by the use of the average hardening rate described by Tracey (1973).

Nagtegaal, Parks and Rice (1974) have noted that all tangent modulus finite element solutions, including that used here, satisfy the virtual work expression:

$$\int_S \dot{T}_i \dot{u}_i dS = \Sigma \int_V \dot{\sigma}_{ij} \dot{e}_{ij} dV \qquad (A.1.3)$$

where $\dot{T}_i$ and $\dot{\sigma}_{ij}$ are an equilibrium set of force and stress rates while $\dot{u}_i$ and $\dot{e}_{ij}$ are a compatible set of displacement and strain rates for a body with surface area S. The corresponding volume is then given as the summation Σ over the set of finite elements of volume V. Decomposing the deformation into mean and deviatoric components, equation A.1.3 may be written as:

$$\int_S \dot{T}_i \dot{u}_i dS = \Sigma \int_V (\dot{s}_{ij} \dot{\epsilon}_{ij} + K(\dot{e}_{kk})^2) dV$$

where ϵ_{ij} are the strain deviators and K is the bulk modulus. Normality implies that $s_{ij}\epsilon_{ij}$ is never negative and so:

$$\int_S \dot{T}_i \dot{u}_i dS \geq \Sigma \int_V K(\dot{e}_{kk})^2) dV.$$

In order for a limit load to exist, $\dot{e}_{kk}$ must vanish in every element throughout the mesh. With the constraint arising from the interpolation functions for the elements this imposes an additional constraint

on the deformation modes of the mesh. In the case of a rectangular array of plane strain elements the effect of the additional constraint is to enforce the same e_{xx}, and e_{yy}, in every element of the mesh, which is unrealistic. For grids of arbitrary quadrilaterals, the effect is pathological.

The additional constraint is shown by Nagtegaal, Parks and Rice (1974) to be a consequence of the strain-displacement relations for the elements and is relaxed by the introduction of a constant dilation rate in each element:

$$\phi = e_{kk}$$

as an independent degree of freedom in the otherwise non-dilational element formulation. A variational principle was devised from which ϕ is found to be:

$$\phi = (1/V) \int_V u_{kk} dV$$

for each element, and a modified strain increment is defined from:

$$\epsilon'_{ij} = \epsilon_{ij} + \delta_{ij}\phi.$$

The strain-displacement relationships then become:

$$\epsilon'_{ij} = (1/2)(u_{i,j} + u_{j,i}) + (1/3)\delta_{ij}(\phi - u_{k,k}).$$

Nagtegaal, Parks and Rice (1974) note that this modification may be made to most existing programs and while principally used to allow the calculation of limit loads, it was included in the current program to allow less constrained deformation than would otherwise be permitted.

The original small-strain version of MARC was given a large strain capability by McMeeking and Rice (1975) who adopted a finite deformation approach which rigorously accounts for rotational terms. In addition, their approach allows stress levels of the order of the current tangent modulus to be correctly handled. An updated Lagrangian formulation was chosen in which field variables are related to the current geometry of the deformed mesh. An incremental approach then linearises the constitutive equations for each step and allows the small strain routines for the constitutive moduli to be used for large deformations given a proper choice of work-conjugate measures of stress and strain rates. In such incremental formulations, the current deformed state may be identified as a reference state in which case all the possible stress measures will be identical. The same cannot be said of the stress rates however. Choosing the rate-of-deformation tensor D as their strain rate term, McMeeking and Rice (1975) identify the Kirchhoff stress τ as the conjugate stress variable. This is expressed as an equivalent Cauchy stress σ in the program output through the expression:

$$\tau_{ij} = J\,\sigma_{ij}$$

where J is the Jacobian of the deformation, equal to the ratio of the volume in the current state to that in the reference state and instantaneously equal to 1. Inserting these stresses into a rate form of the virtual work equation due to Hill (1959) gave:

$$\int_V (\tau_{ij}\delta D_{ij} - (1/2)\sigma_{ij}\delta(2D_{ik}D_{kj} - v_{k,i}v_{k,j}))dV = \int_S T_i\delta v_i dS + \int_V b_i\delta v_i dV \qquad (A.1.4)$$

where the integrations are over the current deformed shape. T and b are nominal surface tractions and body forces calculated with respect to the current configuration.

A vector Q of nodal degrees of freedom was chosen and related to the element velocities v and rates of deformation D by the interpolation functions N via:

$$v = N\,Q$$

and:

$$D = B\,Q$$

where:

$$B_{ij} = (1/2)N_{i,j} + (1/2)N_{j,i}.$$

Equation A.1.4 was then recast in finite element form to give the equilibrium equations:

$$(\int_V B^T C B\, dV + K_S)(Q) = P$$

where P is the load vector, given by:

$$P = \int_V N^T b\, dV + \int_S N^T f\, dS.$$

K_S is an initial stiffness term, given as:

$$K_S = \int_V (N^T_{k,i}\, \sigma_{ij} N_{k,j} - 2B^T_{ki}\, \sigma_{ij} B_{kj})\, dV$$

while C is a rate independent constitutive matrix defined by:

$$\tau = C\,D.$$

For Prandtl-Reuss materials, C is expressible in the form:

$$C_{ij} = E'(\delta_{ik}\delta_{kl} + (\nu/(1-2\nu))\delta_{ij}\delta_{kl} - (3/2)(s_{ij}s_{ij}E')/(\sigma^2((2/3)h + E'))) \quad (A.1.5)$$

where:

$$E' = E/(1+\nu)$$

and:

$$h = d\sigma/de^p$$

is the tangent modulus obtained from a uniaxial tensile test. The last term in A.1.5 is only active during plastic loading.

The program described so far was used for the non-dilating analyses in the main text. The final modification was performed by Parks (unpublished) who recast the general theory of porous plasticity presented in chapter 2 into finite element form, providing the capability of analysing dilating materials. The program was written in FORTRAN IV for an IBM machine and amended to run in batch mode under VME/B on the ICL 2988 mainframe at Glasgow.

A.1.2. THE POST PROCESSOR.

The finite element program as described gives a full field analysis of the deforming grid and the output largely comprises listings of the stress components and scaled values of the displacement partial derivatives for each load increment. However, these quantities generally require further manipulation before they can be inserted into the ductile failure model developed in the current work. Furthermore, lists of numbers are not easily assimilated and graphical output of selected variables is required. The operations necessary to produce secondary quantities and graphical output were done within a post-processor which accesses a user-defined selection of the results files produced by the finite element program. At the discretion of the user, a number of output files are produced which may be printed or stored on disk. The diagram shown in fig.A.1.2 indicates the interaction of the program with its environment. File assignment is controlled by macros to minimise user intervention in driving the program and free the user to control output selection. The program was written in standard FORTRAN IV to assist portability and was structured to facilitate extension to meet additional processing requirements. Operation is controlled by a master segment whose function is to call subroutines which perform the arithmetic and control output.

Analytic solutions are not available for a number of the expressions required in the analysis and in such cases numerical routines were written which iterate such as to minimise a residual norm. Fig.A.1.3 shows a block diagram of the program logic at its highest level and while flowcharts down to the level of individual

subroutines can be produced, they are not appropriate here.

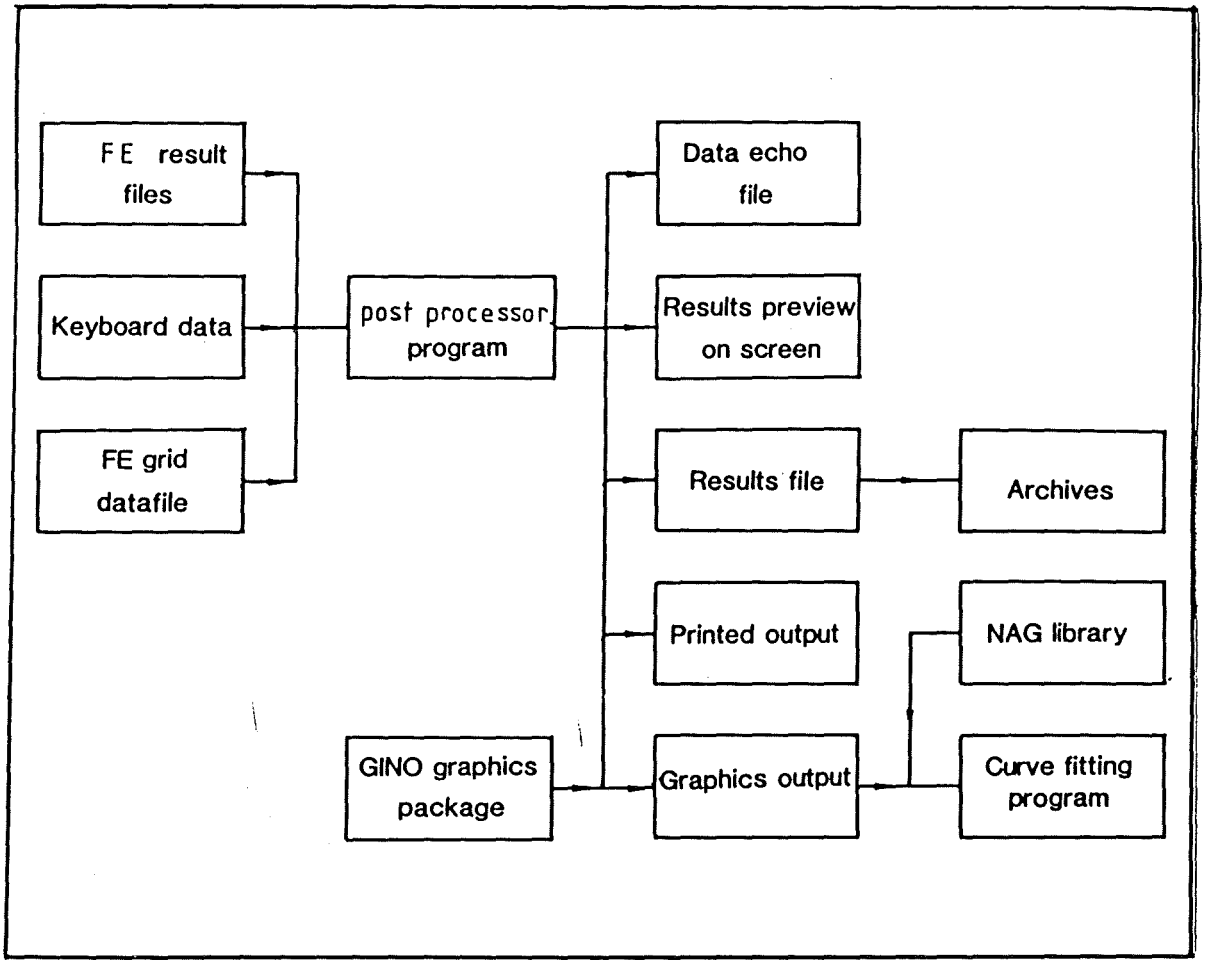

Fig.A.1.2. The flow of information around the post-processor.

The post-processor runs interactively under user control via responses to specific questions appearing on the screen. A wide choice of graphical output is available from a menu which allows any secondary variable to be contour mapped over any selected region of the finite element grid or to be plotted against any other variable on a two-axis graph. The graphics output uses the GINO package, and is available on a variety of terminals and hard copy devices.

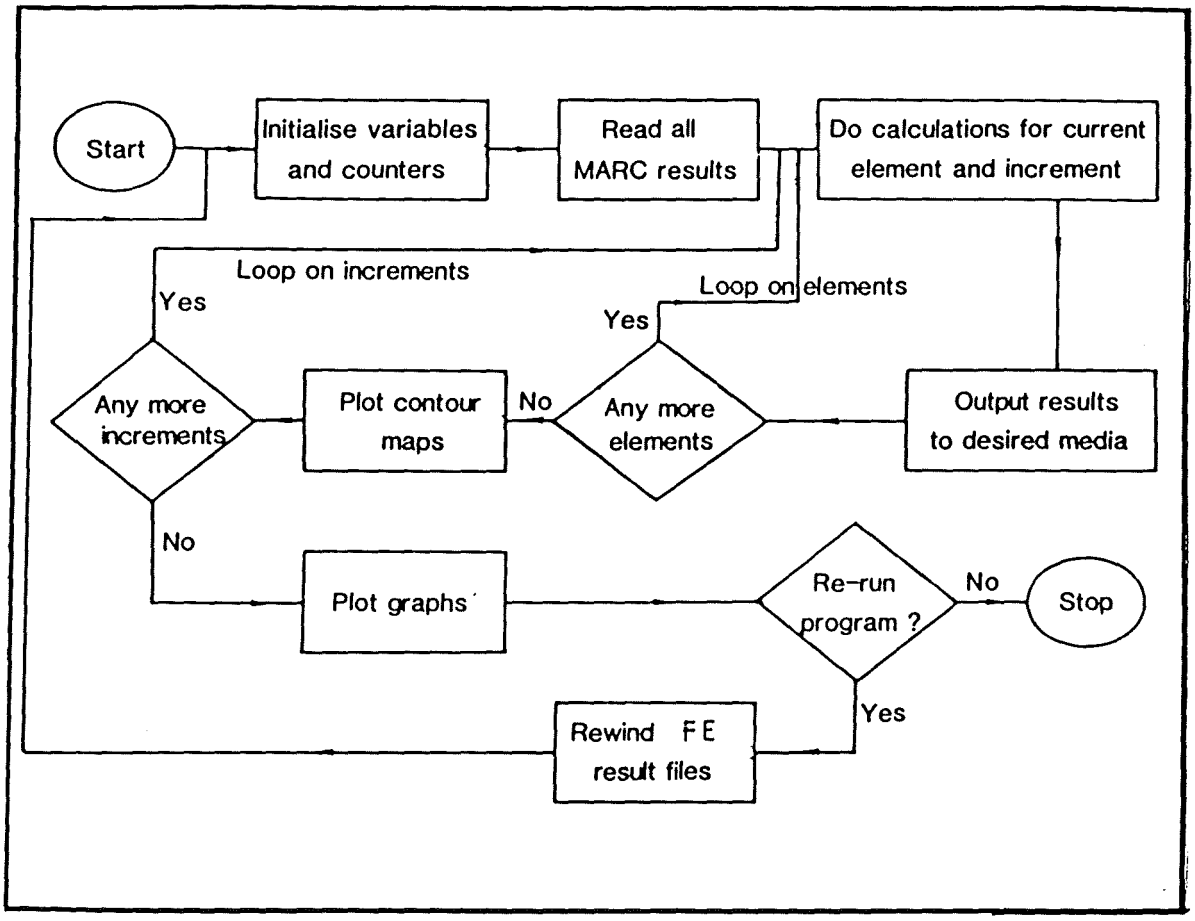

Fig.A.1.3. The high-level logic of the post-processor.

The source deck contains approximately 2000 card images but since FORTRAN IV not allow the assignment of dynamic arrays, the storage required by the DIMENSIONed arrays is considerable. This large work-space requirement implies that modifications may be needed for use on non-virtual machines. For historical reasons, arrays are transferred between subroutines as arguments rather than through COMMON blocks, and the latter is to be preferred if working space is limited.

A.2. THE NUMERICAL ANALYSIS OF VOID NUCLEATION.

In order to determine the local conditions at a nucleating void, the void growth equations of McClintock (1969) (equs.2.13) may be solved numerically, given boundary conditions in the form of the actual void shape for a known effective plastic strain. This requires that the local stress and strain conditions for any observed void be calculated and that a history of such local conditions be produced for that particular void. Such calculations were performed by the programs INTER-A and INTER-D for the A-notch and D-notch geometries respectively, making use of the full field finite element analyses of the notched specimens. The analysis of the unnotched specimen used an analytic solution based on Bridgman's (1952) results as verified by the finite element analysis of Needleman (1972).

An inherent feature of finite element solutions is that the process solves primarily for the unknowns at nodal points of the mesh and hence determines secondary quantities, often at the centroids of the elements. Further, in the non-linear analyses of incremental plasticity, results are output for each load increment. In the particular cases relevant to the current work, full field finite element analyses of the notch tensile specimens gave via the post-processor the positions of the element centroids together with the corresponding stress and strain quantities at each increment of an applied load measured in terms of the remote effective plastic strain.

In the experimental analysis attention was focussed on a number of voids lying near the transverse axis of a metallographic section through the deformed specimens. The finite element results

of interest are then the solutions for elements lying along this axis. These results can easily be abstracted from the full field analyses by the post-processor and were tabulated in the form of deformation histories of the element centroids. Such histories include the transverse coordinate of the centroid at each load step, defined as its distance from the origin of the grid. It is unlikely however that the strain at which any particular test is stopped will correspond exactly to the strain at the end of any increment but will lie between two increments. It is equally unlikely that any void observed on the metallographic section will coincide with the current position of an element centroid and in general voids lie between centroids. Hence, in order to determine the local conditions at the void at the end of the test, it is necessary to interpolate in two dimensions simultaneously, between load increments to the actual strain at the end of the test and between element centroids to the actual position of a void.

All of the programs described subsequently were written in double precision standard FORTRAN IV for the GEC 4070 at Glasgow University. This is part of the SERC Joint Academic Network (JANET). The post-processed finite element results were transferred directly from the ICL 2988. Due to the large number of file transfers involved in the solution, the programs were driven by large macros. Two dimensional interpolation was performed by the INTER programs on metallographic data pre-processed by a small program which scaled the dimensions measured from micrographs to actual sizes. Subsequent programs determined the nucleation strain for each void and the corresponding stress conditions at the inclusion/matrix interface and fig.A.2.1 shows the interaction of files required for the nucleation analysis.

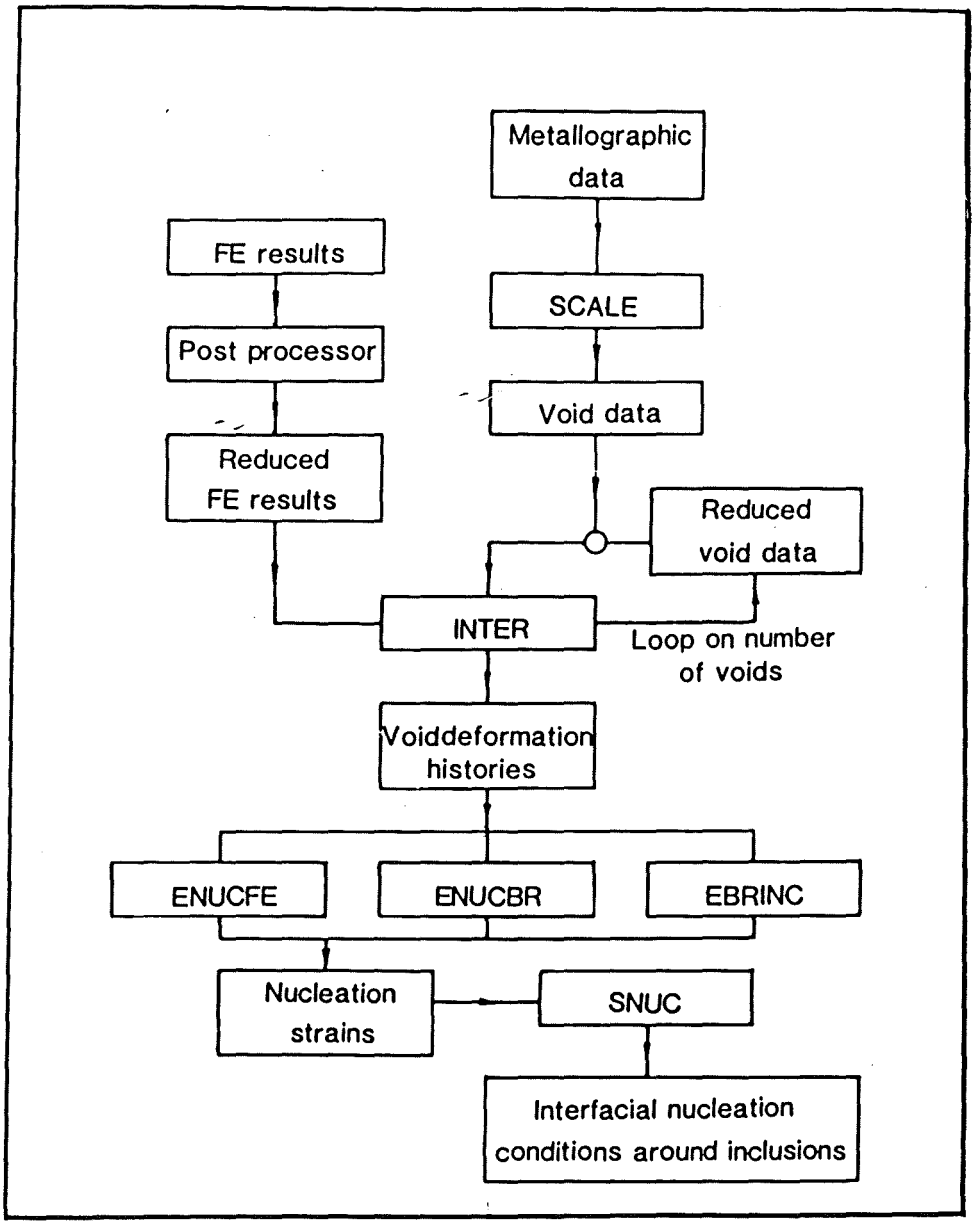

Fig.A.2.1. The interaction of files required for the analysis of void nucleation.

A.2.1. PRE-PROCESSING OF THE METALLOGRAPHIC DATA.

The program entitled SCALE (fig.A.2.1) reduces the dimensions of voids observed on the micrographs of the deformed specimen held on a metallographic data file to actual dimensions and computes the

transverse coordinate of each void for comparison with the coordinate of the centroids of elements lying on the transverse axis of the finite element mesh. Results are written to a void data file and the program also calculates the average diameter for the voids sample.

A.2.2. VOID DEFORMATION HISTORIES.

The INTER program in fig.A.2.1 accesses the deformation histories for each load step of elements on the transverse specimen axis, produced by the finite element post-processor and the void data file produced by SCALE. Only one void is analysed in each pass through INTER and, selecting the first void, its data is removed and the file re-written. Using a two dimensional linear interpolation, local conditions at the current void at the end of the test are computed and the position of the void with respect to adjacent element centroids is determined. Reducing the plastic strain in increments of 1% and assuming the position of any void remains fixed with repect to adjacent element centroids throughout the deformation of the specimen, the two dimensional linear interpolation is repeated to give a deformation history for the current void. Having completed the calculation for one void, the void data file is retrieved and a new void selected from the top of the list. A separate file stores the deformation history of each void together with other information essential to the next stage of the analysis.

INTER comprises a master routine which calls subroutines to perform the arithmetic. Switches may be set to allow the program to run interactively, which is useful during the analysis of a new specimen since data may be echoed and intermediate results output. For

production runs it is preferable to run in a batch mode with output routed to disk files for access by subsequent programs.

A.2.3. NUCLEATION STRAINS.

Having constructed a deformation history for each void, the void growth equations may be solved to determine the strain at which any observed elliptical void was circular, this being identified with the nucleation strain. This calculation was performed by the program ENUCFE. The solution algorithm initially assumes a value for the nucleation strain of the first entry in the void data file and re-writes the file with this entry removed. The initially circular void is then allowed to grow according to McClintock's (1969) equations. These are applied in increments of remote strain in a triaxial stress state determined from the finite element results until this strain has reached the value at which the experiment was stopped. The size of the resulting void is compared with the size observed on the metallographic section, the difference being expressed as a residual. On the basis of this residual, the assumed nucleation strain is adjusted and the program iterates until convergence is achieved.

During the void growth phase of the solution, the option is available to either allow the minor axis to grow unconstrained, as would be the case in a free void subject to a tensile transverse stress or to pin the minor diameter to some fixed value, usually identified with the initial inclusion diameter. This simulates lack of decohesion on the equator of the inclusion subject to tensile transverse stresses and the pinning effect of the inclusion in the presence of compressive transverse stresses. Voids in real materials probably

lie somewhere between these extremes, with the void being pinned initially until the transverse stress reaches some critical value at which complete decohesion occurs or the particle cracks. In practice, the calculations indicate little difference in the predicted nucleation strain under either extreme condition.

For comparison with the nucleation strain as determined with the finite element solutions, and for the analysis of plain tensile specimens for which an analytic solution is acceptable (Needleman (1972)), similar calculations were performed by the programs EBRINC and ENUCBR using Bridgman's (1952) assumption of constant strain across a diffuse neck in which the a/R ratio develops linearly with the remote strain. This allows the local triaxiality to be determined analytically. The former program performs the calculations incrementally while the latter allows the void to grow in a single step. Otherwise the solution algorithm is as before.

Having run through all three solution algorithms for each void, the results for the void sample from a single specimen are written to a nucleation strain file together, in the finite element based analysis, with the triaxiality at nucleation as read from the void deformation history. In the Bridgman (1952) based analyses, this is available analytically and is recalculated in subsequent programs rather than stored in the nucleation strain file.

A.2.4. INTERFACIAL STRESSES AT NUCLEATION.

The final stage in the nucleation analysis is the calculation of the secondary stress variables from the data held in the nucleation strain file, via the SNUC program. This performs similar operations for all three solution algorithms described in section A.2.3. By numerically solving the stress-strain power law:

$$(\bar{\sigma}/\sigma_0)^{(1/n)} - (\bar{\sigma}/\sigma_0) = (\bar{e}^p/e_0)$$

the effective stress corresponding to any nucleation strain is determined. The triaxiality given in the nucleation strain file for the finite element based solutions or by assuming a linear development of the a/R ratio of the notch in the Bridgman (1952) based analyses, then fixes the mean stress. The maximum interfacial radial stress on the surface of the inclusion is expressible as a function of the remote strain either through the expression of Argon, Im and Safoglu (1975) or by the piecewise analytic expression derived of the current work, the latter being preferred here. Here remote strain is identified with the local strain in a complete notch tensile specimen and is held for the chosen voids in the nucleation strain file. The maximum interfacial stress on the inclusion may thus be calculated.

A.3. THE NUMERICAL ANALYSIS OF FAILURE INITIATION.

Failure initiates in the interior of axisymmetric specimens specimen near to the mid-point of the transverse axis. The determination of void growth rates in this critical region and hence the local porosity at failure initiation thus requires a deformation history giving the development of triaxiality and local strain with remote strain for the central region of a specimen. Given the numerical tools devised in the nucleation analysis (fig.A.2.1), the most convenient method of assembling the required deformation history is to set up a dummy metallographic data file containing data for one isolated void of unit dimensions at the centre of the specimen, and to process this data through the first few stages of the nucleation analysis, as shown in fig.A.3.1.

In view of the small strain concentrations which exist prior to flow localisation, there will be virtually no interaction between discrete voids near the failure zone of the specimens and the growth of a population of voids will be a summation of the growth of each void considered in isolation. Furthermore, since continuum mechanics contains no size effect, the growth of the total void population may be found by multiplying the growth of the unit void by a scale factor based on ratio of the volume of the unit void to the actual initial porosity or volume fraction of inclusions. With the deformation history for the centre of the specimen, the void growth equations may be applied to the unit void up to the experimentally determined failure initiation strain and the results scaled to give the porosity at failure. These calculations were performed numerically by the STAT program in fig.A.3.1, in which void nucleation at finite deformations is

included through the use of the probabilistic nucleation criterion determined in the current work.

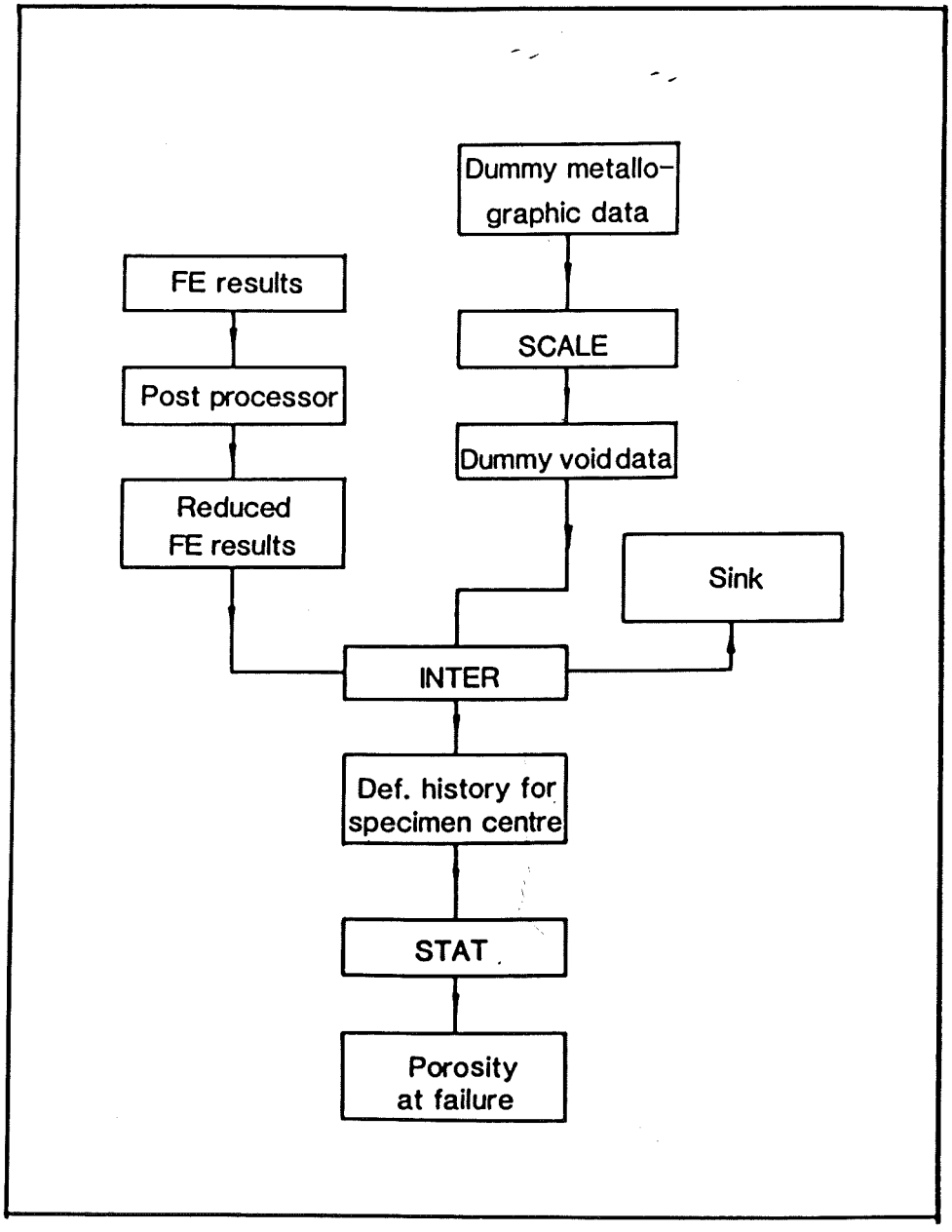

Fig.A.3.1. The files involved in the analysis of failure.

Given the initial statistical distribution of inclusions, the critical porosity in the region in which failure initiates will not be identical to that in the average material and STAT was looped on initial porosities up to a value of 10%, which has an 82% probability of occurrence somewhere in the critical zone. On this basis, the actual critical porosity was investigated.